

UNIVERSITY OF COPENHAGEN
NIELS BOHR INSTITUTE



Enhancing transparent superconductor-semiconductor hybrids

**Advances enabling future experiments
in proximitized InAs(Sb) systems**

Asbjørn Cennet Cliff Drachmann

UNIVERSITY OF COPENHAGEN
FACULTY OF SCIENCE
NIELS BOHR INSTITUTE



ENHANCING TRANSPARENT SUPERCONDUCTOR-SEMICONDUCTOR HYBRIDS

*Advances enabling future experiments in proximitized
InAs(Sb) systems*

ASBJØRN CENNET CLIFF DRACHMANN

Ph.D. Thesis
Center for Quantum Devices
Niels Bohr Institute
University of Copenhagen

Academic Advisor:

Prof. C. M. Marcus

Assessment Committee:

Prof. J. Nygård
Prof. L. Kouwenhoven
Prof. T. Schäpers

August 2020



Center for
Quantum
Devices

DANSK RESUME

Superleder-halvleder hybrider studeres hovedsageligt pga. den potentielle opdagelse af Majorana tilstande som kunne facilitere skalerbare kvantecomputere. Vigtige aspekter af kredsløbsbehandling inkluderer mønstring og fjernelse af superledende materialer, hvilket kan føre til urenheder/uregelmæssigheder i hybridene. Denne afhandling undersøger nye teknikker til superleder mønstring.

Vi demonstrerer udsigterne for brugen af anodisk oxidation på transparente superleder-halvleder hybrider, specific på lavtliggende 2-dimensionel elektrogas (2DEG) heterostrukturer afsluttet med epitaksialt dyrket Al. Delvis oxidation af Al øger dets superledende kritiske temperatur samt dets kritiske magnetfelt. Sammenlignet med brugen af sædvanlig Al æts, så passiverer en komplet oxidering af Al den underliggende 2DEG, og øger dets ledningsbæres egenskaber. Kvant Hall effekt opnås en Tesla under det højeste opnåede kritiske magnetfelt af oxideret aluminium. Brugen af en metalskabelon til litografi af anodisk oxidering muliggøre en tværgående opløsning < 50 nm. Masken bruges til at konstruere

et magnetfelt-robust Josephson knudepunkt. Det nye materialesystem, bestående af en forstyrret superleder i transparent kobling til en underliggende 2DEG, viser $1/B$ periodiske svingninger i magnetomodstand, både under og over det superledende kristiske magnetfelt. Især oscillationerne under the kristiske magnetfelt studeres som funktion af magnetfelt, temperatur og DC strøm. Til sidst uddybes forslag til forbedring af processen til anodisk oxidation samt forslag til yderligere materiale opgraderinger.

ABSTRACT

Superconductor-semiconductor hybrids are studied, mainly due to the potential discovery of Majorana zero modes that could facilitate scalable quantum computers. Improving material quality and fabrication processes is believed necessary in order to realize Majorana zero mode applications. Important aspects of device processing include patterning and removal of superconducting material, which can lead to disorder/irregularities of the hybrid. This thesis investigates new techniques for superconductor patterning.

We demonstrate the prospects of using anodic oxidation on transparent superconductor-semiconductor hybrids, specifically on shallow InAs 2-dimensional electron gas (2DEG) heterostructures terminated with epitaxially grown Al. Partial oxidation of Al increases its superconducting critical temperature and critical magnetic fields. Compared to using a regular Al etch, a full Al oxidation passivates the underlying 2DEG, enhancing the carrier properties. The quantum Hall effect is achieved one tesla below the highest achieved critical field of oxidized Al. Using a metal mask for lithography enables a lateral resolution < 50 nm with

anodic oxidation. The mask is used to construct a magnetic field resilient Josephson junction. The novel system of a disordered superconductor with transparent coupling to an underlying 2DEG, shows $1/B$ periodic magnetoresistivity oscillations both below and above the superconducting critical field. In particular, the oscillations below the critical field is studied as a function of magnetic field, temperature, and DC current. Lastly, suggestions for improvements of the anodic oxidation setup and for further material upgrades are elaborated.

ACKNOWLEDGMENTS

First and foremost, I would like to express deep gratitude to **Charles M. Marcus** for his contributions in establishing QDev; a great frontier research facility in little Denmark that attracts bright minds from all corners of the world. It's been a privilege to have access to all your resources, both financially, intellectually and your huge community.

I'm very grateful to **Jesper Nygård**, **Leo Kouwenhoven** and **Thomas Schäpers** for taking out time to assess this thesis!

The knowledge and experience that condensed into this thesis was obtained over several years guided by many different mentors.

Shout-out to Charlie and **Ferdinand Kuemmeth** who included me in QDev back in 2013 and to **Thomas Sand Jespersen** for taking me under his wing for a year, introducing me to superconductor/semiconductor hybrids. Since the start, **Shivendra Upadhyay** has been an unofficial supervisor in all things fab-related. Whether it was a quick question in the hallway or a late evening call, Shiv was always available. Your helpful spirit and diligent approach to fab has been, and still is, contagious.

I'm grateful to **Chris Palmstrøm** for hosting me in Santa Barbara back in the summer of 2015 and especially to **Borzoyeh Shojaei** who taught me everything I know about Sb-based InAs 2DEG heterostructures.

Coming back to QDev I joined Charlies topo-2DEG team which consisted of **Fabrizio Nichele**, **Henri Suominen**, and **Morten Kjærgaard**. A big thanks for teaching me a lot about working with shallow InAs 2DEGs and how to run measurements at a dilution refrigerator. I had many enlightening interactions with **Alexander R. Hamilton** during his sabbatical in Copenhagen and after. Your vast knowledge on materials and transport has been highly appreciated. I'm looking forward to having more interesting conversations in the future.

I am very grateful to the present and past 2DEG team creating an enjoyable atmosphere in and outside the lab. **Alexander Whiticar**, it's been a pleasure knowing you for 6 years! Your ability to focus and put in the hours is both inspiring and intimidating. Alex, **Antonio Fornieri & Eoin O'Farrel**, it was a pleasure working with you bringing the shallow InAs 2DEG hybrids to their present glory. **Abhishek Banerjee**, I value the many interesting and informative physics discussions as well as your penetrating energy and laughter. **Ahnaf, Alisa, Anders, Andreas, Daniel, DS, Felix** and **Sangeeth**, it's been a pleasure having you joining the topo2DEG group as well. It's great to see the 2DEG hybrids being used for many different research experiments!

Our work would not have been possible without the valuable materials we get from **Michael J. Manfras** team at Purdue University. Mike, **Geoff Gardner, Candice Thomas, Sergei Gronin** and **Rosa Diaz**, I'm very grateful for the materials and the great collaboration we had over the years! And thanks for being generous hosts for my Purdue visit. Here also Mikes measurement team, **Tailung, Teng** and **Saeed** were great hosts! Thanks for the

help enabling me to get useful measurement results within the couple weeks that were available.

I was fortunate to also visit **David Goldhabor-Gordons** lab at Stanford. A special thanks to **Connie** for being my main host. It's always a pleasure being around you! To the rest of the DGG-team: It was a pleasure getting to know all of you guys! I immediately felt as being part of the DGG-family. David, **Aaron** and **Joe**, thanks for introducing me to the exciting world of Twistronics.

Christoph Strunk, thank you for inviting me to give a talk in Regensburg and thanks to **Nicola**, **Christian** and **Lorenz** for showing me around. It's great to see other groups applying the shallow InAs 2DEG platform.

I'm grateful to **Ioan Pop**, for inviting me to join their summer excursion/seminar to the Italian Alps. Getting a sneak peek into the world of granular aluminum greatly improved my understanding of our disordered AI data.

A collective thanks goes out to **Ady Stern**, **Bernard van Heck**, **Brian M. Andersen**, **Karsten Flensberg**, **Mikhail Feigel'man**, **Roman Lutchyn** and **Yuval Oreg** for many educational conversations, helping me getting my head around our data and other related physics.

A humongous thanks to the Admin team: **Dorthe**, **Katrin**, **Maria**, **Marianne** and **Tina**. The great effort you put into making our lives easier and better is highly appreciated! A lot of frustrating bureaucracy has been avoided due to you.

Regarding things running smoothly; **Claus Sørensen** and the cleanroom team, your efforts in keeping the lab and tools running is highly appreciated.

I want to thank **Mark Rudner** as well for a splendid collaboration on making a new version of our local CMP1 course. The two quarters of TA'ing with you were very rewarding, both academically and in terms of teaching.

A heartfelt thanks goes to all the people who helped fulfilling my non-academic needs over the years. The QDev team has been like a second family. I would like to thank **Alisa** for the swings; **Anders** for the many memorable moments during the past decade; **Esben** for the occasional Lunch#2; **Filip K** for your unique humor and for sharing your big day with the rest of us; **Judith** for always creating a pleasant atmosphere, eg. with shoulder scratches and (premature) X-mas decor; **Natalie** for the yearly Halloween parties and the many delicious cakes; **Rob** for your endless kindness and giving spirit; **Sole** for many great and intensive discussions. A most warmly thanks to these past and present QDev fam' member for many enjoyable moments: **Aga, Albert, Andrew, Anasua, Aske, Christian O, Christian V, Dags, Damon, Denise, DR, DS, Esteban, Fabio, Federico, Filip M, Gerbold, Giulio, Jess, Joachim, Johannes, José, Juan Carlos, Karolis, Karthik, Lucas, Lukas, Katrine, Maren, Marina, Martin B, Martin E, Michaela, Mingtang, Mohana, Monica, Paschalis, Rasmus, Rikke, Ruben, Sachin, Thomas K, Thorvald** and **Vivek**.

Within my time at the the Niels Bohr Institute, I have accumulated many precious friends outside of QDev as well; too many to name everyone here! A special thanks to team Obvious, team Hammer, team MaXiT, team Slyngel, FysikRevy™ and to these lovely individuals: **Abdu, Annika, Bakke, Bidse, Buster, Darling, Freja, Gorm, Helle KL, Helle G, Julie, Kildholt, Kris, Kruse, Magnus, Marieke, Momsen, Nanse, Ness, Nina, Peter, Rosie, Sofie, Sofus, Vektor & Øsse**.

Words can't even express how grateful I am to my family and friends outside of physics who despite my absence have continued to throw love in my direction! **Mor, Far, Anine, Zidsel, Thomas, Maria**, jeres dejlig vedhæng og hele den jyske familie – af hjertet tak! To the dudes and dudettes from Brøndby. Your endless love and open arms are forever appreciated.

Last, but not least, a huge thanks to these kind souls for proof-reading this dissertation: Abhishek, Alisa, Ahnaf, Anders, Andreas, Bakke, Felix, Gorm, Judith and Kruse.

LIST OF PUBLICATIONS

Results from these publications are used in this dissertation

1. **Asbjørn C. C. Drachmann**, Abhishek Banerjee, Antonio Fornieri, Alexander M. Whiticar, Candice Thomas, Sergei Gronin, Tiantian Wang, Geoffrey C. Gardner, Michael J. Manfra, and Charles M. Marcus.

Magneto-resistivity oscillations in disordered superconductor on InAs 2DEG heterostructure

Manuscript in preparation

2. **Asbjørn C. C. Drachmann**, Rosa E. Diaz, Candice Thomas, Henri J. Suominen, Alexander M. Whiticar, Antonio Fornieri, Sergei Gronin, Tiantian Wang, Geoffrey C. Gardner, Alex R. Hamilton, Fabrizio Nichele, Michael J. Manfra, and Charles M. Marcus.

Anodic Oxidation of Epitaxial Superconductor-Semiconductor Hybrids

arXiv: 2009.08190.

Publications not directly part of this dissertation

1. A. M. Whiticar, A. Fornieri, E. C. T. O'Farrel, **A. C. C. Drachmann**, T. Wang, C. Thomas, S. Gronin, R. Kallaher, G. C. Gardner, M. J. Manfra, C. M. Marcus, F. Nichele.
Coherent transport through a Majorana island in an Aharo-nov-Bohm interferometer
Nat. commun. **11**, 3212 (2020)
2. F. Nichele, E. Portolés, A. Fornieri, A. Whiticar, **A. C. C. Drachmann**, S. Gronin, T. Wang, G. C. Gardner, C. Thomas, A. T. Hatke, M. J. Manfra, C. M. Marcus.
Relating Andreev Bound States and Supercurrents in Hybrid Josephson Junctions.
Phys. Rev. Lett. **124**, 226801 (2020)
3. A. Fornieri, A. M. Whiticar, F. Setiawan, E. Portolés, **A. C. C. Drachmann**, A. Keselman, S. Gronin, C. Thomas, T. Wang, R. Kallaher, G. C. Gardner, E. Berg, M. J. Manfra, A. Stern, C. M. Marcus, F. Nichele.
Evidence of topological superconductivity in planar Josephson junctions.
Nature, **569**, 89-92 (2019)
4. E. C. T. O'Farrel, **A. C. C. Drachmann**, M. Hell, A. Fornieri, A. M. Whiticar, E. B. Hansen, S. Gronin, G. C. Gardner, C. Thomas, M. J. Manfra, K. Flensberg, C. M. Marcus, F. Nichele.
Hybridization of Subgap States in One-Dimensional Super-conductor-Semiconductor Coulomb Islands.
Phys. Rev. Lett., **121**, 256803 (2018)
5. F. Nichele, **A. C. C. Drachmann**, A. M. Whiticar, E. C. T. O'Farrel, H. J. Suominen, A. Fornieri, T. Wang, G. C. Gardner, C. Thomas, A. T. Hatke, P. Krogstrup, M. J. Manfra, K. Flensberg, C. M. Marcus.
Scaling of Majorana zero-bias conductance peaks.
Phys. Rev. Lett., **119**, 136803 (2017)

-
6. **A. C. C. Drachmann**, H. J. Suominen, M. Kjærgaard, B. Shojaei, C. J. Plamstrøm, C. M. Marcus, F. Nichele.
Proximity effect transfer from NbTi into a semiconductor heterostructure via epitaxial aluminum.
Nano Lett., **17**, 1200 (2017)
 7. B. Shojaei, **A. C. C. Drachmann**, M. Pendharkar, D. J. Pennachio, M. P. Echlin, P. G. Callahan, S. Kraemer, T. M. Pollock, C. M. Marcus, C. J. Palmstrøm.
Limits to mobility in InAs quantum wells with nearly lattice-matched barriers.
Phys Rev B., **24**, 245306 (2016)

CONTENTS

Dansk Resume	iv
Abstract	vi
Acknowledgments	vii
List of Publications	xiii
Table of Contents	xvii
List of Figures	xxi
List of Tables	xxv
1 WHY WORK ON SUPERCONDUCTOR-SEMICONDUCTOR HYBRIDS?	1
1.1 Topological quantum computers	1
1.2 Material quality	3
1.3 Dissertation structure	3
2 ESSENTIAL CONCEPTS	5
2.1 Semiconductor: Two-dimensional electron gas	6
2.1.1 Models for electron transport in materials.	6
2.1.2 Semiconductor transport	10
2.1.3 2-Dimensional Electron Gas	12
2.1.4 Spin-Orbit coupling	14
2.2 Magnetic field induced phenomena in 2DEGs	15
2.2.1 Zeeman	15
2.2.2 Weak Localization	16
2.2.3 Shubnikov-de Haas oscillations	17
2.2.4 Integer Quantum Hall Effect	19
2.3 Superconductivity	21
2.3.1 Discovery of superconductivity	21
2.3.2 Bardeen-Cooper-Schrieffer theory	22
2.3.3 Ginzburg-Landau theory	24
2.3.4 Coherence length and penetration depth	24

	2.3.5	Type I and type II superconductors	25
	2.3.6	Vortex physics	27
	2.3.7	Thin film/disordered superconductors	28
2.4		Hybrid interfaces	31
	2.4.1	Andreev reflection	31
	2.4.2	BTK	31
	2.4.3	Proximity effect	37
	2.4.4	Josephson junctions	40
	2.4.5	Majorana modes	41
	2.4.6	Superconducting quantum Hall edge	45
3		MATERIAL, FABRICATION AND EXPERIMENTAL SETUP	49
	3.1	Material stack considerations	49
	3.1.1	Choosing a material platform	49
	3.1.2	Shallow InAs-based 2DEGs	51
	3.1.3	Choosing a growth substrate	54
	3.1.4	Characterizing the material of choice	55
	3.2	Fabrication with Al Etch	61
	3.3	Introducing anodic oxidation	66
	3.3.1	Motivation	66
	3.3.2	Chemical reaction and experimental setup	67
	3.3.3	Adjustments to AO setup	69
	3.4	Measurement Setup	73
4		ANODIC OXIDATION OF Al ON INSULATING GaAs	75
	4.1	Material and Devices	75
	4.2	Morphology of anodized Al	76
	4.3	Transport study	79
	4.4	Conclusion	83
5		ANODIC OXIDATION OF Al ON InAs 2DEGS	85
	5.1	Devices	85
	5.2	Enhanced critical fields of thinned Al on InAs 2DEG	87
	5.3	Surface passivation	90
	5.3.1	Increased carrier mobility	91
	5.3.2	Integer quantum Hall effect in shallow InAs 2DEG	93
	5.4	Conclusion	97
6		ENABLING HIGH RESOLUTION LITHOGRAPHY WITH ANODIC OXIDATION	99
	6.1	Metal masking	99
	6.2	Devices for evaluating the fab	101
	6.3	Field-induced supercurrent oscillations	104
	6.4	Conclusion	109
7		$\rho(B_{\perp})$ OSCILLATIONS IN SUPERCONDUCTOR/2DEG HYBRID	111
	7.1	Observation of magnetoresistivity oscillation	112
	7.2	Temperature and $1/B_{\perp}$ dependence	118

7.3	DC Current dependence	121
7.4	Conclusion and work to be done	124
8	IDEAS FOR FUTURE PROJECTS	127
8.1	III/V growth improvements with Sb	128
8.2	AO time-dependence	128
8.3	Upgrading AO lithography	129
8.3.1	Removing Ti mask selectively with dry etch	130
8.3.2	Shallow etch mask	131
8.4	Other techniques applying oxidation of Al	131
8.4.1	Local anodic oxidation using AFM	132
8.4.2	Growing Pb on top of Al	132
	Appendices	139
A	SUPERCONDUCTING PROPERTIES OF BULK ELEMENTS	139
B	FABRICATION RECIPES	141
B.1	Mixing ammonium tartrate for AO	142
B.2	Initial clean	143
B.3	Evaporating Ti/Au alignment marks	143
B.4	Mesa etch	144
B.5	Aluminum etch	145
B.6	Ti mask for anodic oxidation	147
B.7	E-Beam resist mask for anodic oxidation	147
B.8	Anodic oxidation	148
B.9	Etch of anodized Al	149
B.10	Hafnia deposition with ALD	149
B.11	Inner gates deposition	150
B.12	Outer gates deposition	151
C	ADDITIONAL DATA	153
C.1	$R(B, T)$ of Al on GaAs	154
C.2	$R(B, T)$ of Al on InAs	155
C.3	Carrier properties of Hall bar anodized at 4.8 V, β	157
C.4	Quantum Hall effect of Hall bar with $V_{AO} = 4.8$ V, β	158
C.5	Other AO-defined Josephson Junctions	161
C.6	Magnetoresistivity study of 4.2 V, α	163
D	LANDAU-BÜTTIKER ANALYSIS WITH $R_{xx} = R_{xy}$	169
	Bibliography	172

LIST OF FIGURES

Figure 2.1	Hall bar measurement	8
Figure 2.2	Carrier mobility versus material quality	11
Figure 2.3	Weak localization	16
Figure 2.4	Landau levels	18
Figure 2.5	Integer quantum Hall effect	20
Figure 2.6	BCS density of states	23
Figure 2.7	Magnetic field on superconductors	26
Figure 2.8	Vortex flow	27
Figure 2.9	Superconductor-Insulator Transition	30
Figure 2.10	Andreev reflection	32
Figure 2.11	BTK Theory	33
Figure 2.12	Superconducting proximity effect	37
Figure 2.13	Controlling the induced gap	39
Figure 2.14	Illustration of Majorana wire	42
Figure 2.15	Edge state Andreev reflection	46
Figure 3.1	Proximity coupling from sidewall	52
Figure 3.2	Shallow InAs quantum well	53
Figure 3.3	Material of choice: M26	55
Figure 3.4	M26 etch-defined Hall bar	57
Figure 3.5	M26 AG Al bar	58
Figure 3.6	M26 spectroscopy	59
Figure 3.7	M26 wire	60
Figure 3.8	Fabrication steps	63
Figure 3.9	Reflowing resist before wet etch	65
Figure 3.10	Different aluminum processes	66
Figure 3.11	Chemical reaction of anodic oxidation	68
Figure 3.12	Bond placement for anodic oxidation	70

Figure 3.13	Chip orientation for bonding	72
Figure 4.1	Al on GaAs material and devices	76
Figure 4.2	TEM study of anodized Al	77
Figure 4.3	Transport data from GaAs material	80
Figure 4.4	T -dependence of critical fields	81
Figure 5.1	Al on InAs 2DEG devices	86
Figure 5.2	Enhancing Al on InAs 2DEG	88
Figure 5.3	Increased carrier mobility with AO	91
Figure 5.4	SdHO and Hall quantization	93
Figure 5.5	QHE resistivity maps	95
Figure 5.6	High B_{\perp} ρ_{xx} -measurements of etched Hall bar	96
Figure 6.1	SEM of AO with PMMA	100
Figure 6.2	Metal mask process flow	101
Figure 6.3	Superconducting bar after double AO	102
Figure 6.4	Semiconducting bar after double AO	103
Figure 6.5	AO defined Josephson junction	105
Figure 6.6	Josephson junction in high B_{\perp}	106
Figure 6.7	Supercurrent oscillations	108
Figure 6.8	I_{sw} and R_{bg} oscillations	110
Figure 7.1	Optical micrograph of the studied device	112
Figure 7.2	Magneto-resistivity isotherms, linear axis	113
Figure 7.3	Magneto-resistivity isotherms, log axis	116
Figure 7.4	Comparing $R_{xx}(B_{\perp})$ and $R_{xy}(B_{\perp})$	117
Figure 7.5	Inverse temperature dependence	119
Figure 7.6	$1/B_{\perp}$ dependence of ρ_{xx} oscillations	120
Figure 7.7	I_{DC} dependence of $\tilde{\rho}_{xx}$ and $\tilde{\rho}_{xy}$	122
Figure 7.8	Line cuts of I_{DC} dependence of $\tilde{\rho}_{xx}$ and $\tilde{\rho}_{xy}$	123
Figure 7.9	Line cuts of small I_{DC} dependence of $\tilde{\rho}_{xx}$ and $\tilde{\rho}_{xy}$	124
Figure 8.1	Implementing Ti mask removal	130
Figure 8.2	Shallow etch masking AO	131
Figure 8.3	Process proposal for Pb hybrid	133
Figure A.1	Superconducting T_c of elements	140
Figure C.1	$R(B_{\parallel})$ -scans from Al on GaAs	154
Figure C.2	$R(B_{\perp})$ -scans from Al on GaAs	155
Figure C.3	$R(B_{\perp})$ -scans from Al on InAs	155
Figure C.4	$R(B_{\parallel})$ -scans from Al on InAs	156
Figure C.5	Hall measurements for 4.8 V Hall bar on device β	157
Figure C.6	SdHO and Hall quantization from Hall bar with $V_{AO} = 4.8$ V on device β	158
Figure C.7	Hall measurements for Hall bar with $V_{AO} = 4.8$ V on device β	159
Figure C.8	Other AO-defined Josephson Junctions	162

Figure C.9	Magneto-resistivity isotherms from bar α , linear axis	163
Figure C.10	Magneto-resistivity isotherms from bar α , log axis	164
Figure C.11	Comparing $R_{xx}(B_{\perp})$ and $R_{xy}(B_{\perp})$, bar α	165
Figure C.12	I_{DC} and B_{\perp} dependence of ρ_{xx} and ρ_{xy}	166
Figure D.1	Voltage probes on Hall bar	169
Figure D.2	Setups used for Landauer-Büttiker analysis	170

LIST OF TABLES

Table 1	BTK amplitudes	35
Table 2	InAs properties	51
Table 3	Carrier properties for various Hall bars	92
Table 4	Landau-Bütikker calculations	171

WHY WORK ON SUPERCONDUCTOR-SEMICONDUCTOR HYBRIDS?

If not familiar with two-dimensional electron gasses, quantum Hall effect, superconductivity, and/or the proximity effect the reader is suggested to start reading [chapter 2](#), where the essentials of these topics are briefly covered.

1.1 TOPOLOGICAL QUANTUM COMPUTERS

Quantum computers¹. Back in 1982, Richard Feynman postulated that to simulate quantum systems we would need to build quantum computers [1]. It requires a huge amount of data and time for a classical computer to simulate the probabilistic nature of quantum systems. Instead, we could try to build a quantum system that directly simulates the problem we want to solve. Even better, universal quantum computers would enable us to solve different kinds of problems. It was later realized that with certain algorithms, quantum computers could also solve classical problems that are unsolvable² for classical computers, eg. the famous Shor's algorithm [2].

1 ... is one of the answers to the title; for sure the financially most prominent.

2 Unsolvable means that it would take unfeasible amount of time.

The promise of unfathomable computing power has captivated the attention of many big tech companies as well as governments in America, Asia and Europe. Thus, quantum computers and related technologies have become some of the most funded scientific ventures of all time.

The quantum supremacy milestone³ was reached in 2019 where the Google team, led by J. Martinis, used a collection of superconducting quantum bits to do a specifically designed simulation in a matter of minutes [3]. They stated: "our benchmarks currently indicate that the equivalent task for a state-of-the-art classical supercomputer would take approximately 10,000 years".

Though promising, we are still far from the end goal of a universal scalable, fault tolerant quantum computer. The scaling of most quantum bits, including the superconducting ones, are limited by cross talk and their decoherence times being too short. The amount of operations (calculations) we can do is limited by the loss of quantum information over time.

Another proposed quantum bit (yet to be realized) is based on the topological nature of Majorana modes, protecting them from local perturbations, which potentially prolong coherence times [4]. Belonging to a novel class of particles, Majorana modes would also be a highly interesting topic for general academic research, and the first researchers to verify its existence should expect an invitation to Stockholm. Some of the most promising proposals for realizing Majorana modes are based on low-dimensional superconductor-semiconductor hybrids [5–8].

Other academic research progresses rely on high quality super-conductor-semiconductor hybrids. Eg. the combination of quantum Hall effect and superconductivity have many intriguing prospects, including exotic circuit elements [9].

³ Quantum supremacy: Demonstration of a quantum computer calculating a classically unsolvable problem.

1.2 MATERIAL QUALITY

Over the past decade, significant improvements of superconductor-semiconductor hybrids have been established, especially with the epitaxial match by *in-situ* growth of the hybrid stack, demonstrated on vapour-liquid-solid nanowires [10], two-dimensional electron gases [11] and selective area growth [12]. A high quality growth lays a good foundation for potential new discoveries, but the following fabrication (construction) of devices is an equally important factor. With the ever increasing demands on material quality for new experiments, optimization of growth and fabrication is necessary.

The topic, that ended up becoming the main portion of this PhD dissertation is the use of anodic oxidation in fabrication of epitaxial hybrids to enhance their properties.

It started as a small quest of trying to realize a cute idea. The idea, put out by David Tuckerman and Burton Smith from Microsoft, was mentioned in W. Changs thesis from 2014 [13]: "...we can selectively turn parts of the Al shell into Al_2O_3 via electrolytic anodization... This method should protect the InAs core and retain its innate mean free path...".

Besides verifying increase of the semiconductor mean free path, the application of anodic oxidation also led to an unexpected study of disordered SC, which at first, to us, was unknown territory with peculiar superconducting properties.

1.3 DISSERTATION STRUCTURE

Most of the essentials needed to understand the topics of this dissertation are mentioned in [chapter 2](#). Our material of choice is a shallow InAs 2DEG capped with epitaxially grown Al. This material and its current state of the art fabrication are elaborated in [chapter 3](#), which also introduces the procedure for implementing anodic oxidation. The chapter also shows how to measure and characterize a wafer.

[Chapter 4](#) presents results from anodic oxidation of epitaxial Al grown on insulating GaAs. A partial oxidation shows increases in critical temper-

ature and in particular critical fields; both parallel and perpendicular to the Al plane. A transmission-electron-microscopy study of the anodized film identifies a bumpy morphology. The results indicate Al becoming disordered by the oxidation.

Similar improved superconducting properties are found for partially oxidized Al on a shallow InAs 2DEG heterostructure, presented in [chapter 5](#). Data from fully oxidized Al shows an improvement of carrier mobility in the underlying 2DEG compared to when implementing a regular Al etch. Hall bars with the highest mobilities are studied at high perpendicular magnetic fields, showing integer quantum Hall effect.

Our progress in enabling lithography with anodic oxidation with nanoscopic lateral resolution is elaborated in [chapter 6](#). Verification of the resolution is done by realization of a thin, elongated Josephson junction. It shows oscillations of the critical current as a function of both the perpendicular and in-plane magnetic field, transverse to the transport direction.

Having a disordered superconductor in transparent connection to a 2DEG composes a novel material system. [Chapter 7](#) studies magnetoresistivity oscillations in this system, in particular the small oscillations that emerge at magnetic fields $B < B_c$ are studied as a function of magnetic field, temperature and DC current bias.

The final [chapter 8](#) discusses different further improvements to our hybrid material system. These include incorporating Sb in the heterostructure, improving the anodic oxidation process setup and enabling universal fabrication with anodic oxidation benefits. Finally other strategies for incorporating Al oxidation in our process flow is elaborated.

2

ESSENTIAL CONCEPTS

Semiconductors, superconductors, and hybrids of the two, are heavily studied systems, both theoretically and experimentally. This is testified by the immense literature on those subjects. This chapter will highlight the essential knowledge within that literature, needed to understand the methods and results of the work presented in this thesis. The reader is assumed to have a prior undergrad level of knowledge about solid state physics.

Semiconductors, in particular two-dimensional electron gasses are elaborated in [section 2.1](#) while [section 2.2](#) elaborates emerging phenomena induced by applying external magnetic fields. [Section 2.3](#) presents key properties of superconductors while [section 2.4](#) displays the theory of superconductor interfaces, in particular with semiconductors.

2.1 SEMICONDUCTOR: TWO-DIMENSIONAL ELECTRON GAS

The discovery of semiconductors and their applications, especially the transistor¹, has shaped our computer-based modern society. This section will introduce key-features of semiconductors, working towards our understanding of 2DEGs and the integer quantum Hall effect.

2.1.1 *Models for electron transport in materials.*

Before we talk about semiconductors, we will start with a quick brush-up on the more general topic of electron motion in materials. More thorough elaborations can be found in solid state text books such as refs [14–17].

Naively, one would think that electrons scatter on all neighboring atoms, which are spaced by a few Å. Blochs theorem tells a different story: When in a perfectly periodic potential, like that from an atomic lattice, the electron wavefunctions will adjust and form plane waves:

$$\begin{pmatrix} u_{\mathbf{k}}(\mathbf{r}) \\ v_{\mathbf{k}}(\mathbf{r}) \end{pmatrix} = e^{i\mathbf{k}\mathbf{r}} \begin{pmatrix} u_0 \\ v_0 \end{pmatrix}, \quad (2.1)$$

where u_0 and v_0 are the amplitudes for electron and hole excitations; holes being vacant electrons. Variables in bold font are vectors; \mathbf{r} represents real-space and \mathbf{k} the reciprocal space. These freely moving effective particles, called *quasi particles*, have a new dispersion relation found by solving the Schrödinger equation:

$$\begin{pmatrix} H(\mathbf{r}) & 0 \\ 0 & -H(\mathbf{r}) \end{pmatrix} \begin{pmatrix} u_{\mathbf{k}}(\mathbf{r}) \\ v_{\mathbf{k}}(\mathbf{r}) \end{pmatrix} = E \begin{pmatrix} u_{\mathbf{k}}(\mathbf{r}) \\ v_{\mathbf{k}}(\mathbf{r}) \end{pmatrix}. \quad (2.2)$$

The Hamiltonian is

$$H(\mathbf{r}) = -\frac{\hbar^2}{2m^*} \nabla_{\mathbf{r}}^2 - \mu, \quad (2.3)$$

¹ Pioneering work was awarded the Nobel prize in physics 1956:
<https://www.nobelprize.org/prizes/physics/1956/summary/0>

resulting in the dispersion relation:

$$E(k) = \frac{\hbar^2 k^2}{2m^*} - \mu, \quad (2.4)$$

where \hbar is Planck's constant, μ is the chemical potential equal to the Fermi energy at zero temperature, and m^* the effective mass of the quasi particles. It is given by the local curvature at the dispersion minimum:

$$m^* = \hbar^2 \left(\frac{d^2 E}{dk^2} \right)^{-1}. \quad (2.5)$$

The Fermi energy

$$E_F(k_F) = \frac{\hbar^2 k_F^2}{2m^*}, \quad (2.6)$$

with the Fermi wave number, k_F , enables extraction of the Fermi velocity

$$v_F = \frac{\hbar k_F}{m^*}, \quad (2.7)$$

the speed with which chemically available electrons move.

Bloch's theory describes real materials well - to an extent. No physical material is defect-free and any irregularity to the lattice would cause the plane wave to collapse and re-disperse, causing the quasi particle to scatter. This is where Drude's theory on diffusive electron transport becomes very helpful. The theory assumes that electrons have a probabilistic scattering time τ_e . When they scatter, their average velocity goes to zero. In between scattering events they are accelerated by the Lorentz force of external electric E and magnetic B fields

$$F = -e(\mathbf{E} + \mathbf{v} \times \mathbf{B}), \quad (2.8)$$

e being the electronic charge, and \mathbf{v} the velocity. With Drude's model, important material parameters can be extracted from simple electrical measurements on Hall bars, see [figure 2.1\(a\)](#). The longitudinal and Hall resistivities

$$\rho_{xx} = \frac{V_{xx} W}{I L} \quad \rho_{xy} = \frac{V_{xy}}{I} \quad (2.9)$$

shall be used in the following derivation, inspired by ref. [17].

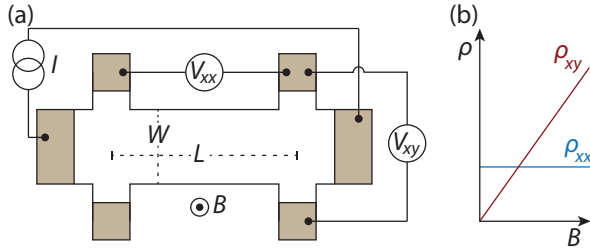


Figure 2.1: **Hall bar measurement:** (a) Sketch of Hall bar and corresponding measurement setup. A current I is sourced and V_{xx} and V_{xy} are measured as a function of applied field B . Width, W and length L of the active region of the bar is defined. (b) Expected B -dependence of longitudinal and Hall resistivity.

Consider an electron, at time t , has an average momentum $\langle \mathbf{p}(t) \rangle$ and ask: What is the average momentum at a later time $(t + dt)$? From the conditions given above, the particle could either have scattered $\langle \mathbf{p}(t + dt) \rangle = \mathbf{0}$ with probability dt/τ_e ; or continued its path, accelerated by equation 2.8, $\langle \mathbf{p}(t + dt) \rangle = \langle \mathbf{p}(t) \rangle + \mathbf{F}dt$, with probability $(1 - dt/\tau_e)$. The full equation becomes:

$$\langle \mathbf{p}(t + dt) \rangle = \mathbf{0} \cdot dt/\tau_e + (\langle \mathbf{p}(t) \rangle + \mathbf{F}dt) \cdot (1 - dt/\tau_e),$$

and is reduced by only considering linear order in dt :

$$\frac{d \langle \mathbf{p}(t + dt) \rangle}{dt} - \frac{d \langle \mathbf{p}(t) \rangle}{dt} = \mathbf{F} - \frac{\langle \mathbf{p}(t) \rangle}{\tau_e}$$

Applying an electric field only, in steady state, we find:

$$\frac{d \langle \mathbf{p} \rangle}{dt} = 0 = -e\mathbf{E} - \frac{\langle \mathbf{p} \rangle}{\tau_e} \rightarrow \langle \mathbf{p} \rangle = m^* \langle \mathbf{v} \rangle = -e\tau_e \mathbf{E}. \quad (2.10)$$

With the relation: $\mathbf{v} = \mu \mathbf{E}$, we can extract an expression for the *carrier mobility*

$$\mu = e\tau_e/m^*. \quad (2.11)$$

Writing [equation 2.10](#) into Ohms law, we can extract a lot of information from a conductivity, σ , measurement.

$$\sigma \mathbf{E} = \langle \mathbf{j} \rangle = -en_e \langle \mathbf{v} \rangle = \frac{e^2 \tau_e n_e}{m^*} \mathbf{E}, \quad (2.12)$$

with the current density \mathbf{j} and the *carrier density* n_e .

Now, applying an electric and a magnetic field, in the steady state, we find:

$$\begin{aligned} 0 &= -e(\mathbf{E} + \langle \mathbf{v} \rangle \times \mathbf{B}) - \frac{\langle \mathbf{p} \rangle}{\tau_e} \\ \rightarrow \mathbf{E} &= \left(\frac{\langle \mathbf{j} \rangle \times \mathbf{B}}{ne} + \frac{m^*}{e^2 n_e \tau_e} \langle \mathbf{j} \rangle \right) = \underline{\underline{\rho}} \langle \mathbf{j} \rangle, \end{aligned} \quad (2.13)$$

with $\underline{\underline{\rho}}$ being the 3×3 resistivity tensor. The longitudinal component is

$$\rho_{xx} = \rho_{yy} = \rho_{zz} = \frac{m^*}{e^2 n_e \tau_e} = \frac{1}{en_e \mu}, \quad (2.14)$$

with the last equality obtained by plugging in [equation 2.11](#). If $B \parallel \hat{z}$, the Hall resistivity will be

$$\rho_{xy} = \frac{B}{n_e e} \rightarrow n_e = \left(e \frac{d\rho_{xy}}{dB} \Big|_{B=0} \right)^{-1}. \quad (2.15)$$

Knowing n_e , we can now extract μ from [equation 2.14](#)

$$\mu = \frac{1}{en_e \rho_{xx}}. \quad (2.16)$$

With ρ_{xx} and the field dependence of ρ_{xy} , see [figure 2.1\(b\)](#), we can extract n_e and μ without knowing anything about a material other than the charge of its carriers e .

Another important quantity, extractable from measurements, is the mean free path, l_e , the mean distance traveled between consecutive scattering events. By combining [equation 2.7](#) and [equation 2.11](#) we find the following expression

$$l_e = v_F \cdot \tau_e = \frac{\mu \hbar k_F}{e}. \quad (2.17)$$

In [subsection 2.1.3](#) and [subsection 2.2.3](#), we will elaborate how to extract k_F and m^* from measurements of 2-dimensional electron gasses.

For bulk metals, τ_e , n_e , μ , and l_e are material constants, which can be looked up in literature. For semiconductors, they are tuneable parameters controlled by externally applied electric fields as well as the electrostatic potential from the surrounding heterostructure. Therefore, the extractions from resistivity measurements are key in understanding the state of the carriers in a semiconductor in any given configuration.

2.1.2 Semiconductor transport

In the following subsection, we will cover semiconductors and their improvements over the past decades.

Semiconductors are characterized by having a small² band gap, E_G , around the Fermi energy, separating conduction band and valence band. Bulk semiconductors are thus insulating when E_C is the largest energy scale, since all available electron states are occupied. Through electrostatics, eg. from the surrounding heterostructure or from a field effect transistor (also called a gate), E_F can be pulled into either of the bands, thus enabling conductance.

In our structures, we occupy the conduction band; we label the bottom of the band E_C . By bringing E_F above but still close to E_C , low carrier density conductors can be created; low compared to the high carrier density of metals³. With many orders of magnitude decrease in carrier density, electron-electron scattering becomes insignificant, enabling a large electron mean free path l_e . Many quantum phenomena, some of which are presented in [section 2.2](#), depend on l_e being longer than the length scales associated with these phenomena.

On a quest for increasing l_e , the amount of scattering has to be reduced. Two significant scattering contributors had to be overcome: *impurity scattering* and *intersubband scattering*. Rather than tracking and reporting l_e , it is easier, as we saw above, to extract μ from magnetoresistivity

2 The definition of small varies but can be up to a few eV [15]

3 Charge carrier density of a metal is found by multiplying its atomic density $\sim 10^{22} \text{ cm}^{-3}$ [15] with its amount of valence electrons.

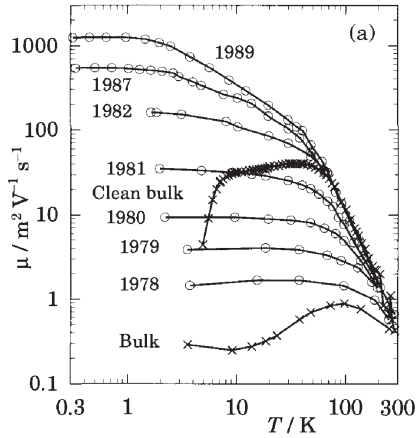


Figure 2.2: **Carrier mobility versus material quality:** Graph showing carrier mobility versus temperature, (\times) showing difference between 'Bulk' GaAs and 'Clean bulk', and (\circ) showing the improvements in 2DEG heterostructure growths. [Re-print from ref. [14]].

measurements. Combining [equation 2.11](#) and [equation 2.17](#), we see that l_e and μ are linearly proportional

$$\mu = \frac{e}{m^* v_F} l_e \quad (2.18)$$

Impurity scattering can be understood through Bloch's theorem. Impurities break the lattice periodicity thus causing scattering. Clean materials are therefore needed to optimize transport properties and have been a major focus of research over the past decades. Development of crystal growth techniques such as Molecular Beam Epitaxy (MBE) enables mono layer deposition of various elements on substrate. Doing the deposition inside ultra-high vacuum ($\sim 10^{-10}$ to 10^{-12} Torr) chambers enabled huge improvements in the cleanliness of materials. The mobility improvement is clearly displayed by the bulk data (\times) in [figure 2.2](#). The cleaner bulk has more than an order of magnitude increased mobility.

Before elaborating *intersubband scattering*, we'll recall what a subband is. Let us assume we have carriers moving in a bulk material along the x - y -plane. They are degenerate due to the lack of confinement. By confining the carriers transverse to their travel direction, along the z -direction, discrete energy-levels called subbands are formed. Intersubband scattering is scattering between these subbands and was first experimentally verified in 1982 [18]. The obvious solution is to design materials with only a single occupied subband. This has been achieved by embedding quantum wells, along the growth direction, in heterostructures. Such heterostructures are what enables mobilities larger than 10^6 cm²/Vs as shown by (o) data in [figure 2.2](#). Heterostructure quantum wells are further elaborated below in [subsection 2.1.3](#).

Even though a low electron density is key in obtaining high mobilities, the density can be too low. By decreasing n_e , we decrease the radius of the Fermi sphere. At some point the radius k_F becomes comparable to the Thomas-Fermi wave number q_{TF} [14]. When $k_F \sim q_{TF}$ fluctuations have a higher probability of flipping the momentum of the carriers. This prevents them getting from A to B, thus decreasing the mobility.

One last thing worth addressing is how to realize electrical contacts between metal and semiconductor. For most semiconductor-metal junctions, a *Schottky barrier* [14, 16] is formed at the interface. The metal work function is greater than that of the semiconductor, whose conduction band is pulled up at the interface causing a resistive contact. Through annealing a dirty but low resistance interface can be made. One exception is the semiconductor InAs, which has a surface accumulation layer, with increased free carrier concentration, that negates the Schottky barrier, and allows for a low resistive metal contact through regular metal deposition.

2.1.3 2-Dimensional Electron Gas

The confinement given by a heterostructure quantum well removes one degree of freedom from the carriers, giving them a 2-dimensional nature.

Assuming confinement in \hat{z} -direction from an L_z wide infinite quantum square well, the quantized energy of the n^{th} mode becomes [19]

$$E_n = \frac{\hbar^2 \pi^2 n^2}{2m^* L_z^2}. \quad (2.19)$$

Besides enabling enhanced mobilities, these 2-dimensional electron gasses (2DEGs) give rise to new physics such as the quantum Hall effect⁴, elaborated in subsection 2.2.4. Quantum wells are engineered by stacking materials with different conduction band energies $E_{C_1} < E_{C_2}$. One way is to sandwich the E_{C_1} material with E_{C_2} material forming a square well. Placing E_F in between the two conduction bands accumulates carriers only in the material with E_{C_1} . Different quantum well shapes have been used over the years. The highest reported mobilities have been achieved in GaAs/AlGaAs interfaces with triangular quantum wells [20, 21]. Among more recent high-mobility candidates, InAs quantum wells [22–24] and graphene encapsulated in hBN [25, 26], both have square quantum wells.

Carriers in a 2DEG are well described by a finite square well. By orienting our coordinates for the well is grown along \hat{z} , the energy of subband n becomes:

$$E_n(k_x, k_y) = \frac{\hbar^2 |\mathbf{k}|^2}{2m^*} + E_n, \quad (2.20)$$

As elaborated in all solid state text books, eg. ref [15, 17], a 2-dimensional Fermi sea has the following electron density:

$$n_e = 2 \frac{1}{(2\pi)^2} \pi k_F^2 = \frac{k_F^2}{2\pi} = \frac{E_F m^*}{\pi \hbar^2}, \quad (2.21)$$

resulting in an energy-independent density of states:

$$\mathcal{D}_{2D}(E) = \frac{dn_e}{dE} = \frac{m^*}{\pi \hbar^2}. \quad (2.22)$$

⁴ Two Nobel prizes were awarded for discoveries of quantum Hall effect: Integer quantum Hall effect in 1985: <https://www.nobelprize.org/prizes/physics/1985/summary/> Fractional quantum Hall effect in 1998: <https://www.nobelprize.org/prizes/physics/1998/summary/>

From [equation 2.21](#), we can extract k_F of a 2DEG by knowing its density, extractable from Hall measurements, see [equation 2.15](#). With k_F and m^* we can, with [equation 2.7](#), extract v_F and l_e

$$k_F = \sqrt{2\pi n_e}, \quad (2.23)$$

$$v_F = \frac{\hbar\sqrt{2\pi n_e}}{m^*}, \quad (2.24)$$

$$l_e = \frac{\mu\hbar\sqrt{2\pi n_e}}{e}. \quad (2.25)$$

For this thesis, we chose to work with InAs 2DEGs. Many reasons (all of which are elaborated in [section 3.1](#)) lie behind this choice, one of them being the high spin-orbit coupling, which is the topic of the following subsection.

2.1.4 Spin-Orbit coupling

Spin-orbit (SO) coupling is a relativistic effect known from atomic physics; an electron orbiting its atom, will in its own rest frame experience the atom orbiting itself. Thus the electron experiences a magnetic field that couples to its spin. A similar effect happens for electrons moving through charged environments in materials, experiencing electrical fields[16].

As mentioned in [subsection 2.1.3](#), quantum wells are formed in heterostructures by sandwiching materials with respective band offsets. The offsets, holding the carriers in place, are effectively applying an electric field on the carriers, pushing them into the well. Another field, that can be applied perpendicular to the 2DEG plane, is the field from a field effect transistor. Both the internal and the external electrical fields add a Rashba spin-orbit term to the Hamiltonian[16]:

$$H_R = \alpha_R(\sigma_x k_y - \sigma_y k_x), \quad (2.26)$$

with σ_x and σ_y being the Pauli matrices, in the plane of the 2DEG. From [equation 2.26](#), we see that the Rashba spin orbit coupling will align spins in the plane of the 2DEG, but orthogonal on the current direction.

Another contribution, known as Dresselhaus spin orbit coupling, stems from a lack of inversion symmetry in the crystal structure [16]. In bulk InAs, Rashba spin orbit dominates Dresselhaus spin orbit [16]. To verify whether this is also the case for our shallow InAs 2DEG with Al on top, we measured the magnetic field dependence on Coulomb blockade peaks of a charged island [27]. From varying the magnetic field directions, we found Rashba to be the dominating spin-orbit contributor and estimated a lower bound of $\alpha_R = 120 \text{ meV}\text{\AA}$, for these hybrid systems.

With the basics of 2DEG transport covered, we can now look at how it is altered by the application of magnetic fields.

2.2 MAGNETIC FIELD INDUCED PHENOMENA IN 2DEGS

A zoo of phenomena can emerge when magnetic fields are applied to 2DEGs, especially if the carriers have a sufficiently long l_e . This section will recap the ones that are important for the research presented in this thesis.

2.2.1 Zeeman

At zero magnetic field, the spin-states of freely moving electrons are degenerate. By exposing them to a uniform field, \mathbf{B} , the spins will precess around the field axis leading to a Zeeman split of the spin energies[16]

$$E_Z = \pm \frac{1}{2} g \mu_B \mathbf{B}, \quad (2.27)$$

with g the g-factor ($g \sim 2$ for metals) and μ_B the Bohr magneton. As for their mass, quasi particles in semiconductors also have a material dependent effective g-factor⁵, g^* . In [equation 2.27](#), the energy of states with spins pointing along \mathbf{B} is decreased while states with opposing spins have their energies increased.

⁵ Both sign and amplitude can vary, with some amplitudes being smaller than 2 and others being more than an order of magnitude larger.

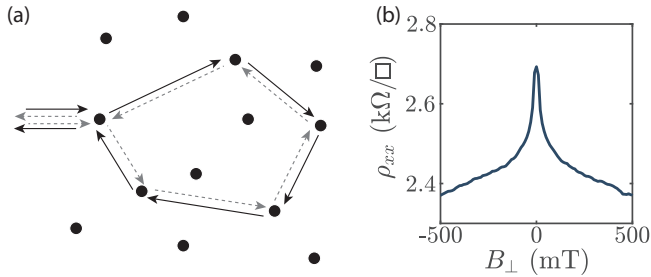


Figure 2.3: **Weak localization:** (a) Schematic showing time reversal symmetric clockwise and anti-clockwise paths in a diffusive system. (b) Data from a depleted Hall bar showing a weak localization resistance peak at $B_{\perp} = 0$.

2.2.2 Weak Localization

From the Lorentz force, [equation 2.8](#), we know that magnetic fields curve the path of moving charges. By pausing the particle's motion and letting time run backwards, the particle would not follow the original path back. Therefore, time reversal symmetry is broken by magnetic fields. One effect showing the breaking of time reversal is *weak localization*.

In a diffusive material, there is a finite probability that an electron, through consecutive scattering events, propagates along a circular path, sending the electron back where it came from, see [figure 2.3\(a\)](#). This leads to an increase of resistance, since electrons going in circles have a lower probability of transmitting. Going clockwise and anti-clockwise cannot be distinguished due to time-reversal symmetry. The two paths interfere constructively thus further increasing the probability of an electron taking the loop. This phenomenon is called weak localization.

The application of a magnetic field breaks time reversal symmetry and therefore decreases the resistance leading to a peak around zero field, see [figure 2.3\(b\)](#).

The role of interference dictates a strong dependence on the phase coherence length ξ . For weak localization to be present, the relation $\xi > l_e$ has to be fulfilled, since large l_e would only lead to long circular paths

under which phase would be lost, making interference impossible. Both the height in resistance and the width in B is increased with decreasing l_e [16].

2.2.3 Shubnikov-de Haas oscillations

As discussed in [subsection 2.1.1](#), we expect ρ_{xx} to be constant in B while ρ_{xy} has a linear dependence. Such an assumption is true for small fields, until $\omega_c \tau_e \sim 1$, with $\omega_c = |e|B_{\perp}/m^*$ being the cyclotron frequency. From here on, electron orbits are formed with new eigenenergies [16]

$$E_n = \hbar\omega_c \left(n + \frac{1}{2} \right), \quad (2.28)$$

equal to those of a harmonic oscillator with $n = (0, 1, 2, \dots)$ being the excitation level. The absence of a k -dependence of the energy indicates that states with different k , but same n , are degenerate. These form the so-called *Landau levels*, see [figure 2.4\(a\)](#).

To extract the amount of occupied filled Landau levels at a given B_{\perp} and n_e , we define the number of allowed states, per level, per unit area [16]:

$$n_L = \frac{|e|B_{\perp}}{h}. \quad (2.29)$$

The number of occupied Landau levels, called the filling factor, is given by

$$\nu = \frac{n_e}{n_L} = \frac{n_e h}{|e|B_{\perp}}. \quad (2.30)$$

Since E_n and the capacity of each level increases with B_{\perp} , fewer and fewer levels are occupied and ν decreases. This causes E_F to oscillate as a function of B_{\perp} , as shown with the dashed line in [figure 2.4 \(a\)](#).

Until now, we have not taken the spin degeneracy into account and all Landau levels would be doubly occupied, so ν would only jump between even values. When Zeeman energy, $g^* \mu_B B$, becomes comparable to the

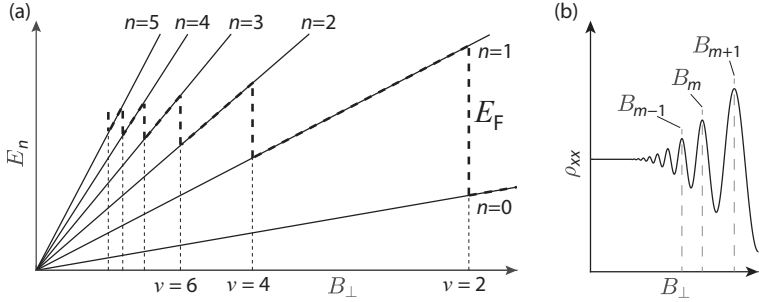


Figure 2.4: **Landau levels.** (a) Energy of spin-degenerate Landau levels as a function of B_\perp , called a Landau fan, for a selection of n_e . The dashed line shows how the Fermi energy oscillates with B_\perp at a fixed n_e . [Inspired by figure 16.5 from [16]] (b) Shubnikov de Haas oscillations of ρ_{xx} in B_\perp , calculated by equation 2.33. The oscillations peak at certain fields B_m which are indicated.

Landau level spacing, $\hbar\omega_c$, odd levels are distinguishable, enabling odd values of ν . The new eigenenergies are

$$E_n^\pm = \hbar\omega_c \left(n + \frac{1}{2} \right) \pm \frac{1}{2} g^* \mu_B B_\perp, \quad (2.31)$$

and the density of states:

$$\mathcal{D}_{2D} = \frac{|e|B_\perp}{h} \sum_{n,\sigma=\pm} \delta(E - E_n^\sigma). \quad (2.32)$$

The presence of disorder, lifts the k -degeneracy and gives the delta peaks of equation 2.32 a Gaussian broadening and their widths and heights increase with B_\perp . As the density oscillates, so does ρ_{xx} [16]:

$$\rho_{xx}(B_\perp, T, n_e) = \frac{m^*}{n_e e^2 \tau_0} \left[1 - 2e^{-\frac{\pi}{\omega_c \tau_q}} \frac{2\pi^2 k_B T / \hbar\omega_c}{\sinh(2\pi^2 k_B T / \hbar\omega_c)} \cos\left(2\pi \frac{\hbar n_e}{2eB_\perp} \right) \right], \quad (2.33)$$

with k_B being the Boltzmann constant, τ_q the lifetime of the quantum state and $\tau_0 = \tau_e(B=0)$. A plot of $\rho_{xx}(B_\perp)$ is shown in figure 2.4(b),

displaying *Shubnikov-de Haas* oscillations. Variable values were chosen to highlight the increase of oscillations width and amplitude with B_{\perp} . From Shubnikov-de Haas oscillations, n_e and m^* can be extracted.

Extracting electron density. From [equation 2.33](#), we see that Shubnikov-de Haas oscillations have the period: $2\pi \frac{\hbar m}{2|e|B_{\perp}}$. By extracting the fields B_m for which the oscillations peaks, indicated in [figure 2.4\(b\)](#). Plotting $1/B_m$ as a function of m one should find a linear slope

$$\Delta \left(\frac{1}{B_{\perp}} \right) = \left| \frac{1}{B_{m+1}} - \frac{1}{B_m} \right| = \frac{2|e|}{\hbar n_e}, \quad (2.34)$$

from which n_e can be extracted.

Extracting effective mass. The amplitude of Shubnikov-de Haas oscillations:

$$A(T, B_m) = 2e^{-\frac{\pi}{\omega_c \tau q}} \frac{2\pi^2 k_B T m^* / \hbar |e| B_m}{\sinh(2\pi^2 k_B T m^* / \hbar |e| B_m)}, \quad (2.35)$$

is reduced by increasing temperature. The relative amplitude, measured at different temperatures T and T_0 (the base temperature of the setup) becomes:

$$\frac{A(T, B_m)}{A(T_0, B_m)} = \frac{T \sinh(2\pi^2 k_B T_0 m^* / \hbar |e| B_m)}{T_0 \sinh(2\pi^2 k_B T m^* / \hbar |e| B_m)}. \quad (2.36)$$

By measuring and plotting the relative amplitude versus T , [equation 2.36](#) can be used to fit the data with m^* being the only fit parameter.

Next, we will look into how the transport in a clean 2DEG is altered in large fields.

2.2.4 Integer Quantum Hall Effect

Assume we have a clean and low density 2DEG. When applying B_{\perp} on the order of tesla the longitudinal resistivity, ρ_{xx} , of a mesoscopic Hall bar is zero each time the Landau levels are filled. Consequently, the Hall resistivity ρ_{xy} obtains plateaus with the value $\rho_{xy} = h/ve^2$, see [figure 2.5\(a\)](#). This is called the *integer quantum Hall effect*, and was the first observation of a topological insulator.

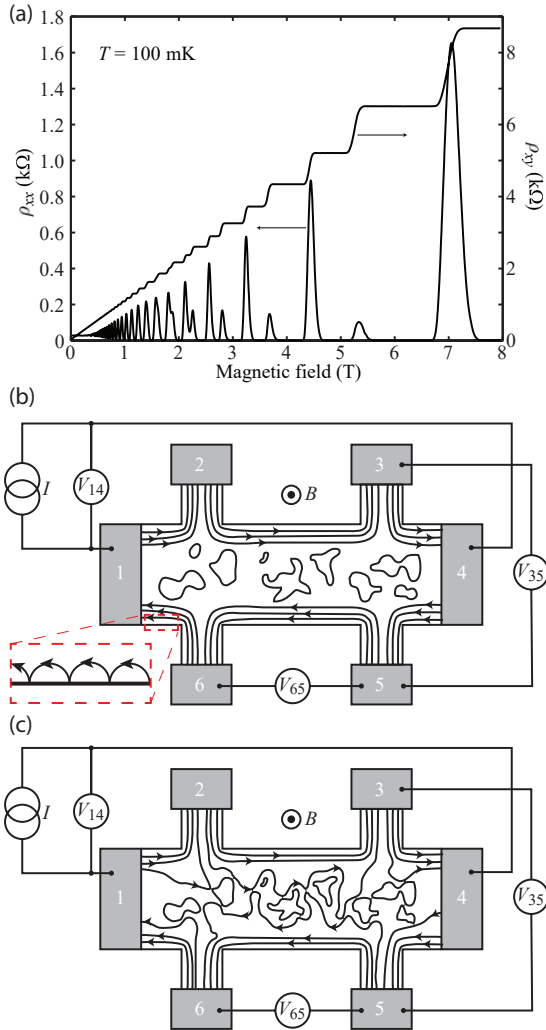


Figure 2.5: **Integer quantum Hall effect.** (a) Longitudinal and Hall resistivity versus applied magnetic field showing ρ_{xy} plateauing as $\rho_{xx} = 0$, hallmarks of the integer quantum Hall effect. (b) Transport in a 2DEG in the quantum Hall state where all bulk states are localized. Opposite edge currents travel in opposing directions. Inset sketches skipping motion of edge electrons. (c) Situation where bulk is conducting, enabling coupling the opposite edge current. Adapted from [16].

A simple explanation is the following. As B_{\perp} is increased, the cyclotron orbit radius

$$r_c = \frac{v_F}{\omega_c} = \frac{\hbar k_F}{|e|B_{\perp}} = \frac{\hbar\sqrt{2\pi n_e}}{|e|B_{\perp}} \quad (2.37)$$

decreases. For a clean 2DEG, eventually, electrons in the bulk are localized in orbits while the outermost states conduct along the edges, see [figure 2.5\(b\)](#). The inset shows a semi-classical picture of the edge electrons performing skipping orbits. Due to the edge states, the probe potentials have the following correlation: $V_1 = V_2 = V_3$ and $V_4 = V_5 = V_6$. It follows that $\rho_{xx} = \frac{V_6 - V_5}{I} = 0$ and $\rho_{xy} = \frac{V_3 - V_5}{I} \neq 0$. The size of ρ_{xy} is determined by the filling ν . Each filled Landau level adds a single conducting electron channel, each with h/e^2 resistance in parallel, leading to

$$\rho_{xy} = \frac{1}{\nu} \frac{h}{e^2}. \quad (2.38)$$

In between the B_{\perp} with $\rho_{xx} = 0$ in [figure 2.5\(a\)](#), there are regions of finite ρ_{xx} , suggesting a conducting bulk. This is possible, when a Landau level is partially filled, leading to coupling between opposing edge states as shown in [figure 2.5\(c\)](#). In systems with significant disorder, frequent scattering disables the bulk states from achieving fully isolated orbits, thus coupling the opposing edges. This results in a finite ρ_{xx} , even for B_{\perp} in between the lowest Landau levels.

Semiconductors are versatile materials, but lack some certain properties, such as ferromagnetism and superconductivity⁶. In the following two sections, we will elaborate superconductivity and how to induce it into semiconductors.

2.3 SUPERCONDUCTIVITY

2.3.1 *Discovery of superconductivity*

Back in 1908, Heike K. Onnes was the first person to liquefy Helium, giving him a way of cooling down materials towards 1 K. This led to the

6 Exceptions are twisted bi-layer graphene showing superconductivity [28], and certain twist angles between hexagonal boron nitride and twisted bi-layer graphene, showing ferromagnetism [29].

discovery of superconductivity⁷ in 1911, when he measured the resistance of mercury vanishing when cooled below a critical temperature T_c [30]. In the following century, more advanced cooling techniques (such as dilution refrigeration [31]) and many more experiments led to the discovery of superconductivity in multiple materials. Various elements and alloys were found to superconduct when cooled below a material-specific critical temperature. Figure A.1 shows T_c of elements at ambient pressure.

2.3.2 Bardeen-Cooper-Schrieffer theory

While superconductivity became a more and more wide spread phenomenon, it was not before 1957 that a self-consistent microscopic theory for superconductivity was developed; the Bardeen-Cooper-Schrieffer (BCS) theory⁸[32, 33].

Superconductivity arises when electron of opposite momentum and spin ($k \uparrow, -k \downarrow$) pair up in effective bosons called Cooper pairs. The pairs, having zero spin, have bosonic properties, enabling them to condense into a single ground state with a common phase ϕ . The material dependent paring energy, $\Delta \sim 3.3k_B T_c$, was found to be phonon mediated in simple s-wave superconductors. A quasi-classical description of the paring is that an electron pulls on a positively charged atomic core when traveling past it. Another electron traveling past the same core feels the positive charge of the displacement. Its path is thus correlated to the path of the initial electron, thereby coupling the two electrons. Thermally induced vibrations would wash out this effect, explaining the existence of the critical temperature T_c .

The above-mentioned electron-electron correlations are included through a mean-field $\Delta_k = \langle c_{k\uparrow}^\dagger | c_{-k\downarrow}^\dagger \rangle$, with c^\dagger being the fermionic creation op-

⁷ Awarded Nobel prize in 1913: <https://www.nobelprize.org/prizes/physics/1913/summary/>

⁸ Awarded the Nobel prize in 1972: <https://www.nobelprize.org/prizes/physics/1972/summary/>

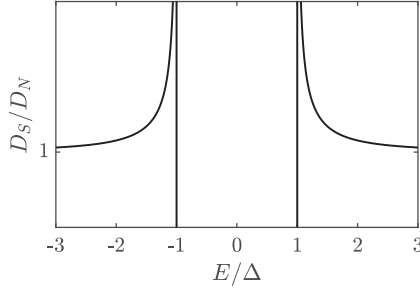


Figure 2.6: **BCS density of states** at zero temperature, calculated from [equation 2.41](#). Energy is normalized with Δ , while density of states is normalized to the normal density of states, D_N .

erator. When added to the Schrödinger equation [2.2](#), we obtain the Bogoliubov-de Gennes equations,

$$\begin{pmatrix} H_{\mathbf{k}} & \Delta_{\mathbf{k}} \\ \Delta_{\mathbf{k}} & -H_{\mathbf{k}} \end{pmatrix} \begin{pmatrix} u_{\mathbf{k}} \\ v_{\mathbf{k}} \end{pmatrix} = E \begin{pmatrix} u_{\mathbf{k}} \\ v_{\mathbf{k}} \end{pmatrix}. \quad (2.39)$$

Assuming a uniformly distributed pairing $\Delta_{\mathbf{k}} = \Delta$, we find the eigenenergies

$$E = \pm \sqrt{\varepsilon_{\mathbf{k}}^2 + |\Delta|^2}, \quad (2.40)$$

with $\varepsilon_{\mathbf{k}} = \left(\frac{\hbar^2 |\mathbf{k}|^2}{2m^*} - \mu \right)$. From [equation 2.40](#) we can extract the fermionic density of states for the superconductor, shown in [figure 2.6](#),

$$D_S = \frac{dN}{dE} = \frac{dN}{d\varepsilon_{\mathbf{k}}} \frac{d\varepsilon_{\mathbf{k}}}{dE} = D_N \frac{E}{\sqrt{E^2 - |\Delta|^2}}. \quad (2.41)$$

Here, N is the total number of states and $D_N = \frac{dN}{d\varepsilon_{\mathbf{k}}}$ is the normal density of states. We see a gap of 2Δ opening up in the fermionic density of states around the Fermi energy. Therefore the pairing energy Δ is also called the superconducting gap.

Though BCS theory has revolutionized our understanding of elemental superconductors, it still has its limits. The microscopic theory can become complicated when describing certain phenomena arising from

spatial fluctuations. As such, we turn to a macroscopic description of superconductivity better suited for describing such phenomena.

2.3.3 Ginzburg-Landau theory

In 1950, some years before BCS theory, Ginzburg and Landau published a macroscopic theory (GL-theory)[34]. It treats the overall energy rather than details of the excitation spectrum making it suitable to describe superconductivity with spatial variations of magnetic field and order parameter.

GL-theory introduces a complex wave function

$$\psi(\mathbf{r}, t) = |\psi(\mathbf{r}, t)|e^{i\phi(\mathbf{r}, t)}, \quad (2.42)$$

as an order parameter, looking at superconductivity as a second-order phase transition. When the transition into a condensate happens, an arbitrary but global phase ϕ is solidified. This will become important in [subsection 2.4.4](#). From ψ , the local density of superconducting electrons is given by

$$n_s = |\psi(x)|^2. \quad (2.43)$$

Later in 1959, Gor'kov showed that GL-theory can be derived as a limiting case of BCS-theory [35], and found that the order parameter $\psi(\mathbf{r})$ is proportional to the BCS gap, $\Delta(\mathbf{r})$

2.3.4 Coherence length and penetration depth

In addition to a critical temperature, superconductors also have a critical magnetic field B_c . When exposed to a magnetic field $B > B_c$ they regain finite resistance and the magnetic field lines penetrates the bulk, see [figure 2.7\(a\)](#). When exposed to $B < B_c$, they expel the magnetic field lines from their bulk as perfect diamagnets, illustrated in [figure 2.7\(b\)](#). This is done by creating circulating surface supercurrents, producing a magnetic field to exactly oppose the applied field.

The expelling of magnetic field, called the Meissner effect, happens over a characteristic length scale, the London penetration depth [15]

$$\lambda_L(T=0) = \sqrt{\frac{m_e}{\mu_0 n_e e^2}}, \quad (2.44)$$

with μ_0 being the vacuum permeability. It is defined as

$$B(r) = B \exp(-r/\lambda_L), \quad (2.45)$$

where r is the distance inside of the superconductor from its surface.

Another important length scale is the Pippard coherence length, ξ_0 , over which the superconductor remains coherent. Through BCS theory, it is found to be [36]

$$\xi_0 = \frac{\hbar v_F}{\pi \Delta}. \quad (2.46)$$

For dirty materials, both of these length scales are altered by the mean free path l_e [36]

$$\frac{1}{\xi} = \frac{1}{\xi_0} + \frac{1}{l_e}, \quad \lambda \approx \lambda_L \sqrt{1 + \xi_0/l_e}. \quad (2.47)$$

Subsection 2.3.7 will elaborate further on the properties of thin and disordered superconductors. The ratio

$$\kappa = \lambda/\xi, \quad (2.48)$$

is called the GL-parameter. It separates superconductors into two groups:

$$\begin{aligned} \kappa < 1/\sqrt{2} &\rightarrow \text{Type I} \\ \kappa > 1/\sqrt{2} &\rightarrow \text{Type II} \end{aligned} \quad (2.49)$$

2.3.5 Type I and type II superconductors

As a function of applied field B , *Type I* superconductors have a discontinuous (2nd order) phase transition at B_c . The superconductor expels the magnetic field from its bulk until $B \geq B_c$, after which electron-electron

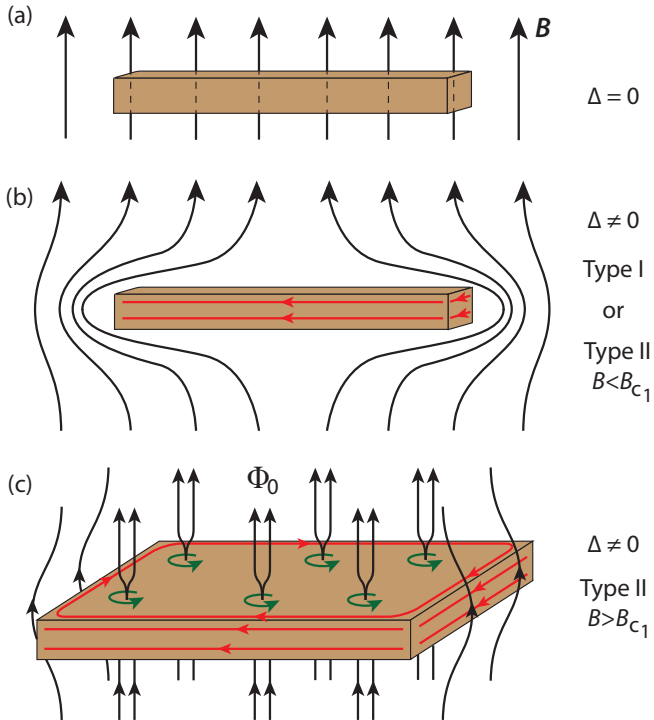


Figure 2.7: **Magnetic field on superconductors.** (a) When $\Delta = 0$, magnetic field lines penetrate the material. (b) For a type I superconductor, the Meissner effect excludes all field lines from the superconductor bulk by creating opposing surface currents. (c) For a type II superconductor with $B > B_{c1}$, pairs of quantized flux lines ($\Phi_0 = h/2e$) penetrate the bulk in certain places, creating local vortices of supercurrent. The rest of the field lines are expelled.

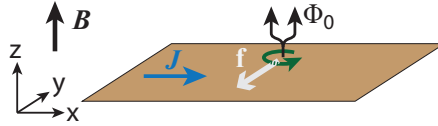


Figure 2.8: **Illustration of vortex flow** in a type II superconductor. A vortex with flux Φ_0 experience a Lorentz force pr. unit length f when a current density J is applied to the superconductor, see [equation 2.50](#).

correlations in the ground state disappears and cooper-pairs as such are split.

Type II superconductors, on the other hand, have a continuous (1st order) phase transition with two characteristic field scales, B_{c1} and B_{c2} , with $B_{c2} > B_c$ for type I. At low $B < B_{c1}$, all field lines are expelled, see [figure 2.7\(b\)](#). For $B_{c1} < B < B_{c2}$ flux quanta of $\Phi_0 = h/2e = 2.07 \text{ mT} \cdot \mu\text{m}^2$ penetrates the superconductor⁹, illustrated in [figure 2.7\(c\)](#). The pierces the superconductor by creating a supercurrent vortex. At the center of the vortex, superconductivity is lost, but restores to Δ over a length scale ξ . Global superconductivity remains until $B = B_{c2}$, at which point the flux density is too large for a global superconducting phase to exist.

2.3.6 Vortex physics

Let's assume we have a type II superconductor in the vortex state with $B_{c1} < B_{\perp} < B_{c2}$, $\mathbf{B}_{\perp} = B\hat{\mathbf{z}}$. In the presence of an applied current density $\mathbf{J} = J\hat{\mathbf{x}}$, each vortex experience a Lorentz force per unit length [36]

$$\mathbf{f} = J\hat{\mathbf{x}} \times \Phi_0\hat{\mathbf{z}} = -f\hat{\mathbf{y}} \quad (2.50)$$

transverse to current direction. Local potential changes pins the vortices giving rise to an effective drag force. The potential changes could be due to material impurities, voids, etc., *pinning* the vortices in place. Due to

⁹ The exact value of Φ_0 , having $2e$ charge, is an experimental validation of electron paring

the drag, vortices settle at a velocity $v_{\perp} = -v\hat{y}$. Their movement induces an electric field [36]

$$\mathbf{E} = B\hat{z} \times (-v)\hat{y} = E\hat{x}, \quad (2.51)$$

parallel to the current, enabling charge dissipation. This *vortex flow* starts as soon as $B > B_{c1}$ and gives rise to a flow resistivity which increases with both B and J .

For a strong pinning force, vortices can be present without causing dissipation. If a large current is applied, vortices can be thermally activated to jump between pinning sites, called *vortex creep*.

2.3.7 Thin film/disordered superconductors

Until now, we have addressed bulk clean superconductors. The superconducting properties can change drastically by making the superconductor thin or disordered.

Enhanced critical fields: The parallel critical field of superconducting thin films with thickness $d < \lambda$ can be calculated from GL-theory[36]:

$$B_{c,\parallel} = 2\sqrt{6}\frac{B_c\lambda}{d}, \quad (2.52)$$

exceeding the thermodynamic critical field B_c .

Rather than increasing indefinitely, a so called *Pauli limit* or *Chandrasekhar-Clogston (CC) limit* is predicted for a maximal critical field, B_P [37, 38]. The limit is predicted to be the field for which the Zeeman energy (see equation 2.27) equals the gap, leading to

$$B_P = \frac{\Delta}{g\mu_B}, \quad (2.53)$$

with g being the g-factor. Observation of $B_{c\parallel} > B_P$ has been made in systems with high spin-orbit coupling [39, 40]. The authors claim that the spins are momentum locked in Rashba subbands due to high spin orbit energy; thus, weakening Zeeman breaking of superconducting Cooper pairs.

The temperature dependence of critical fields can with GL theory be determined for temperatures close to the critical temperature, $T \lesssim T_c$. This is determined by knowing the temperature dependence of the characteristic coherence length [36]

$$\xi^2(T) \propto \frac{1}{1 - T/T_c}. \quad (2.54)$$

Ref. [41] shows that the parallel and perpendicular field of a thin superconducting film is given by:

$$\begin{aligned} B_{c,\parallel} &= \frac{\sqrt{3}\Phi_0}{\pi d \xi(T)} \propto \sqrt{1 - T/T_c}, \\ B_{c,\perp} &= \frac{\Phi_0}{2\pi \xi^2(T)} \propto 1 - T/T_c, \end{aligned} \quad (2.55)$$

with the temperature dependence found by implementing [equation 2.54](#). With $B_{c,\parallel}(T)$ and $B_{c,\perp}(T)$ the thickness of the thin superconducting film can be extracted:

$$\frac{B_{\perp}}{B_{\parallel}^2} = \frac{\pi d^2}{6\Phi_0}. \quad (2.56)$$

As indicated by [equation 2.47](#), disorder resulting in a lower mean free path l_e , decreases ξ and increases λ . The resulting increased GL-parameter can potentially turn a type I superconductor into type II. One example is Al, a classic type I superconductor. By evaporating aluminum oxide (alumina) or by evaporating metallic aluminum in an oxygen atmosphere, granular aluminum was formed [42]. These films could sustain supercurrent with $B_{\perp} > 1$ T, a clear indication of type II superconductivity.

Effects on critical temperature: Besides increases in B_c , thickness d and disorder (evaluated by the sheet resistance, R_{\square}) also alters T_c of superconductors. A large dataset of experiments on different superconductors is collected in ref [43]. The authors claim a universal scaling of T_c with the sheet resistance R_s . Most of the datasets show T_c decrease as $d \rightarrow 0$. This could be reasoned by Hohenberg-Mermin-Wagner theorem stating that thermal fluctuations prohibits long-range phase coherence in systems with dimension ≤ 2 . Two exceptions in the dataset are studies of

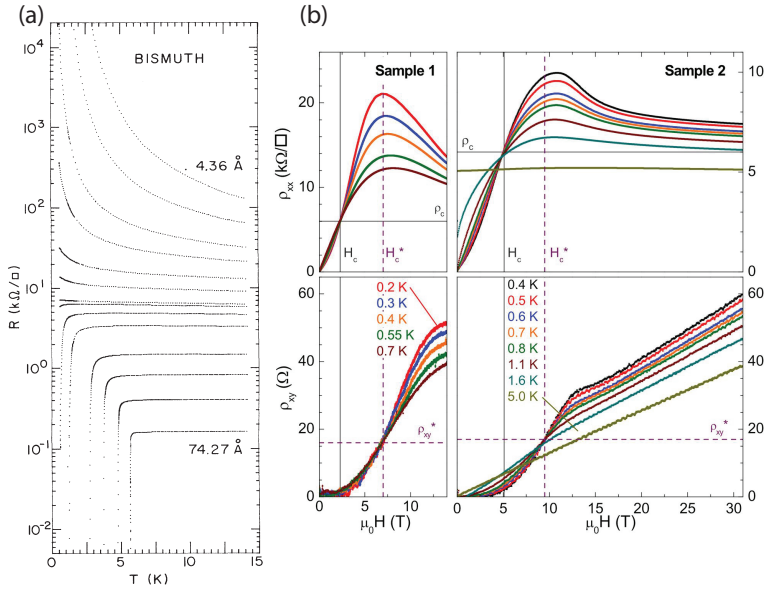


Figure 2.9: **Superconductor-Insulator Transition.** (a) Sheet Resistance of bismuth films of different thicknesses as a function of temperature. The figure is adapted from Ref [46]. (b) Hall and longitudinal resistivity of indium oxide films as a function of applied magnet field, measured at different temperatures. The figure is adapted from Ref [47].

aluminum [42, 44], showing an increase of T_c with d , eventually followed by a decrease as $d \rightarrow 0$. An increase of T_c for thin Sn has also been reported [45]. A theory explaining the inverse relationship between T_c and d for certain materials has not yet been developed.

Superconductor insulator transition: Some superconductors are so disordered that they, in their resistive state ($B > B_{c2}$) show insulating behavior, meaning that resistance increases as temperature drops. This gives rise to a so-call *superconductor-insulator-transition*. The transition can happen by varying different parameters, eg. thickness [46] or magnetic field [48], see figure 2.9. When driving the transition with magnet field, there is a characteristic crossover of isotherms in both ρ_{xx} and ρ_{xy} as shown in figure 2.9(b). According to our knowledge, in the current

literature [47–49], the crossover in ρ_{xx} always happens prior in field compared to ρ_{xy} .

2.4 HYBRID INTERFACES

With an understanding of transport in semiconductors and superconductors, in this section, we will look into transport through hybrids of the two. First we will go through the theoretical framework of Andreev reflection, BTK-theory and proximity effect, finally addressing two of the exotic states that is predicted to emerge from super/semi-hybrids: *Majorana modes* and *Andreev edge modes*.

2.4.1 Andreev reflection

What happens to an electron with energy $|E| < \Delta$, coming from a normal conductor, impinging on a superconductor? The superconductor doesn't have available fermionic states for the particle to jump into. It turns out that besides doing a normal specular reflection, see [figure 2.10\(a\)](#), there is a finite probability for the electron to undergo *Andreev reflection* [50], see [figure 2.10\(b\)](#).

With an Andreev reflection, the electron is retro-reflected as a hole, effectively transmitting two electrons into the superconductor in the form of a Cooper pair.

The reflected hole has opposite spin and momentum compared to the incoming electron and the two share a phase correlation, which will be elaborated in [subsection 2.4.3](#). Besides the opposite momentum, the hole also has opposite energy to E_F such that $E_e + E_h = E_F$, see [figure 2.10\(c\)](#).

2.4.2 BTK

Through the combined effort of Blonder, Tinkham and Klapwijk, a theory [51] was established giving the probability of an electron to Andreev reflect (A), normal reflect (B) or transmit (T) when hitting the interface to a superconductor. They introduced transmission without/with branch

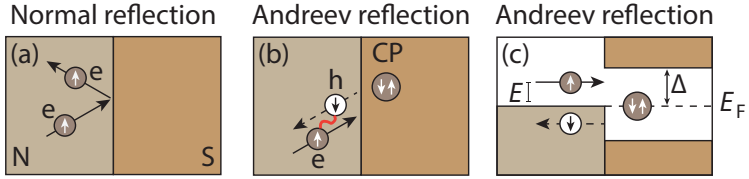


Figure 2.10: **Andreev Reflection.** (a) Normal specular reflection: An electron from a normal conductor (N) is reflected back into N at the superconductor (S) interface. (b) Andreev reflection: An electron from N is retro-reflected as a hole with opposite spin and momentum, effectively transmitting two electrons into S as a Cooper pair. The electron and hole is phase correlated, indicated by the red connection. (c) Energy of Andreev reflections: The electron from N has energy $E < \Delta$ and the reflected hole has energy $-E$.

crossing (C/D), but for simplicity, we will collect these into a combined transmission $T = C + D$. Collectively we have

$$A(E) + B(E) + T(E) = 1, \quad (2.57)$$

with E being the energy of the incoming carrier.

This *BTK theory* is derived for $T = 0$ and assumes ballistic normal- and superconductors. Scattering at the interface is introduced by a delta-shaped barrier

$$U(x) = \hbar v_F Z \delta(x = 0), \quad (2.58)$$

with a dimensionless size parameter (Z), see [figure 2.11\(a\)](#).

To describe the transport across a semiconductor(N)/superconductor(S) interface, a couple adjustments, summarized in ref [52], are needed. The significant carrier density difference between semi- and superconductor gives a Fermi energy difference, lifting the conduction band of the semiconductor leading to a potential step V_0 , see [figure 2.11\(a\)](#). The two potentials combined yields,

$$V(x) = V_0 \Theta(-x) + \hbar v_F Z \delta(x), \quad (2.59)$$

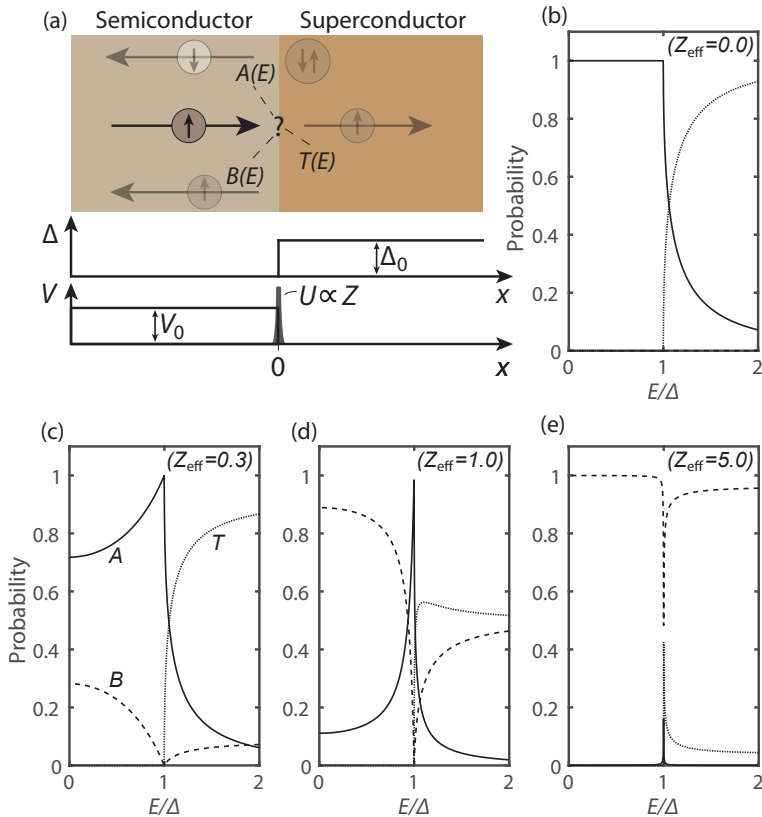


Figure 2.11: **BTK Theory** (a) Schematic showing BTK theory setup for calculating scattering amplitudes of an incoming electron from a semiconductor impinging on a superconductor. The amplitudes for Andreev reflect (A), normal reflect (B) or transmit (T), depends on energy (E) of the incoming electron, the interface barrier parameter (Z) and the conduction band offset (V_0). Pairing potential Δ_0 is assumed to be finite in the superconductor. (b-e) Plotting $A(-)$, $B(-)$, and $T(\dots)$ as a function of energy for different effective barrier parameters Z_{eff} .

With the superconductor present, we have to take both electron- and hole-like excitations into account, for which the Bogoliubov-de Gennes equations, [equation 2.39](#), are ideal. We utilize the Hamiltonian

$$H(x) = -\frac{\hbar^2}{2m^*} \nabla_r^2 - \mu + V(x), \quad (2.60)$$

as well as a step function shaped parring potential with $\Delta(x < 0) = 0$, $\Delta(x > 0) = \Delta_0$, see [figure 2.11\(a\)](#).

We look for solutions of the form [\[52\]](#),

$$\psi_{\text{in}}(x) = \begin{pmatrix} 1 \\ 0 \end{pmatrix} e^{ik_e x}, \quad (2.61)$$

for the incoming electron and the resulting reflected and transmitted waves:

$$\begin{aligned} \psi_{\text{r}} &= a \begin{pmatrix} 0 \\ 1 \end{pmatrix} e^{ik_e x} + b \begin{pmatrix} 1 \\ 0 \end{pmatrix} e^{-ik_h x} \\ \psi_{\text{t}} &= c \begin{pmatrix} u_0 \\ v_0 \end{pmatrix} e^{i\tilde{k}_e x} + d \begin{pmatrix} v_0 \\ u_0 \end{pmatrix} e^{-i\tilde{k}_h x}, \end{aligned} \quad (2.62)$$

with the wavenumbers given by:

$$\begin{aligned} k_e &= \sqrt{k_{\text{FN}}^2 + (2m^*/\hbar^2)E} \\ k_h &= \sqrt{k_{\text{FN}}^2 - (2m^*/\hbar^2)E} \\ \tilde{k}_e &= \sqrt{k_{\text{FS}}^2 + (2m^*/\hbar^2)\sqrt{E^2 - \Delta_0^2}}, \\ \tilde{k}_h &= \sqrt{k_{\text{FS}}^2 - (2m^*/\hbar^2)\sqrt{E^2 - \Delta_0^2}} \end{aligned} \quad (2.63)$$

with k_{FN} and k_{FS} being the Fermi wave number of the semi- and superconductor respectively.

The Schrödinger equation [2.60](#) with potential from [equation 2.59](#) can be solved by evaluating the boundary conditions at $x = 0$. The resulting probability amplitudes $A = |a|^2$, $B = |b|^2$ and $T = |c|^2 + |d|^2$ is listed in [table 1](#).

Andreev reflection	A	$\frac{ \eta ^2}{ 1+Z_{\text{eff}}^2(1-\eta^2) ^2}$
Normal reflection	B	$\frac{Z_{\text{eff}}^2(1+Z_{\text{eff}}^2) 1-\eta^2 ^2}{ 1+Z_{\text{eff}}^2(1-\eta^2) ^2}$
Transmission	T	$1 - A - B$

Table 1: Scattering probabilities for an incoming normal particle on a semi-/superconductor interface. $\eta = \frac{\Delta_0/\sqrt{E^2-\Delta_0^2}}{1+E/\sqrt{E^2-\Delta_0^2}}$. $Z_{\text{eff}} = \sqrt{Z^2 + (1-r)^2/4r}$, with the Fermi velocity mismatch $r = v_{\text{FN}}/v_{\text{FS}}$. Extracted from ref [52, 53].

A good intuition on Z_{eff} is found by setting S is in the normal state ($\Delta = 0$). We find that $\eta = 0$, which leads to the reflection and transmission probabilities

$$\begin{aligned}
 B &= \frac{Z_{\text{eff}}^2}{1 + Z_{\text{eff}}^2} \\
 T &= \frac{1}{1 + Z_{\text{eff}}^2}
 \end{aligned}
 \tag{2.64}$$

With [table 1](#), we can plot the scattering amplitudes (A, B, T) as a function of energy for different Z_{eff} , see [figure 2.11](#)(b-e). With $Z_{\text{eff}} = 0$, no normal reflections occurs, so at $E < \Delta_0$ only Andreev reflections occur. For $E > \Delta_0$ A decreases with energy as T becomes finite and increases.

For $Z_{\text{eff}} > 0$ normal reflection, B , is finite and increases monotonically as a function of Z_{eff} causing A and T to decrease, according to [equation 2.57](#). With $Z_{\text{eff}} = 5$, A only has a small contribution around $E = \Delta$, while $B \sim 1$ for $E < \Delta_0$ and dominates for $E > \Delta_0$ as well.

The peak of A and T around $E = \Delta_0$ for high Z_{eff} clearly indicates the size of Δ_0 , similar to the conductance peaks of the BCS density of states, [figure 2.6](#). This paragraph will show how the superconducting density of states D_S can be directly measured by *tunnel differential conductance*

spectroscopy. If a constriction is connecting two reservoirs with voltage difference V , the current through the constriction is given by

$$I = \frac{G_0}{e} \int_0^\infty [f(E - eV) - f(E)] T_t(E) dE, \quad (2.65)$$

with $f(E)$ being the Fermi distribution and $T_t(E)$ the probability of an electron with energy E to transmit through the constriction. If the two reservoirs are normal- and superconducting, the transmission coefficient can be expressed in terms of BTK parameters,

$$I = \frac{G_0}{e} \int_0^\infty [f(E - eV) - f(E)] [1 + A(E) - B(E)] dE, \quad (2.66)$$

with $A(E)$ adding to the transmitted current and $B(E)$ reducing it. Differential conductance is obtained by evaluating dI/dV . At low temperatures the Fermi distributions are well approximated by step-functions, leading to a differential conductance,

$$\begin{aligned} \frac{dI}{dV} &= \frac{G_0}{e} \int_0^\infty [e \cdot \delta(E - eV)] [1 + A(E) - B(E)] dE. \\ &= G_0 [1 + A(eV) - B(eV)] = G_{\text{NS}}. \end{aligned} \quad (2.67)$$

By plugging in the scattering coefficients and evaluating them for $Z \gg 1$, one finds

$$G_{\text{NS}} = G_0 \frac{1}{1 - Z^2} \frac{E}{\sqrt{E^2 - \Delta^2}} = G_{\text{N}} \frac{E}{\sqrt{E^2 - \Delta^2}}. \quad (2.68)$$

with the normal state conductance $G_{\text{N}} = G_0 \frac{1}{1+Z^2}$, using [equation 2.64](#). Through comparison with [equation 2.41](#), we see the direct correlation between NS tunnel conductance and the superconducting density of states, D_{S} :

$$\frac{G_{\text{NS}}}{G_{\text{N}}} (Z \gg 1) \approx \frac{E}{\sqrt{E^2 - \Delta^2}} = \frac{D_{\text{S}}}{D_{\text{N}}} \quad (2.69)$$

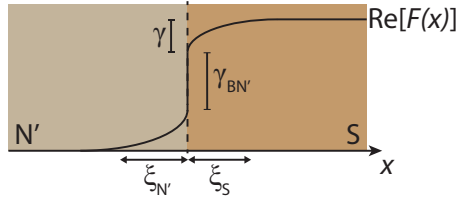


Figure 2.12: **Superconducting proximity effect** leads to a gradual change in the density of states for paired particles given by $\text{Re}[F(x)]$. The amount of correlated particles that leak from a superconductor (S) into an adjacent normal region (N') is defined by the proximity strength γ and the interface transparency $\gamma_{BN'}$. The coherence length of the respective materials $\xi_{N',S}$ act as the characteristic length scale over which $\text{Re}[F(x)]$ varies. Figure inspired by [52].

2.4.3 Proximity effect

An over-simplification of the BTK theory is the step-function parring potential across a NS junction, with Δ only residing in the superconductor. Parring also manifests in a normal conductor between the incoming electron and the reflected hole after an Andreev reflection as indicated in figure 2.10(b). The induced phase correlation decays over the phase coherence length of the normal conductor. This phenomenon is called the superconducting *proximity effect* and is well elaborated in ref [54].

In addition, ref [52] and its citations elaborates a Greens function approach to the BTK analysis, providing access to spacial information of the parring potential. The assumption is that at the surface or interface of a superconductor (S), a metallic region (N'), with width $d_{N'}$ is formed due to impurities, oxide or alloying. An S-N junction then becomes S- N' -N. Two angle-averaged Greens are introduced. The normal Greens function $G(E, x)$ and the anomalous Greens function $F(E, x)$.

The real part of G is interpreted as the quasi-particle density of states, $\text{DOS}(E, x) = \text{Re}[G(E, x)]$, while the real part of $F(E, x)$ is interpreted as density of states for paired particles $\text{DOS}_{\text{pair}}(E, x) = \text{Re}[F(E, x)]$.

Using Eilenberger equations [55], two important parameters are extracted [56]; the proximity strength:

$$\gamma = \frac{\rho_S \xi_S}{\rho_{N'} \xi_{N'}}, \quad (2.70)$$

and the interface transparency

$$\gamma_{BN'} = \frac{R_I}{\rho_{N'} \xi_{N'}}. \quad (2.71)$$

Here, R_I is the SN' interface area times its resistance, while $\rho_{N',S}$ and $\xi_{N',S}$ are the resistivities and the coherence lengths of the N' and S , respectively. The effect of γ and $\gamma_{BN'}$ is illustrated well in [figure 2.12](#). Besides the phase correlation added into N' , we see an *inverse proximity effect* as well, where $F(x)$ drops when moving towards the interface. The length scale over which $F(x)$ changes is the coherence length of the respective materials $\xi_{S,N'}$. Great experimental visualization of proximity effect with a very transparent interface is shown in ref [57].

For a narrow interface region $d_{N'} \ll \xi_{N'}$, the proximity strength and interface transparency parameters can be changed to [56]

$$\begin{aligned} \gamma_m &= \alpha \gamma d_{N'} / \xi_{N'} \\ \gamma_B &= \alpha \gamma_{BN'} d_{N'} / \xi_{N'} \end{aligned} \quad (2.72)$$

Here $\alpha = \ln(T_c/T_{c'})/\ln(2\gamma^*\Omega_d/\pi T_{c'})$, where $T_{c'}$ is the critical temperature of the N' region, $\Omega_d = \pi T_c (\xi_{N'}/d_{N'})^2$, and $\gamma^* \simeq 1.78$ is Euler's constant.

With the updated parameters [equation 2.72](#), ref [56] plots $\text{DOS}_{\text{Pair}}(E)$ in N' at various locations. [Figure 2.13](#) displays $\text{DOS}_{\text{Pair}}(E)$ at the SN' interface and at the free end of N' with fixed proximity strength $\gamma_m = 0.1$ but with varying γ_B . At the interface, the gap is hardly affected by γ_B , while the gap away from the interface is clearly reduced.

An observation, important for [subsection 2.4.5](#), is that $\text{DOS} \sim 0$ at low energies, even when the gap is significantly reduced by the increased γ_B . This is called a *hard gap*, whereas a gap with finite DOS is called a *soft gap*. One should keep in mind though, that the theory assumes zero

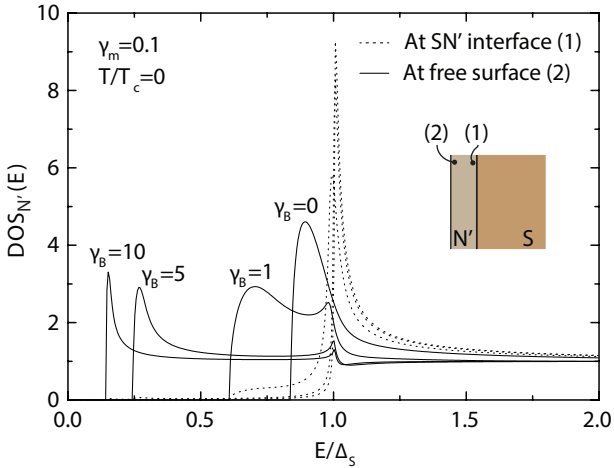


Figure 2.13: **Controlling induced gap** by varying the barrier transparency. Local density of states in N' is plotted as a function of energy for different interface transparencies γ_B and constant proximity strength $\gamma_m = 0.1$. Two locations, marked by inset, are included and distinguished by the legend. DOS is normalized by the normal state value while energy is normalized by the bulk superconducting gap Δ_S . Figure is adapted from refs [52, 56].

temperature and no disorder in the materials. A way to distinguish soft and hard gaps, derived by Beenakker [58], is to compare the conductance at $E \sim 0$ with that, far in the normal regime, $E \gg \Delta$.

The control of induced superconductivity into semiconductors have proven to be a challenging though crucial part of engineering material systems harboring exotic physics including topological states of matter.

2.4.4 *Josephson junctions*

A clear experimental evidence of the proximity effect, is the presence of a supercurrent in a material that by itself is resistive. This can be accomplished by sandwiching the resistive material (N) between two superconductors (S) separated by ζ . Assuming that both S-N interfaces are transparent and that $\zeta \lesssim \zeta_N$, a supercurrent is passed between the superconductors. It is carried by phase-correlated carriers transmitting from, and to, the superconductors via Andreev reflection.

Such a junction is called a *Josephson junction*, after B. D. Josephson who predicted the effect in 1962¹⁰ [59]. He derived a relation for the supercurrent, I_s , between two superconductors, separated by a thin insulator, with their GL-wavefunction phase difference $\Delta\phi$:

$$I_s = I_c \sin \Delta\phi, \quad (2.73)$$

where I_c being the maximal critical current of the junction. The relation was later found also to be true when the two superconductors are connected by a conducting material, as described above.

Like bulk superconductors, the Josephson junctions also have a critical temperature and a critical magnetic field beyond which they become resistive. Especially the field dependence gives rise to interesting physics. An applied magnetic field will wind the phase between the superconductors by sending flux through the junction. The flux, winding the phase, is scaled by the area A of the junction, with $\Phi = \mathbf{B} \cdot \mathbf{A}$. As seen by [equation 2.73](#), not only the magnitude, but also the direction of the current

¹⁰ Josephson was awarded half of the Nobel prize in physics 1973:
<https://www.nobelprize.org/prizes/physics/1973>

depends on $\Delta\phi$, with a period of 2π . When the phase difference $\Delta\phi$ is an integer multiple of π , the supercurrent goes to zero. At these phases, an integer multiple of flux quanta $\mathbf{B} \cdot \mathbf{A} = \Phi_0 = h/2e$ penetrates the junction, causing equal amount of supercurrent to flow in both directions, resulting in zero net current. This gives rise to a characteristic Fraunhofer diffraction pattern [36, 60, 61], known from optics:

$$\frac{I_c(\Phi)}{I_c(0)} = \left| \frac{\sin(\pi\Phi/\Phi_0)}{\pi\Phi/\Phi_0} \right| \quad (2.74)$$

When the Josephson weak link is made out of a semiconductor, the link can be depleted with an electrostatic gate. Such a Josephson junction can be operated as a superconducting transistor.

2.4.5 Majorana modes

Back in 1937, Majorana worked out a consistent theory of a new class of fermions [62], different from regular 1/2-spin Dirac fermions [63]. This Majorana fermion is charge-less and is its own anti-particle, giving it unique physical properties, including non-abelian statistics [64]. If two Majoranas interact and annihilate, they create a Dirac fermion or its anti-particle, eg. electron or hole. As mentioned in [chapter 1](#), one of the main motivations behind current research in superconductor/semiconductor hybrids is the realization of Majorana modes [5, 6, 65], and utilizing them to establish hardware for topological quantum computation [66–68].

With no experimental confirmation of Majorana fermions, yet, many physicist from different research-fields participate in the Majorana hunt [69]. With modern day nanotechnology, solid state physics serves as a promising platform for the realization of Majorana modes, with theoretical proposals suggesting what material combinations and device geometries to try out.

A good starting point for realizing a particle that is its own antiparticle is in a superconductor, where the definition of electron and hole is blurred. The Cooper pairs, with their bosonic nature, are not candidates, but fermionic excitations in the superconductors could be. These are

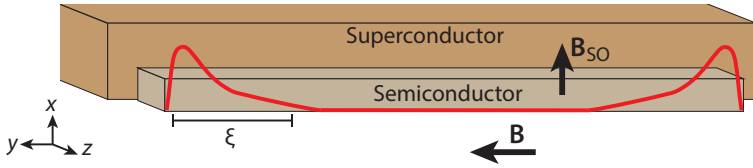


Figure 2.14: **Illustration of Majorana wire.** A 1D semiconductor wire with spin-orbit field \mathbf{B}_{SO} is proximity coupled to a s-wave superconductor. By application of external magnetic field \mathbf{B} Majorana modes form at the wire ends. The wave function spreads out according to the coherence length ξ .

electron- and/or hole-like, weighted by u and v from Bogoliubov-de Gennes theory, see [equation 2.39](#). In the search for Majorana modes, we therefore look for excitations with equal amount of electron and hole nature, living at zero energy [70].

Rather than conventional s-wave superconductivity, elaborated in [section 2.3](#), p-wave superconductivity with spinless pairing and finite angular momentum is needed. In 2001, Kitaev [65] predicted the boundary of one- and two-dimensional p-wave superconductors to host Majorana zero modes. All of the currently known bulk p-wave superconductor candidates are not suited for nano-fabrication, making them hard to implement in circuit elements. Instead, proposals have predicted p-wave pairing to emerge in hybrid systems. The general idea is to construct a system with a Hamiltonian, resembling that of a p-wave superconductor. This can be done by forcing the spin of s-wave paired electrons to align into effectively spinless channels. One proposal by Fu and Kane in 2008 [71], suggested combining topological insulators with s-wave superconductors while in 2010, two back-to-back publications [5, 6] suggested 1D semiconductor nanowires with strong spin-orbit coupling to be combined with superconductors.

The physical requirements, needed for realizing localized Majorana fermions in a hybrid system, is illustrated in [figure 2.14](#). To have well defined Majoranas at each end, the hosting semiconducting should be 1-dimensional. Dimensions along \hat{x} and \hat{z} should be small enough to only occupy the ground state mode, see [equation 2.19](#). Another constraint is

for the widths to be smaller than the superconducting coherence length, to induce a global superconducting gap. The length along \hat{y} , L_y , should be long enough to have a continuous spectrum of states, and $L_y > 2\xi$ is needed for the Majorana overlap to be small. The semiconductor should have strong spin-orbit coupling, which, due to the confinement, will be Rashba-type and the field B_{SO} will point along the \hat{x} - \hat{z} plane. For simplicity, a pure \hat{x} -orientation is chosen. Good spin-orbit candidates are InAs and InSb [16]. Lastly, a magnet field $\mathbf{B} = B\hat{y}$ is applied along the wire, and the chemical potential, μ , can be tuned by surrounding electrostatic gates. The resulting Hamiltonian, acting on Nambu spinners

$$\Psi = \begin{pmatrix} \psi_{\uparrow} \\ \psi_{\downarrow} \\ \psi_{\downarrow}^{\dagger} \\ -\psi_{\uparrow}^{\dagger} \end{pmatrix}, \quad (2.75)$$

becomes:

$$H = \underbrace{\left(\frac{\hbar^2 k_y^2}{2m^*} - \mu \right)}_{\text{Kinetic}} \sigma_0 \otimes \tau_z + \underbrace{\alpha_R k_y \sigma_x}_{\text{Rashba}} \otimes \tau_z + \underbrace{E_Z \sigma_y}_{\text{Zeeman}} \otimes \tau_0 + \underbrace{\Delta^* \sigma_0}_{\text{Induced gap}} \otimes \tau_x, \quad (2.76)$$

with σ and τ being the Pauli matrices in spin and particle/hole space, respectively; Rashba and Zeeman terms are from equation [equation 2.26](#) and [2.27](#), respectively, and Δ^* is the gap induced in the semiconductor.

The combination of Zeeman and Rashba, orthogonal to each other, splits the spin degeneracy and simultaneously supplies a spin texture. If μ is placed within the the Zeeman gap, then the spins are momentum locked. Adding superconductivity splits the bands around zero energy creating a gap of $2\Delta^*$. The gap is closed by Zeeman when

$$E_{Z,\text{topo}} = \sqrt{\mu^2 + \Delta^{*2}} \quad (2.77)$$

at which point we enter the topological regime. For higher fields, the gap reopens by flipping the electron and hole bands until B_c is reached and

$\Delta^* = 0$. At $E_{Z,\text{topo}} = \Delta^*$, states from the conduction and valence band meeting at $E = 0$.

To find states that stay at zero energy over an extended region in parameter space, we have to look at the edges of the wire. Let's assume we have $E_Z > E_{Z,\text{topo}}$ with flipped bands. At the edge of the wire where a topological non-trivial region is connected with a trivial one, the bands abruptly flip. This flip necessarily have to include a band crossing at $E = 0$, resulting in a zero energy state fixed at the ends of the 1D wire. This forms a so called *zero bias peak* in the local density of states. This is a fermionic mode formed by the wanted Majorana states. They are protected from other fermionic states by the effective p-wave gap, $\Delta'_p(B)$, assuming that we have a *hard* induced gap, defined in [subsection 2.4.3](#).

The size of the p-wave pairing in the topological region is given by [72]

$$\Delta'_p = \frac{\alpha_R \Delta^*}{E_Z}, \quad (2.78)$$

with the units $[\Delta'_p] = \text{Jm}$. Though needed to get into the topological regime, Zeeman also reduces the topological gap, while spin orbit strength and the induced s-wave gap both increase Δ'_p .

Both Δ^* and E_Z have a B -dependence. To maximize $\Delta^*(B)$ within the topological regime, it is favorable to reach the topological criterion, [equation 2.77](#), at a minimal magnetic field. This is done by tuning $\mu \sim 0$ and by using host-materials with high g-factors, making B more efficient in increasing E_Z , see [equation 2.27](#). Also for high g-factor, InAs and InSb are good candidates [16].

Regarding choice of superconductor, a big gap is preferable since $\Delta \propto \Delta^* \propto \Delta'_p$. But with a bigger Δ , a larger B is needed to enter the topological regime, [equation 2.77](#). As discussed in [section 2.3](#), the field dependence of a superconductor can vary significantly by the choice of material and its composition. It would be beneficial to use a superconductor with large B_c/Δ ratio. Then the gap would be reduced minimally, when $E_{Z,\text{topo}}$ is reached, thus maximizing Δ'_p .

One way to observe a zero-energy fermionic edge mode is to do local spectroscopy at the ends of a wire by measuring tunnel conductance as a function of B and μ . Δ^* and α_R are given by choice of material and can

therefore not easily be varied. First observation of a zero bias peak in a proximity coupled semiconductor wire was done in 2012 [73], followed by other observations over the years [74, 75]. It has since been shown, in theory, that unintentional dots in the wire can lead to states that mimic the zero bias peak behavior [76].

Other experiments, researching Majorana candidates with semiconductor/superconductor hybrids, have been done, including charged Majorana islands [27, 77, 78] and Majoranas formed at the ends of Josephson junctions [79, 80], the latter proposed in these theoretical papers [7, 8]. To get conclusive evidence of Majorana modes, more elaborate experiments are needed, putting even more demands on our materials [81].

2.4.6 Superconducting quantum Hall edge

To create Majorana modes at the boundary of a 2D system, rather than using a topological insulator (as proposed by Fu and Kane [71]), other proposal suggests combining quantum Hall effect with superconductors [82–84]. From such a hybrid, other interesting physics can be researched as well including *Andreev conversion* enabling exotic circuit elements [9]. Some experimental results were realized with Graphene/NbN hybrids [85]. We will address the physics of Andreev reflecting quantum Hall Edge states, and simultaneously mention some of the experimental challenges.

A clean superconductor interface with a high Andreev reflection probability is key for preserving electron-hole duality, illustrated in figure 2.15(b). As illustrated on inset of figure 2.5, a simplification of quantum Hall edge states interfacing an insulator/vacuum consist of electrons doing skipping orbits through consecutive normal reflections figure 2.15(a). By interfacing a superconductor instead, the edge states can Andreev reflect, alternating between being an electron and a hole, making the state on average charge-less. With opposite charge and wave number, the hole trajectory obtains a sign both from reversed momentum and reversed Lorentz force, equation 2.8, thus traveling the same direction as electrons. The presence of impurities adds normal reflection

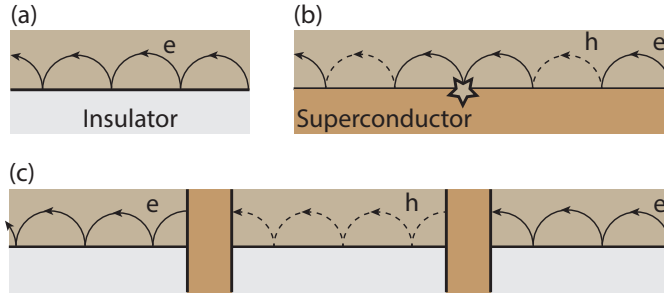


Figure 2.15: **Skipping orbits on different interfaces.** (a) Skipping orbit on an insulator. Electron is being reflected back as an electron. (b) Skipping orbit on a superconductor. When Andreev reflecting, the electron is reflected as a hole and vice versa, creating a charge-less edge state. Impurities, marked by the star, adds charge to the state through normal reflection. (c) Superconductor fingers overlapping the edge states can through Andreev conversion flip the charge of an edge state [9, 85]

probability that can be different for electron and hole thus adding finite charge to the state, illustrated in [figure 2.15\(b\)](#).

Another interesting geometry is having superconducting fingers interrupting the 2DEG, see [figure 2.15\(c\)](#). These can introduce Andreev conversion, flipping the sign of the edge states charge [9, 85]. With a broader finger, several Andreev reflections happen while the edge states pass it. The resulting charge depends on the parity of Andreev reflections and can eg. be controlled by an applied voltage [86] or magnetic field [84].

A magnetic field, usually on the order of teslas, is necessary to obtain quantum Hall effect (see [subsection 2.2.4](#)), but simultaneously counteracts superconductivity (see [subsection 2.3.4, 2.3.5, 2.3.6](#)). Inspecting [figure A.1](#), regular bulk elemental superconductors are not sufficient. Instead, disordered, thin or compound type II superconductor are needed. Even though B_{c2} is sufficiently large, another problem arises with the presence of vortices. If a vortex is within a coherence length of the interface, its

resistive core adds to the normal reflection probability [85], further complicating the matter.

As indicated from the last two subsection, advances in material science are needed to fully harvest the physics and applications that are hidden within the framework of superconductor/ semiconductor hybrids. The following chapter will address the current state of the art fabrication of shallow InAs 2DEG heterostructures with epitaxially grown Al, and elaborate how to measure and characterize them. We will look into their benefits, limitations, and introduce novel fabrication schemes that eases some of those limitations.

3

MATERIAL, FABRICATION AND EXPERIMENTAL SETUP

Nanofabrication ("Fab" in short): the design and manufacture of products and structures, especially electronic devices, with dimensions measured in nanometers¹.

We start, in [section 3.1](#), with presenting and discussing the material foundation: An InAs 2DEG heterostructure with *in-situ* grown epitaxial Al. Next, in [section 3.2](#), the state of the art, Fab recipe is elaborated. [Section 3.3](#) introduces the novel use of anodic oxidation to fab these hybrid materials. The final [section 3.4](#) describes the measurement setup used to characterize the products of fab.

3.1 MATERIAL STACK CONSIDERATIONS

3.1.1 *Choosing a material platform*

As mentioned above, a big demand is put on semi-/superconductor hybrids to host Majorana fermions, see [subsection 2.4.5](#). The first problem to solve is obtaining a clean and low-resistive interface between

¹ Definition from [dictionary.com](https://www.dictionary.com)

the superconductor and semiconductor to obtain a hard induced gap, recall [subsection 2.4.3](#). With a naturally forming Schottky barrier (see [subsection 2.1.2](#)), this problem seems hard to overcome. A huge breakthrough was made in 2014, proposed by T. S. Jespersen and executed by P. Krogstrup. Al was grown *in situ* on InAs² vapor-liquid-solid (VLS) nanowires [10]. A significant difference in sub-gap conductance was observed between *ex situ* evaporated Al with *in situ* grown Al, the latter having the subgap conductance meeting the measurement noise floor [87]. With optimal growth conditions the Al forms an epitaxial match with the InAs. Luckily, these conditions don't deteriorate the InAs and, as mentioned in [subsection 2.4.5](#), InAs is a promising candidate for hosting Majorana modes due to its high g-factor and large spin-orbit coupling.

Though promising, and useful for academic research, standard VLS nanowires are not a scalable solution when the goal is to make quantum computer hardware due to the need of manually placing each wire. *Selective area growth* (SAG) and *two-dimensional electron gases* (2DEG) are both grown as planar structures making them more scalable. The epitaxial match between *in situ* grown Al and InAs based SAG [12, 88] and shallow 2DEGs [11, 89], have proven to induce hard gaps as well. For this thesis we chose to work with the 2DEG platform due to (i) accessibility to high quality material, and (ii) decades of experience in the global community leading to easy characterization and evaluation of material quality.

Al is the only superconductor, so far, which has been implemented with a successful epitaxial match on InAs 2DEGs. Bulk Al facilitates a relatively small superconducting gap, Δ , low critical temperature, T_c , and small critical magnetic field B_c^3 . This motivates the search for other potential candidates. Recently, similar high interface transparencies were reported for hybrid VLS nanowires using materials other than Al such as Sn-InSb [90], Ta-InAs [91] and Pb-InAs [92]. Some of these were accomplished due to the use of *in situ* shadow evaporation, removing the need of stripping such as superconductor to make a junction. Shadow evaporation is currently not developed for planar growths such as 2DEGs.

2 As mentioned in [subsection 2.1.2](#), InAs naturally doesn't form a Schottky barrier.
 3 See [figure A.1](#) for comparison with T_c and B_c of other bulk elemental superconductors.

Ideas for future implementations of other superconductors are elaborated in [chapter 8](#).

Rather than choosing another superconductor, T_c and B_c of aluminum can be increased by growing thinner films [11]. Unfortunately, there is a limit to how thin an Al film can be grown. *In situ*, without its oxide layer formed, aluminum's tendency of dewetting is promoted for thinner films. A cooled substrate stage is key in avoiding dewetting⁴, but even with liquid nitrogen cooling, there is a limit to how thin a uniform layer can be grown. Once oxidized, the film is stable and keeps its shape, due to the formation of alumina, which self-saturates at a thickness of ~ 3 nm [93].

3.1.2 Shallow InAs-based 2DEGs

First, let us get familiar with the properties of bulk InAs. It is a III/V semiconductor with a narrow and direct gap, and its carriers have low effective mass, m^* , high effective g-factor magnitude, g^* , and a high Rashba coefficient, α ⁵, see [table 2](#):

a_{InAs}	$E_{G,\text{InAs}}$	m_{InAs}^*	g_{InAs}^*	α_{InAs}
6.06 \AA	0.42 eV	$0.023 m_e$	-14.9	117.1 e\AA^2

Table 2: Properties for bulk zinc-blende InAs, extracted from ref [16]. From left to right: Lattice spacing, Band gap, effective mass, g-factor and Rashba coefficient.

For the past couple decades, it has been custom to do proximity coupling to buried⁶ 2DEGs from the side [85, 94–101], see [figure 3.1](#). To obtain optimal transport properties, the 2DEG is buried deep, to isolate it from surface scattering. This approach comes with a loss in interface transparency.

⁴ When a surface layer dewets, it contracts from the underlying material surface, creating a non-uniform film.

⁵ $\alpha_R = \alpha \langle E \rangle$, with $\langle E \rangle$ being an averaged electric field [16]

⁶ Buried means that the 2DEG well-isolated from the surface, usually done to omit surface scattering.

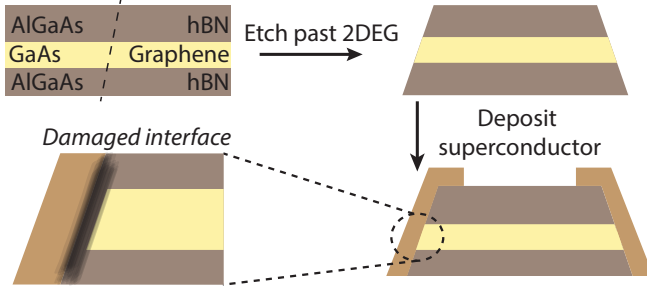


Figure 3.1: **Proximity coupling from sidewall.** Illustrating standard procedure to couple high-mobility buried 2DEGs to superconductors. First, a high mobility heterostructure is made, eg. GaAs/AlGaAs or Graphene/hBN. Etches can produce a slanted mesa wall on which a superconductor can be evaporated. Even with sophisticated cleaning, these interfaces usually come out damaged.

To optimize the proximity coupling, inspired by the results from nanowires [10, 87], J. Shabani grew shallow⁷ quantum wells hosting InAs 2DEGs [11], see figure 3.2(a). The electron wavefunction extends to the surface, where Al is deposited *in situ*. Initial studies verified a very transmissive interface [89, 102].

The cost of getting a good proximity-coupling is to have carriers close to the surface and thus susceptible to surface scattering, which greatly limits the carrier mobility. When stripping the Al, the surface III/V is exposed to the same process, and is prone to be disordered. This fact was shown by comparing mobility peak of an InAs 2DEG after Al etch with mobility peak of similar InAs 2DEG grown without Al to begin with [11]. The results, displayed in figure 3.2(b) clearly shows a degradation of the 2DEG from the Al etch. Another recent study confirms that shallow 2DEG carriers are sensitive to surface chemistry [103]. The authors find that changes in the surface chemistry from varying atomic layer deposition

⁷ In a shallow quantum well the 2DEG wave-function has a finite carrier density probability at the surface of the heterostructure.

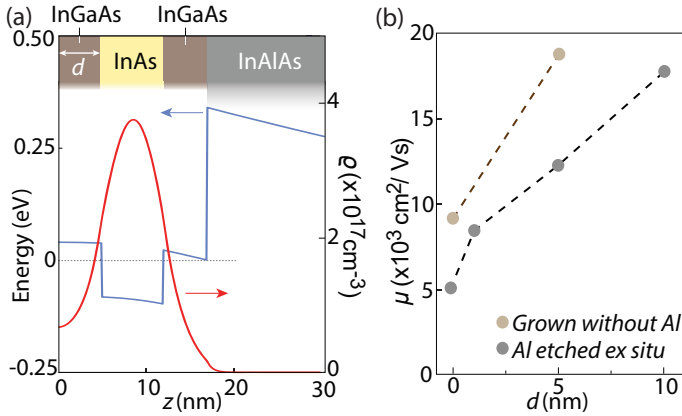


Figure 3.2: **Shallow InAs quantum well.** (a) Conduction band energy and carrier density probability along the growth direction in a shallow InAs/InGaAs 2DEG. Calculation done with self-consistent Schrödinger-Poisson solver. (b) Peak mobility measurement versus top barrier thickness from $\text{In}_{0.81}\text{Ga}_{0.19}\text{As}$. Two scenarios were tried. In one, III/V was grown without Al. In the other, III/V was grown with aluminum, which were later stripped. The figures are adapted from ref [11].

process (used to deposit dielectric for top-gating, see section 3.2) gives up to a factor 2 difference in mobility peak on the same material.

The mobility peak of shallow 2DEGs is usually lower than $5 \cdot 10^4 \text{ cm}^2/\text{Vs}$ once the Al is stripped [11, 79, 103, 104]. One way to decrease surface scattering, is to grow thicker quantum well barriers. By growing a fully buried InAs 2DEG, mobilities $\mu \sim 10^6 \text{ cm}^2/\text{Vs}$ have been achieved [22–24, 105]. That an order of magnitude higher mobility can be obtained by similar but buried 2DEGs indicates that the surface is our main source of scattering.

A big effort has been made by our 2DEG-team in Copenhagen and M. Manfra’s group from Purdue in trying out different barrier thicknesses and compositions, including both InAlAs and InGaAs barriers. Many considerations have to be taken into account. The proximity coupling should be strong enough to induce a hard gap. On the other hand, having

the coupling stronger than what is needed for optimal proximity effect gives disadvantages:

(i) As discussed above, shallow barrier carriers are more susceptible to surface scattering. (ii) The carrier quantities are affected by where they reside. For a strong coupling, the carriers will spend a lot of time in the Al, resulting in reduced g-factor and increased density, potentially leading to more than one mode being occupied in the 2DEG quantum well. (iii) Another effect to take into account is the Fermi velocity mismatch, mentioned in [subsection 2.4.2](#). A strong coupling to the superconductor would increase the 2DEG density and thus decrease the mismatch. Through decoupling, the BTK Z-parameter would increase; potentially more than originally intended with the addition of Fermi velocity mismatch due to a larger density difference.

3.1.3 *Choosing a growth substrate*

The foundation of MBE crystal growth is the substrate, dictating the initial lattice constant of a growth. Growing crystals, lattice mismatched to the substrate, can lead to strain and defects such as dislocations [106]. In the worst case, a non-planar growth will form. Two substrates, InP and GaSb, are regularly used for InAs growths and have lattice constants of 5.87 Å and 6.10 Å, respectively [16]. (Reminder for convenience: $a_{\text{InAs}} = 6.06 \text{ \AA}$).

InP is insulating with a band gap $E_{G,\text{InP}} \sim 1.3 \text{ eV}$. Of the two, it has the largest lattice mismatch, requiring additional growth engineering to enable clean InAs growth. Specifically for microwave resonator technology, Fe-doped InP was tested superior to GaAs and GaSb substrates. Ref [107] extracted a quality factor of $Q \approx 6.4 \cdot 10^4$, sufficient for circuit quantum electrodynamics.

GaSb is an interesting substrate candidate as well. Firstly, it is very well lattice-matched with InAs, enabling high quality growths. The lattice match also enables growth of thick InAs layers [24]. AlSb ($a_{\text{AlSb}} = 6.14 \text{ \AA}$, $E_{G,\text{AlSb}} = 1.69 \text{ eV}$), also matches well and makes efficient barriers

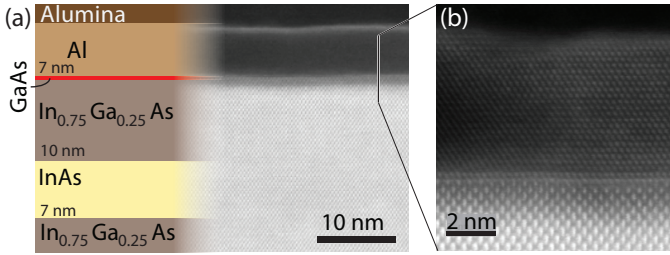


Figure 3.3: **Material of choice: M26.** (a) Stack and cross sectional transmission electron microscopy of the topmost heterostructure. (b) High resolution transmission electron microscopy of the III/V-Al interface.

The transmission electron micrographs are courtesy of Dr. Rosa Diaz at the Electron Microscopy Facility at the Birck Nanotechnology Center, Purdue University.

with its high band gap. Being conductive, the substrate can be used as an electrode for back-gating, giving more control of the lateral carrier distribution while measuring. One complication is that the antimonides are chemically reactive materials. Especially AlSb oxidizes uncontrollably when exposed to atmosphere. Reactivity decreases substantially by adding a small ratio of Ga, making AlGaSb. A functional GaSb-based shallow InAs 2DEG has been demonstrated [108], using InGaAs top-barrier to allow for good proximity coupling.

3.1.4 Characterizing the material of choice

The stack that so far has given the highest mobility peak while maintaining a hard induced gap $\Delta^* \sim 200$ eV is called M26 and is shown in figure 3.3. Cross sectional transmission electron microscopy shows a clean and epitaxial interface between the III/V and Al.

Grown on InP substrate, a 7 nm InAs quantum well is sandwiched between two In_{0.75}Ga_{0.25}As barriers, with the top barrier being 10 nm thick. Before Al deposition, a couple monolayers of GaAs is grown, since

our choice for Al etch (elaborated in [section 3.2](#)) is made to etch Al on GaAs.

When receiving a new hybrid growth, a selection of devices is fabricated to extract important material parameters, including Hall bars, aluminum bars and spectroscopy devices. The characterization of M26 based on those devices will be presented below. Josephson junctions, see [subsection 2.4.4](#), with the weak link being the 2DEG, can also be measured to extract the induced gap from multiple Andreev reflection analysis [[102](#), [108](#)]. Fabrication and measurement setup will be elaborated below in [section 3.2](#) and [3.4](#) respectively.

Hall bar: As elaborated in [subsection 2.1.1](#) and [2.1.3](#), Hall bars can be used to extract carrier mobility μ , density n_e , and mean free path l_e . A Hall bar made out of M26, and its extracted properties, are shown in [figure 3.4](#). An AC current $I_{AC} \sim 10$ nA is sourced, longitudinal and Hall voltages (V_{xx} and V_{xy}) are measured as a function of top-gate voltage, V_{TG} , and applied perpendicular magnetic field B_{\perp} . This allows us to extract μ , n_e and l_e as a function of V_{TG} .

A mobility peak of $42 \cdot 10^3$ cm²/Vs is found at a density $n_e = 6.3 \cdot 10^{11}$ cm⁻², leading to a maximum mean free path of $l_e = 545$ nm. The shape of the mobility versus density curve in [figure 3.4\(e\)](#) is interpreted as follows. Starting from the lowest densities, μ is increased with n_e . In the Thomas-Fermi approximation for a 2D electron sea, screening is independent of density. The approximation is valid for $q < 2k_F$ [[14](#)]. Here, q is the change in momentum after a scattering event: $k_{init} + q = k_{final}$. By increasing n_e we also increase the Fermi wave number k_F (see [equation 2.23](#)), thus increasing the range of validity for constant screening. A saturation (peak) followed by a decrease of μ , with further increase of n_e , is due to the electron distribution being more significant at the surface scattering centers [[103](#)].

AG Al bar: As mentioned in [subsection 2.3.7](#), thin superconductors has an increased in-plane critical field. A quick way of determining $B_{c||}$ is to do a 4-terminal voltage V_{4t} measurement of a bar covered by as-grown (AG) Al, see [figure 3.5\(a\)](#). The Al on M26 has $B_{c||} \sim 2.55$ T. The critical perpendicular field $B_{c,\perp} \sim 40$ mT, see [figure 3.5\(b\)](#), is a lot smaller than $B_{c||}$ but still 4 times larger than the bulk B_c , see [figure A.1](#).

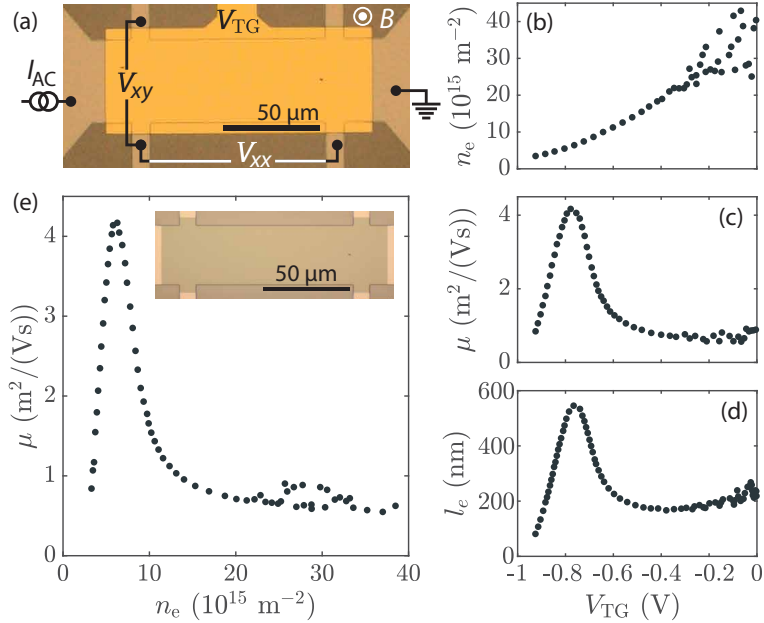


Figure 3.4: **M26 etch-defined Hall bar.** (a) Optical microscopy of the device after gate deposition, also showing measurement parameters. (b-d) Extracted carrier density, mobility and mean free path as a function of top-gate voltage. (e) Parametric plot of carrier mobility versus density. Inset shows optical microscopy of the device before gate deposition.

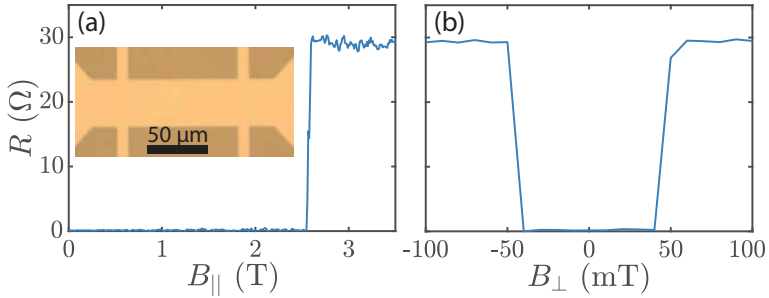


Figure 3.5: **Mz6 AG Al bar.** **(a)** Four-terminal resistance as a function of a in-plane field $B_{||}$. Inset show the bar covered with as-grown Al. **(b)** Four-terminal resistance as a function of a in-plane field B_{\perp} .

S-QPC-N: A quantum point contact (QPC in short) is used for making local constrictions in a 2DEG. It consists of two pointy electrostatic gates facing each other. Through depletion, they form a narrow conducting channel in the 2DEG, which can be pinched off with further depletion. A S-QPC-N device is a QPC being placed at the border of an Al etch, see [figure 3.6\(a\)](#).

Differential conductance tunnel spectroscopy is performed by measuring the current going across the QPC in the tunnel regime from sourcing an AC voltage $V_{AC} \sim 3 \mu\text{V}$ superimposed on a DC source-drain voltage V_{SD} . A map of differential conductance versus QPC voltage V_{qpc} and V_{SD} shows an induced gap before pinch-off, see [figure 3.6\(b\)](#). The magnitude $\Delta^* \sim 185 \mu\text{V}$ is estimated from half the conductance peak spacing and is extracted from a line cut taken at $V_{qpc} = -1.4 \text{ V}$, see [figure 3.6\(c\)](#). When driving the Al resistive with $B_{\perp} = 1 \text{ T}$, three well-defined quantization steps are observed in zero bias conductance, displayed in [figure 3.6\(d\)](#). This testifies the quality of this quantum well. At zero B_{\perp} we see conductance enhancement, but no well-defined $4e^2/h$ plateaus.

1D wire: An elongated wire geometry should be ideal for hosting Majorana end modes, elaborated in [subsection 2.4.5](#). One way to define wires in the 2DEG platform was introduced by ref [109]. A 1D channel is imprinted in the 2DEG by an etch-defined Al wire which screens the

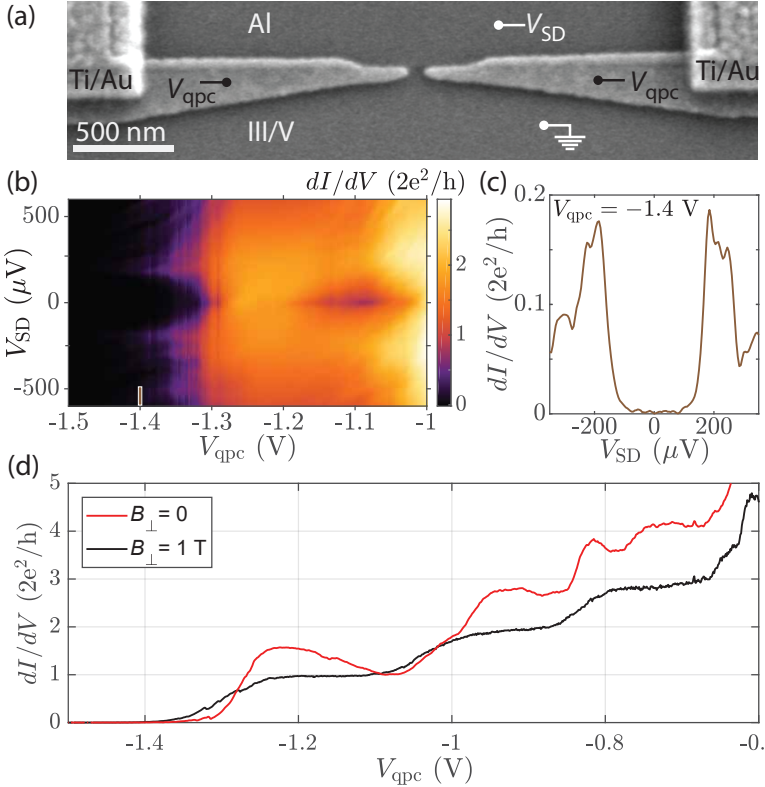


Figure 3.6: **M26 spectroscopy.** (a) Scanning electron microscopy of a superconductor semiconductor junction with a two Ti/Au gates forming a quantum point contact tunnel-constriction. A similar device was used to measure data in (b-d). (b) Differential conductance measured as a function of source drain voltage and quantum point contact voltage. (c) Differential conductance versus source drain voltage. Cut is from $V_{qpc} = 1.4$ V. Induced gap $\Delta^* \sim 185$ μeV is extracted. (d) Zero bias conductance is measured at $B = 0$ and 1 T with the Al being superconducting and resistive, respectively. In the resistive regime, three clear conductance steps are observed.

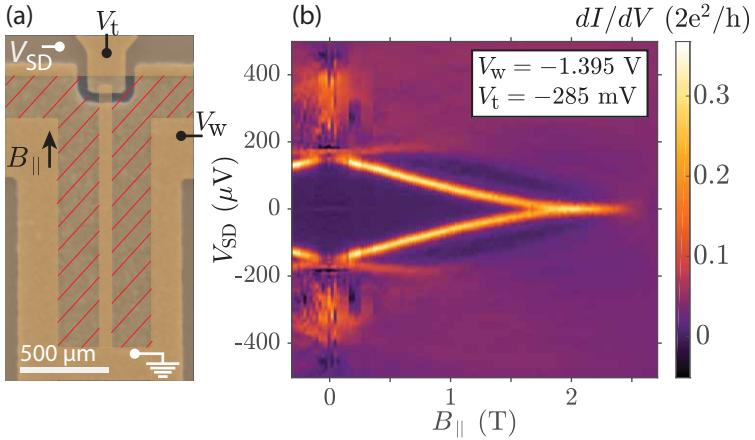


Figure 3.7: **Mz6 wire.** (a) False-colored scanning electron microscopy of an Al wire, grounded in one end and tunnel-connected to an Al plane in the other. V_t controls the tunnel coupling and V_w pinches off exposed III/V (marked by red lines), forming the wire shape in the 2DEG. Differential conductance can be measured while varying the gates, the source drain bias V_{SD} , and a magnetic field $B_{||}$ parallel to the wire. (b) Differential conductance measured as a function of V_{SD} and $B_{||}$, with both V_w and V_t energized. Two sub gap states meet by sweeping $B_{||}$ and sticks at zero energy until $B_{c,||}$.

depletion from a global top-gate. The same gate also tuned tunneling at the wire end. Ref [75] added an additional gate to have independent control of tunneling V_t and wire formation V_w , see figure 3.7(a). Besides forming the wire, V_w is also meant to tune the chemical potential under the Al wire.

By tuning around in V_w - V_t -space, different subgap states are found. One example is shown in figure 3.7(b). At $B_{||} \sim 0$, both the Al wire and the Al plane has an induced gap, forming an S-I-S Josephson junction with a lot of features above $\Delta^* \sim 185 \mu\text{eV}$. Applying $B_{||} \sim 300 \text{ mT}$ softens up the induced gap under the Al plane resulting in a N-I-S junction, which is easier to interpret. Two subgap states start from $eV_{\text{SD}} = \Delta^*$ and are by Zeeman splitting, equation 2.27, driven towards zero energy, where they seem to meet and stick until the gap collapses around $B_{c,||} \sim 2.5 \text{ T}$. The subgap states' g-factor was extracted to be $g^* \sim 3$ from their $B_{||}$ -slope using equation 2.27. It being much smaller than g_{InAs}^* could be due to the strong coupling to Al, as well as contributions from the surrounding heterostructure.

3.2 FABRICATION WITH AL ETCH

The fab recipe developed by M. Kjaergaard and H. Suominen (reported in M. Kjaergaards thesis [110]), has been a solid foundation for general fab of shallow InAs 2DEGs. This section will give a quick overview of the fab steps and elaborate improvements added during this thesis. The recipe in its current state is thoroughly elaborated in Appendix B.

For lithography we use Elionix electron beam lithography systems together with a combination of PMMA and MMA e-beam resists, specified for each step in Appendix B. We have access to a 100 kV and a 125 kV system in QDev. They allow for alignment and lateral resolution down to 10 – 20nm.

Preparing for fab. The material we receive from Michael Manfra's lab are grown on 2" wafers. When we receive a wafer we inspect it using bright and dark field optical microscopy, spin-coat it with PMMA

and store it in a chamber with Nitrogen over-pressure, to preserve the material.

To maximize the amount of experiments being made from one growth, we use small $\sim 3 \times 5 \mu\text{m}^2$ chips. These are made with a high precision scribe. It has a rotational stage so that we can align the scribe lines to the minor and major flats. Chips are cleaved on a cleaving block. The cleaving force is applied with tweezers or by fingers with a cleanroom wipe in between.

This whole process is done with the PMMA on, so that particles from the scribing and cleaving will be stripped with the resist. This first strip is done by sonication in Dioxolane for 5 min at 80 kHz and 100% power, followed by squirts of acetone, then isopropanol and lastly blow-drying with a nitrogen gun. After device fabrication is started, sonication is avoided due to the risk of potential damage to the nano-structures. Now the chip is ready for nano-lithography. [Figure 3.8](#) illustrates the different steps.

Alignment marks. To align consecutive lithography exposures, alignment marks are needed. There are two ways for making these. The first is done with evaporation and liftoff. It enables auto-detection of the alignment marks in our Elionix E-beam systems. Evaporation of 10/50 nm Ti/Au is enough to get a good color-contrast with the scanning electron microscope. The second way of making the marks is to etch them out together with the mesa etch.

Mesa Etch. Since our material is conductive per default, we need to etch away the conducting layers to have isolated device with controlled current paths. If alignment marks are made in the mesa etch step, they should be exposed first to minimize stage drift during the E-beam exposure. The etch is done in two steps. First the surface Al is etched (elaborated below). Second, the III/V is etched in a $\text{H}_2\text{O} : \text{C}_6\text{H}_8\text{O}_7 : \text{H}_3\text{PO}_4 : \text{H}_2\text{O}_2$ (220:55:3:3 ratio) solution. Depending on the heterostructure, different etch depths are needed for mesa insulation. For M26, 300 nm was needed, which was achieved in ~ 9.30 min at room temperature. After the etch, the resist was stripped and the etch depth was verified with a profilometer.

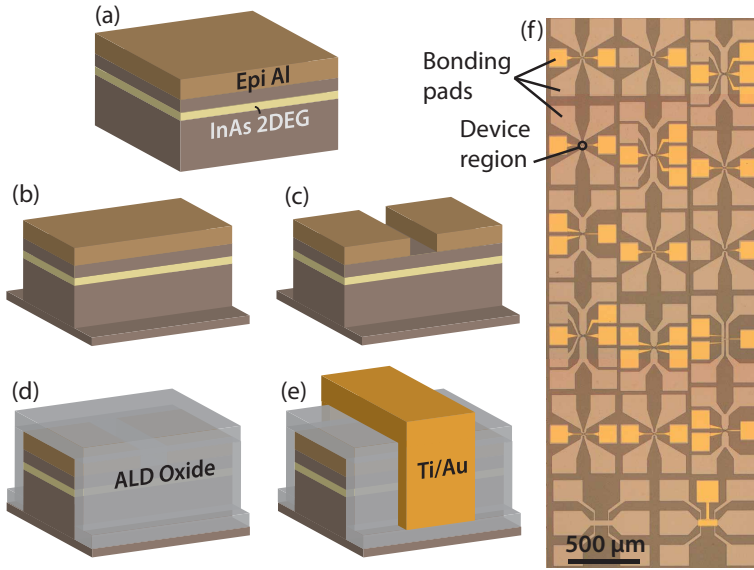


Figure 3.8: **Fabrication steps.** These schematics, which are not to scale, specifically illustrate the creation of a Josephson junction, but most other devices have the same fab steps. **(a)** Starting with a clean hybrid material with Al grown *in situ* on a shallow InAs 2DEG. **(b)** A mesa etch defines the region of conduction. **(c)** An Al etch defines the gateable regions with Al. **(d)** A global dielectric is grown with atomic layer deposition **(e)** Ti/Au is evaporated for electrostatic gating. **(f)** Optical microscopy of a finished chip.

Al Etch. As mentioned in [subsection 3.1.1](#) the Al etch can degrade the 2DEG transport properties. We shall see below that this crucial step is hard to execute consistently. The recipe was developed to enhance the resolution of the etch and is (in the time of writing) the only etch recipe that is proven to make usable devices.

After exposure and development, the etch is prepared. We have been using Transene etch D⁸, heated to 50 ± 0.5 °C. Two beakers fo Transene D are put in a hot bath. One for the etch and one for temperature measurements. Two beakers with Milli-Q water should be prepared as well. One at 50 °C the other at room temperature. An etch of 5.5 sec is followed by 20 sec in hot Milli-Q and finally 40 sec in room temperature Milli-Q. The short etch time is not ideal for reproducibility and the time may vary from user to user, depending on when exactly the time is started and stopped.

Significant improvement to the lateral resolution was achieved by post-baking the resist after development, see [figure 3.9](#). The following test was done: Two chips from the same growth had a grid of small holes patterned using the same resist and exposure recipe. The first chip was chemically developed and etched, see [figure 3.9\(a-b\)](#). A lateral etch run of ~ 20 nm was observed. The second chip was chemically developed but also had a short oxygen plasma ash for 45 sec, followed by a post bake for 2 min at 115 °C. The ash is used to get rid of thin organic residues on the surface while the baking is believed to reflow the resist, illustrated [figure 3.9\(c\)](#). Subfigure (d) shows the etch result, with a minimal etch run of $\sim 2-4$ nm. This optimized development process has since been implemented for all our wet chemistry.

After Al etch, the III/V surface is exposed and susceptible to damage, so efficiency is key. A thorough strip is executed before loading the chip into an atomic layer deposition (ALD) system.

ALD. Two different dielectrics, alumina and hafnia, have been used for shallow 2DEGs over the years. With a limited amount of testing, a slow and low temperature (90 ± 0.5 °C) hafnia recipe, with a 10 hour pre-bake at base pressure, was found to give the least amount of hysteresis and

8 <https://transene.com/aluminum/>

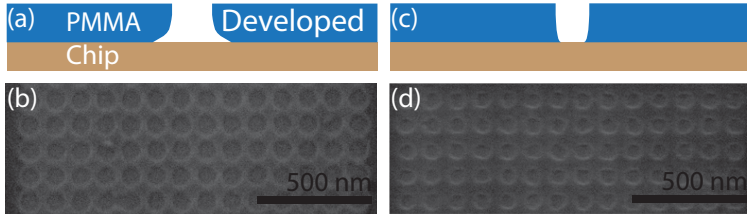


Figure 3.9: **Reflowing resist before wet etch.** (a) Illustration of the expected resist profile after chemical development. (b) Scanning electron microscopy of etched holes in Al. (c) Illustration of the expected resist profile after chemical development, followed by plasma ash and thermal reflow of the resist. (d) Scanning electron microscopy of etched holes in Al using the reflowed resist. The holes are smaller than in (b) and only a few nm larger than designed.

charge switches. We expect the pre-bake to remove solvents and organics from the surface.

Gate evaporation. Finally, Ti/Au gates are evaporated. If small features like in [figure 3.6\(a\)](#) or [3.7\(a\)](#) are needed, two lithography steps are necessary. First, the small features are enabled by a single layer resist and a 3/20 nm Ti/Au evaporation. To have gates crawling up the 300 nm mesa walls, see [figure 3.8\(e\)](#), 10/350 nm Ti/Au is evaporated on a patterned resist with a deep undercut.

Bonding. A reader with a background in semiconductor devices might ask her-/himself: what about ohmic contacts⁹? A practical advantage of the Al covered shallow 2DEGs is that a high yield ohmic contact is obtained by bonding straight to the mesa with an Al threaded wedge bonder. Squares of dimensions 100 – 200 μm are suitable for the purpose, see [figure 3.8\(f\)](#). To prepare for bonding, the chip is glued onto a daughter board with PMMA. The board is chosen according to the motherboard being used at the measurement setup. Currently, most setups are equipped with 96 DC lines, allowing for many devices to be cooled down simultaneously.

⁹ Low resistance electrical contact to a device for source and drain.

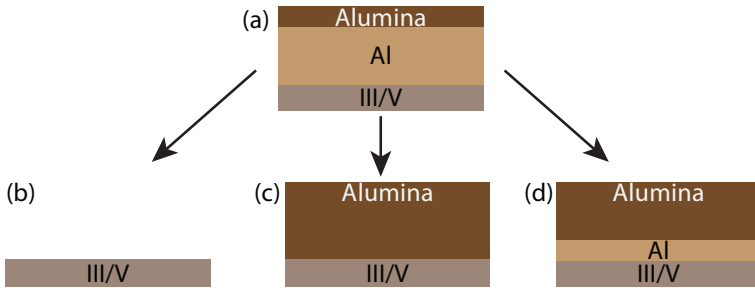


Figure 3.10: **Different aluminum processes.** (a) Untouched heterostructure. (b) Al etch. (c) Full oxidation. (d) Partial oxidation.

The chip is now ready for being loaded and measured in a cryostat. The measurement setups will be briefly covered in [section 3.4](#).

3.3 INTRODUCING ANODIC OXIDATION

3.3.1 *Motivation*

To make junctions and enable electrostatic gating of the 2DEG, metallic aluminum has to be removed. With its good lateral resolution, hot Transene D etches have enabled a lot of publications [11, 27, 61, 75, 78, 79, 89, 102, 104, 107–109, 111–115]. Still, this aluminum etch is not ideal. It exposes the surface III/V, allowing it to oxidize, causing carrier scattering [103]. The etch causes additional scattering itself as shown in [figure 3.2](#), possibly due to chemical damage.

Rather than stripping the grown aluminum/alumina as in [figure 3.10\(b\)](#), the metallic phase can be removed through complete oxidation, turning the whole film into alumina, [figure 3.10\(c\)](#). It won't turn superconducting and it doesn't screen electric fields. If done properly, this process would avoid the chemical damage from etching and simultaneously passivate the III/V surface, thus significantly reducing surface scattering.

Another benefit of oxidation, is the possibility of partial oxidation of aluminum, see [figure 3.10\(d\)](#), leaving behind a thinner metallic film than what is possible with growth, see [subsection 3.1.1](#). *Very thin films*

are expected to have significantly increased superconducting parameter space, see [subsection 2.3.7](#).

For this thesis, we implemented electrochemical anodic oxidation (AO), but other options are also available as discussed in [section 8.4](#). Electrochemical AO is a well established process for oxidizing metals; particularly Al. The process has been used in the industry for approximately a century [116] to surface coat various metallic components.

Depending on the choice of chemical, two different types of coating are possible[117]. One is a thick porous-type film with long (up to multiple microns) pores extending through the oxidized region. In this study we aimed for a barrier-type film, a thin and uniform oxide layer, which has previously been used as a low loss dielectric [118].

3.3.2 *Chemical reaction and experimental setup*

The chemical reaction of AO is displayed in [figure 3.11\(a\)](#): A voltage V_{AO} is sourced between Al and an electrolyte in which Al is emerged. The voltage stimulates oxide growth by driving oxygen ions to the Al surface. The barrier type oxidation depth increases linearly with applied voltage. Refs [119, 120] observed a barrier-type oxidation with a depth-voltage dependence of 1.3 nm/V when using tartaric acid (3 percentage by mass), pH regulated to pH of ~ 5.5 by ammonium hydroxide. We implement a similar solution in our studies. The mixture recipe is elaborated in [Appendix B](#).

Our electrical setup is displayed in [figure 3.11\(b\)](#). Electrical contact to our small delicate chips was established through small aluminum bonds. To stabilize the setup a glass slide was prepared with Ti/Au evaporated in one end¹⁰ (top). The chips (potentially with a ready mask) would be glued, with PMMA, to the bottom end of the glass slide and long aluminum wires were bonded from chip to the Ti/Au. An alligator can then contact the Ti/Au, making connection to a voltage source. The glass slide with a chip bonded to Ti/Au was put into the ammonium tartrate

¹⁰ The masking was done by covering the rest of the slide with aluminum foil

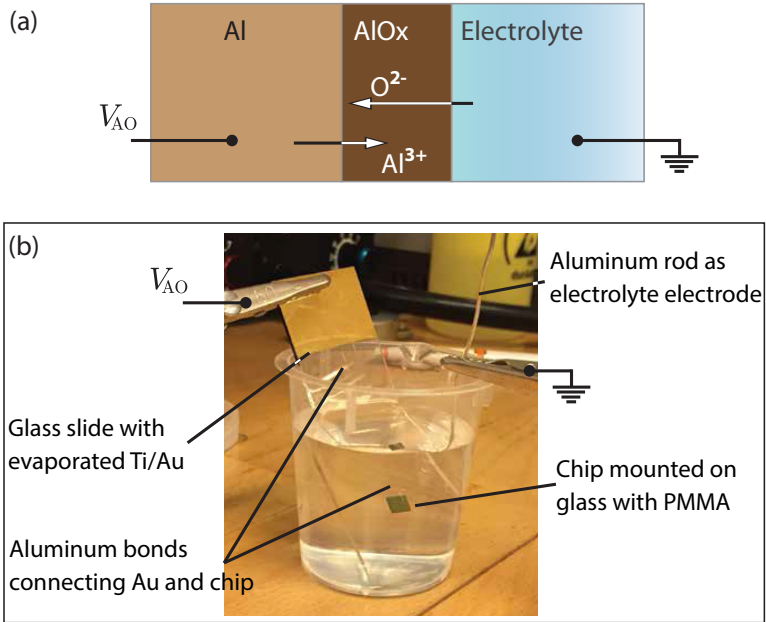


Figure 3.11: **Chemical reaction of anodic oxidation.** (a) Anodic oxidation process uses a source voltage V_{AO} between the metal (Al) and the electrolyte to drive O^{2-} ions on the Al surface. (b) Electrical setup used for executing anodic oxidation. The chip was mounted (with PMMA) on a glass slide that have Ti/Au evaporated on the other end. Aluminum bonds are shorting the Ti/Au and chip. Glass slide and an aluminum rod are put in the electrolyte and are both contacted with alligators to source a potential difference V_{AO} .

solution together with an aluminum rod, grounded by another alligator clip.

With the glass slide and rod submerged, the power supply was turned on and ramped with 100 mV/s to the desired voltage, V_{AO} . Once reached, the process ran for 5 minutes before the voltage was ramped down, again with 100 mV/s. Once at zero, alligators were unhooked and the glass slide was rinsed in MQ. The chip was then stripped from the glass using acetone and isopropanol. This step replaces the Al etch step in the original recipe mentioned in [section 3.2](#).

As we shall see in [chapter 6](#), E-beam resist is not sufficient to obtain nm-resolution lithography with AO, but for μm sized features, resist suffice. A rather thick resist was needed, otherwise the AO process had a high risk of attacking through the resist.

3.3.3 *Adjustments to AO setup*

Due to the observation of inconsistencies in oxidation depth among areas with similar AO exposures, thoughts were put into optimizing the reproducibility. Here is a list of healthy practices to maximize the outcome and reproducibility when using this setup for anodic oxidation. Many of these points were thought of after finishing experiments, but should be implemented in the future.

Do not have exposed regions with Au on the surface. Au has an unwanted reaction with the AO process, leaving behind residues in large areas around the exposed Au. Alignment marks should therefore not be capped with Au as the final material.

AO before mesa etch.

When fabbing a chip using Al etch, there are two main reasons to begin with the mesa etch. One is that alignment marks can be made with the mesa, thus removing a lithography step. Another is to expose the surface III/V as little as possible in between Al etch and ALD.

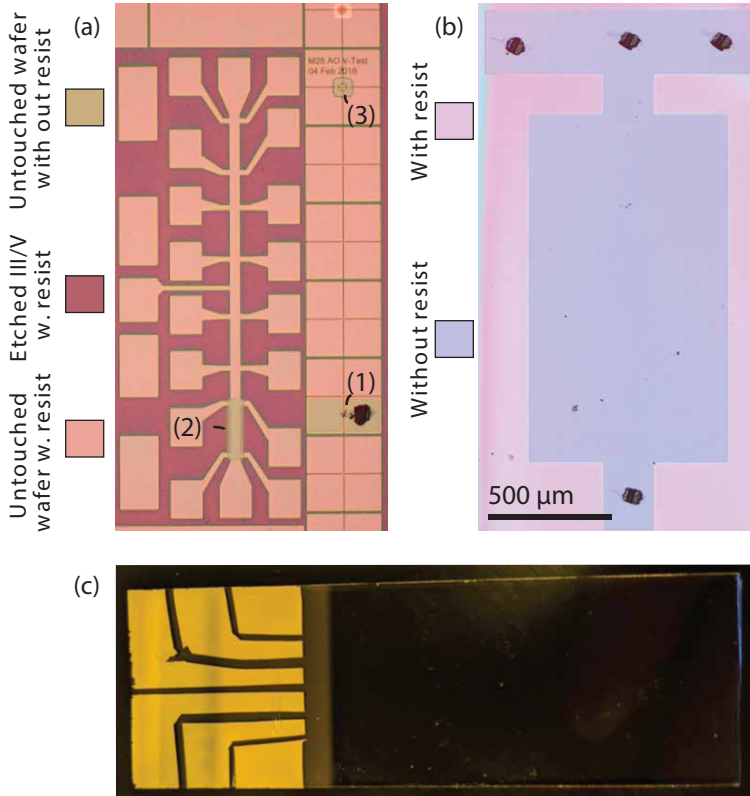


Figure 3.12: **Bond placement for anodic oxidation.** (a) Initially, AO was done after mesa etch. (1) A region on the side of the chip was exposed and bonded to. (2) The exposed device area was separated from the bond by etched mesa. (3) Alignment mark areas are also exposed to AO. (b) AO done as first step. All exposed regions are shorted to the bonds with Al. It is more fail-proof to use multiple bonds, and if not shorted, multiple bonds can be used to do resistance measurements. Scale bar applies for both images, which were captured with optical microscope. (c) Picture of glass slide with multiple Ti/Au leads. Masking was done with aluminum foil.

When implementing AO, multiple points advocate doing AO before mesa etch.

- The mesa side walls are exposed to AO if it is done after mesa etch. The specific implications of this are not known, but oxidizing the III/V is bad for transport.
- The potential of the aluminum to be anodized should be as close as possible to the applied potential V_{AO} . The resistance between the bond and the exposed area should therefore be as little and consistent as possible. By doing mesa etch first, the isolated devices will be spaced by etched portions, see [figure 3.12\(a\)](#). These regions are conductive at room temperature, but has higher resistance than aluminum. If instead AO is done before mesa etch, see [figure 3.12\(b\)](#), then everything is shorted by Al, giving a more consistent potential to the exposed regions each time.

Hot transene did not yield good results in etching anodized Al. Instead, 5 min in MF 321 (an optical resist developer) stripped the anodized Al without residues being left behind. This etch was only used for large features, so the 5 min etch time is not optimized for good resolution.

Setup logistics

To ensure a reproducible voltage drop gradient across the solution and alumina, the following steps should be considered.

- Place the glass slide and the Al rod vertically in the solution, and place them as far apart in the beaker as possible. This will ensure a reproducible spacing between the two and therefore a reproducible voltage drop. Even better, a more advanced setup could be machined, with fixed chip and rod distance.
- If a bond from Ti/Au to the chip traverses the exposed region to be anodized, it could screen the sourced voltage potential between that region and the rod. When mounting the chip on the glass slide, orient the chip such that bonds will not cross exposed regions of interest. This is illustrated in [figure 3.13](#).

Resistance measurements

With a multi-leaded glass slide, such as the one in [figure 3.12\(c\)](#), 2-

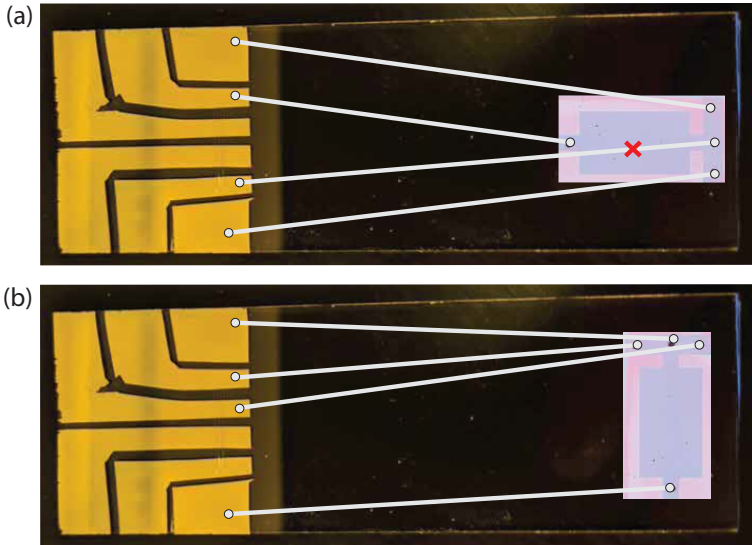


Figure 3.13: **Chip orientation for bonding.** Schematic showing poor and good practices for chip mounting and bonding before AO. **(a)** Poor choice of chip orientation forces one bond, marked by a red cross, to traverse the region to be anodized. **(b)** Proper choice of chip orientation allows all bonds to avoid the region to be anodized.

terminal resistance between different bonds could be tested. Especially the resistance before and after AO gives an idea of how deep a given oxidation has gone. It is preferable to verify consistency in fab early in the fab process, rather than finding out later when measuring the finished devices. When comparing resistances of two different AO exposures, the same geometry and bond placement should be used. Here, the pattern in [figure 3.12\(b\)](#) was useful. Middle top and bottom bonds were used for V_{AO} , while the left/right top bonds were used for resistance measurements, either between each other or to the middle bond.

3.4 MEASUREMENT SETUP

Many quantum phenomena are only observable at very low temperatures. The state of the art commercial cooling technique is $^3\text{He}/^4\text{He}$ dilution refrigeration [31]. Dilution fridges, both from Oxford and Bluefors, with base-temperatures in the range $\sim 20 - 40$ mK were used. All the DC (low frequency) lines, accessed through a break out box, were equipped with rf and rc filters from QDevil¹¹. All fridges were equipped with a 6-1-1 tesla vector magnet for optimal magnetic field control.

All data from AO-based devices were acquired in current-bias configuration, measuring a 4-terminal voltage drop with standard lock-in techniques, using frequencies in the range $10 - 170$ Hz. Both SR830 and the newer SR860 were used. AC excitation of $1 - 20$ nA was sourced through $100\text{ M}\Omega$ or $1\text{ G}\Omega$ resistors in parallel with a variable DC current sourced through $100\text{ k}\Omega$. Current was read out through a Basel IV-converter, usually with a gain of 10^5 . A 4-terminal voltage drop was measured through a 10^3 voltage amplifier with an input impedance of $500\text{ M}\Omega$. DC voltage bias for gates was sourced through a low-pass filter with a cutoff frequency of ~ 16 Hz.

To perform voltage-bias used for high resistance devices (spectroscopy and quantum dots), the bias resistors for AC and DC was exchanged with 10^5 and 10^3 voltage-dividers, respectively, and the current to voltage converter gain was increased to 10^8 .

¹¹ <https://www.qdevil.com/qfilter/>

ANODIC OXIDATION OF Al ON INSULATING GaAs

In [subsection 3.3.2](#) we addressed how to thin down metallic aluminum by using anodic oxidation (AO). From [subsection 2.3.7](#) we expect the thinned Al to have increased superconducting critical temperature and enhanced critical magnetic field. To investigate the properties of epitaxial Al thinned by (AO), a separate study was done where epitaxial Al grown on an insulating GaAs substrate, see [figure 4.1\(a\)](#). First, [section 4.1](#) elaborates material, fab and devices. [Section 4.2](#) presents a transmission electron microscopy study of the anodized Al showing a rough morphology while [section 4.3](#) presents transport studies showing enhanced critical temperature and field of anodized aluminum. Concluding remarks are given in [section 4.4](#).

These results are also presented in [\[121\]](#)

4.1 MATERIAL AND DEVICES

Using an insulating substrate makes it straight forward to extract transport properties of the oxidized Al due to not having other conductors in parallel. GaAs was chosen due to its compatibility with epitaxial growth of Al [\[122\]](#).

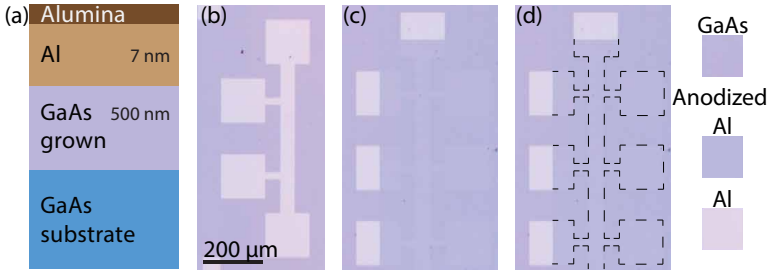


Figure 4.1: **Al on GaAs material and devices.** (a) The simple stack of Al grown on GaAs. (b-d) Optical micrographs showing devices measured on GaAs substrate, sharing the same scale bar. (b) Bar etched out of as-grown aluminum, named AG_{GaAs} . (c) AO bar etched out in anodized region. Oxidized aluminum is hard to distinguish from substrate, so some Al was left unprocessed on bonding pads to enable localization of the pads. (d) Identical to (c), but with dashed lines indicating boundary of bar and substrate.

Four different anodic oxidation voltages were tried in separate lithography steps, out of which only the lowest $V_{\text{AO}} = 4 \text{ V}$ was conductive. The AO was done in resist defined patterns as shown in figure 3.12(b). Consecutively an EBL defined chemical wet etch (MF-321 developer for 5 min at room temperature) was done to define elongated Hall bars in the anodized and as-grown Al, see figure 4.1(b-d).

In total three bars were measured: A bar etched out of as-grown Al (AG_{GaAs}) and two bars etched out of the anodized region (AO_{I} and AO_{II}).

4.2 MORPHOLOGY OF ANODIZED Al

A transmission electron microscopy (TEM) study of the anodized aluminum was done, to extract the morphology of the anodized Al film [121] It was conducted by Dr. Rosa Diaz from Purdue University. This section will summarize the main points of the study.

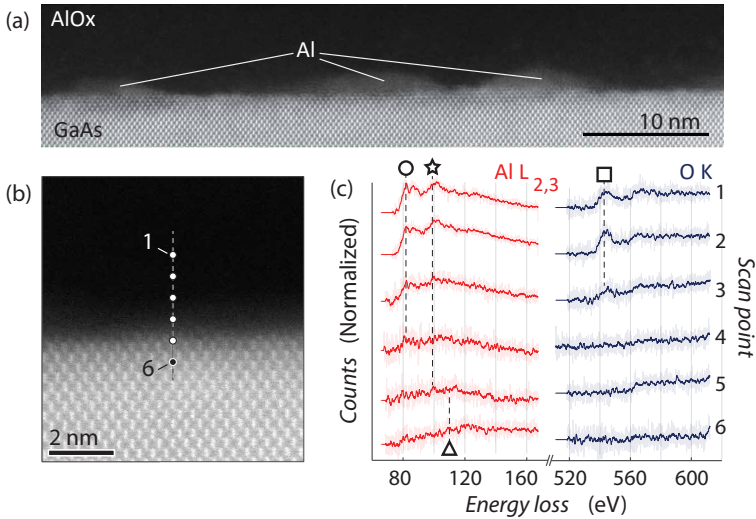


Figure 4.2: TEM study of anodized Al. (a) Scanning transmission electron micrograph in high-angle annular dark-field (HAADF) mode of AlO_x , showing up to 2 nm hills of Al at the GaAs interface. (b): HAADF image of the Al/GaAs interface. Electron energy loss spectroscopy (EELS) was performed at 6 different locations (marked by points and separated by 0.3 nm) along the growth direction to gauge material composition. (c) EELS image showing L edge for Al spectra (Red) and K edge for O (Blue) from scan points 1–6, in (b) with 0.3 nm separation. Symbols indicate composition: (o) AlO_x , (☆) Al or AlO_x , (△) GaAs, (□) oxygen.

Figure 4.2(a) displays a scanning tunneling electron microscopy (STEM) micrograph acquired in high-angle annular dark-field (HAADF) mode of AlO_1 at the GaAs/Al interface. Three hills of metallic Al (dark grey) are distinguishable from GaAs (bright) and AlO_x (black). Hills of Al, ~ 2 nm in height, were observed across the entire cross section sample. The origin of irregular Al thickness resulting in the hills is not clear. One possible explanation could be that amorphous grain boundaries in the Al, formed during heterostructure growth, could oxidize faster/deeper than the crystalline grains. The different oxidation of amorphous and crystalline aluminum was observed when oxidizing Al with nitric acid [123]. Another explanation could be degradation of the lamella happening during FIB preparation.

Electron energy loss spectroscopy (EELS) was implemented to analyze the elemental configuration, as was done in [124]. Specifically it was studied whether the region between Al hills was covered with metallic Al or only alumina. High resolution STEM micrographs in HAADF mode were acquired at the Al/GaAs interface between Al hills, one is displayed in figure 4.2(b). EELS analysis was done at points on a line along the growth direction, see figure 4.2(b,c). For each point, inelastically scattered electrons are measured and binned according to their energies, giving information about the atoms causing the scattering. Energy loss is defined as the difference between the measured energy and the initial kinetic energy. Dual EELS mode was used. It allowed for simultaneous acquisition of Al L-edge (~ 80 eV) and O K-edge (~ 540 eV) energies. All EELS data was background subtracted, normalized and averaged every 20 points.

When GaAs is scattering the electrons, a shoulder around an energy loss of 110 eV (marked by Δ in figure 4.2(c)) is expected. Metallic aluminum has one peak around 97 eV (\star) while alumina has two peaks around 79 eV (\circ) and 98 eV (\star). The presence of oxygen can also be measured at high energy EELS where it creates a peak around 540 eV (\square).

At the Al L-edge, presence of GaAs (Δ) is indicated at points 6 and maybe 5; alumina (\circ) are at points 1 to 3, maybe 4; metallic Al (\star , no \circ) indications are at 4 and 5. Looking the O K-edge, high energy, oxygen

(\square) is only present in points 1 thru 3, suggesting that point 4 indeed has metallic Al.

To get quantitative data on the global morphology of the Al after AO, nine additional EELS analyses were conducted in between other Al hills. Only one out of the total ten EELS analyses didn't show any presence of metallic Al, suggesting $\sim 10\%$ of regions in between hills are fully oxidized. A collection of broad view STEM like [figure 4.2\(a\)](#), were used to extract the ratio of hills/land in the lateral direction. We find that the hills have an average height of 2 nm and cover $\sim 33\%$ of the imaged regions. Within the remaining $\sim 67\%$, $\sim 10\%$ is fully oxidized. The remaining $\sim 60\%$ contains a thin metallic Al layer. Measurements of the metallic Al thickness, in the between hills, span 3 to 6 Å (5 Å on average), similar to 1 – 2 ML of Al. Additional scans and analyses are included in Supplementary Material of ref [121]. In summary, an uneven, though continuous, Al film is formed by AO.

4.3 TRANSPORT STUDY

With AO changing the thickness and morphology of the Al films, a change in superconducting properties can be expected, as mentioned in [subsection 2.3.7](#). Resistance of the three bars, AG_{GaAs} , AO_I , and AO_{II} was measured as a function of temperature (T) and in-plane magnetic field $B_{||}$ or perpendicular field B_{\perp} .

The study of critical in-plane field ($B_{c,||}$) as a function of temperature is displayed on [figure 4.3\(a\)](#). The GaAs substrate freezes out at these temperatures, restricting all transport to the Al. 4-terminal longitudinal resistivities, ρ_{xx} , were measured on three different devices. The similarity of AO_I and AO_{II} in [figure 4.3](#) indicates that the two AO bars came out close to identical, suggesting a uniform AO process in the exposed area. In the following, only AO_I will be addressed.

$B_{c,||}(T)$ is extracted from ρ_{xx} versus $B_{||}$ at fixed temperature. Examples of such field scans are shown in the two insets of [figure 4.3\(a\)](#). Additional scans are displayed in the appendix [section C.1](#). For AG_{GaAs} , the normal state resistivity is low $\rho_{N,AG} = 3.5 \Omega/\square$ and the transition is sharp,

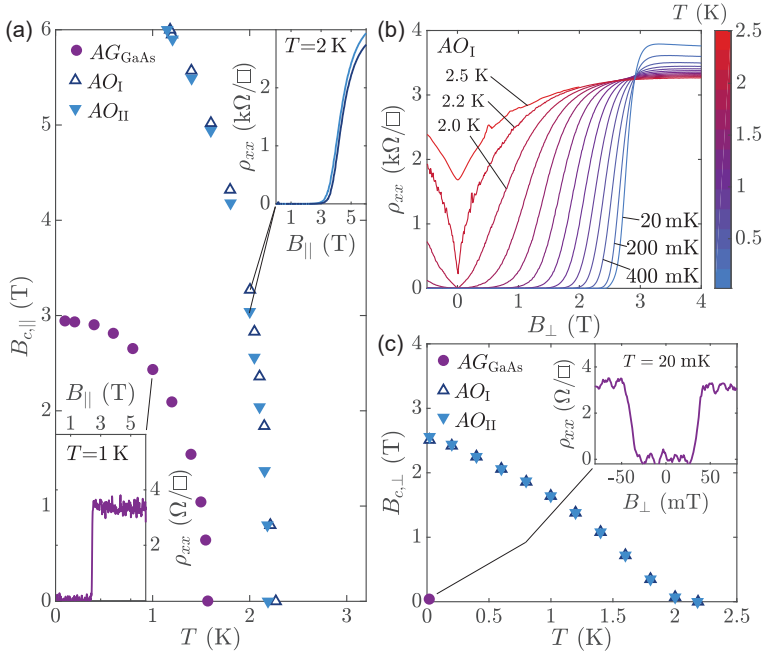


Figure 4.3: **Transport data from GaAs material.** (a) Critical in-plane field of AG_{GaAs} and AO bars as a function of temperature. Insets: examples of ρ_{xx} versus B_{\parallel} at elevated temperatures of 1 K and 2 K respectively, used for extracting $B_{c,\parallel}$ points marked by lines. (b) AO_I ρ_{xx} versus B_{\perp} at different temperatures. (c) Same as (a) but for B_{\perp} , extracted from data in (b) with $\rho_{xx}(B_{c,\perp}) = 0.01 \cdot \rho_N$. Inset: ρ_{xx} versus B_{\perp} at base temperature for AG_{GaAs} .

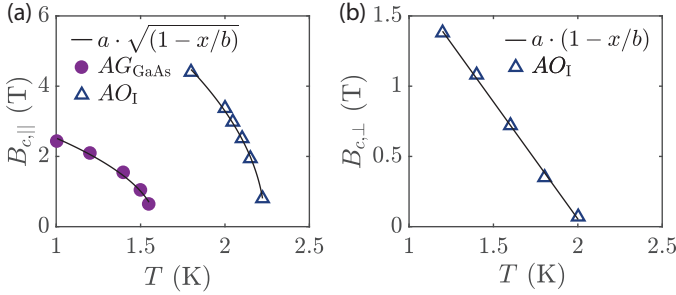


Figure 4.4: **Temperature dependence of critical fields.** Temperature dependence of critical fields for $T \lesssim T_c$ are compared with expectation from GL theory, equation 2.55. (a) parallel critical field $B_{c,||}$, and (b) perpendicular critical field $B_{c,\perp}$.

while the AO bars have higher resistivities $\rho_{N,AO} \sim 3.5 \text{ k}\Omega/\square$ and broad transitions. $B_{c,||}$ will be defined as $\rho_{xx}(B_{c,||}) = 0.01 \cdot \rho_N$.

To explain the three orders of magnitude difference between ρ_N of the AG_{GaAs} and AO bars, resistivity contributions affecting thin films needs to be taken into account. Possible contributions originate from roughness as well as scattering from grain boundaries and surfaces [125].

The 7 nm Al has $B_{c,||} = 2.97 \text{ T}$, reported in figure 4.3(a), while the few ML thin AO films have a $B_{c,||}$ higher than the 6 T limit of our vector magnets. A slow temperature scan was performed with $B_{||} = 6 \text{ T}$ to extract $T_c(B_{||} = 6 \text{ T}) = 1.18 \text{ K}$ for AO_I . Temperature sweeps were also used to extract $T_c(B_{||} = 0)$. AG_{GaAs} has $T_c = 1.57 \text{ K}$ while AO_I has $T_c = 2.27 \text{ K}$. As expected from subsection 2.3.7, the thin and disordered Al film has a higher T_c .

For a BSC-like superconductor with $T_c = 2.3 \text{ K}$, the theoretical Chandrasekhar-Clogston (CC) limit, see subsection 2.3.7, for the highest possible critical field, assuming a metallic Lande g-factor of 2, is $B_c(T = 0) \sim 4.6 \text{ T}$, which this data clearly violates. A suppression of Zeeman energy could originate from the high surface to bulk ratio of the anodized films adding a significant Rashba term to the Hamiltonian of conduction electrons [126].

Critical perpendicular field as a function of temperature $B_{c,\perp}(T)$ was studied as well, reported in [figure 4.3\(b-c\)](#). $B_{c,\perp}$ will be defined as $\rho_{xx}(B_{c,\perp}) = 0.01 \cdot \rho_N$. A 20 mK scan was performed for the AG_{GaAs} bar, showing a critical perpendicular field $B_{c,\perp} = 32$ mT, slightly higher than the bulk aluminum value $B_c = 10.5$ mT, see [figure A.1](#). Scans used for $B_{c,\perp}(T)$ extraction of AO_{I} are shown in [figure 4.3\(b\)](#), while [figure 4.3\(c\)](#) displays extracted values for AO_{I} and AO_{II} . AO_{II} scans are displayed in [appendix section C.1](#). An almost two orders of magnitude increase in $B_{c,\perp}$ up to ~ 2.5 T is observed for the anodized bars, comparable with high $B_{c,\perp}$ extrapolated from measurements on granular aluminum [[42](#), [127](#)].

Just below 3 T, a crossover point for different isotherms is observed. Such crossovers indicate superconductor-insulator transitions, mentioned in [subsection 2.3.7](#). A similar crossing was not observed in the probed range of $B_{\parallel}(T)$, but it might occur beyond 6 T. The resistance jumps seen below 1 T at high temperatures are coherent with temperature fluctuations, which was monitored simultaneously.

Comparing $B_{c,\parallel}(T)$ and $B_{c,\perp}(T)$, the latter has a more linear T -dependence for $T \lesssim T_c$. This is expected from Ginzburg-Landau (GL) theory, see [equation 2.55](#), and previously observed in thin quench-condensed Al films [[128](#)]. The expected temperature dependencies are verified with fitting as shown in [figure 4.4](#). The extraction of the film thickness (d) using critical fields ratio, [equation 2.56](#), overestimates with $d \gtrsim 5$ nm. The overshoot is correlated with the high $B_{c,\perp}$, which we attribute to the significant amount of monolayer thin metallic Al across the film.

Another feature worth highlighting is the upward curvature of $B_{c,\perp}(T)$ for $T \lesssim T_c$, previously observed in thin granular aluminum [[129](#)]. There, the authors attributed the effect to electron localization and electron-electron interaction.

4.4 CONCLUSION

This chapter introduced epitaxial Al grown on an insulating GaAs substrate. A film, partially oxidized with AO, was studied with TEM and EELS, showing ~ 2 nm Al hills connected by 1-2 monolayers metallic aluminum. Resistance of bars etched out of as-grown (AG_{GaAs}) and anodized (AO) aluminum was measured as a function of magnetic fields B_{\parallel} and B_{\perp} at various temperatures. The high normal resistivity $\rho_{N,AO} \sim 3.5 \text{ k}\Omega/\square$ of the anodized film indicates a disordered aluminum film. As expected, it had enhanced critical fields $B_{c,\parallel}(1.18 \text{ K}) = 6 \text{ T}$, $B_{c,\parallel}(0) = 2.5 \text{ T}$ and increased critical temperature $T_c = 2.27 \text{ K}$.

With the high resistivity, the partially oxidized aluminum could be interesting for the resonator community as has been the case for granular aluminum [130].

In [chapter 4](#), we showed that partial oxidation of Al, grown on insulating GaAs, significantly increases its critical field and temperature. In this chapter we study anodic oxidation of Al grown on a heterostructure hosting an InAs 2DEG, specifically M26, shown in [figure 3.3](#). [Section 5.1](#) displays the measured devices, oxidized at different voltages V_{AO} . Results from the superconducting devices are presented in [section 5.2](#), while the transport properties of the resistive ones are elaborated in [section 5.3](#). Concluding remarks are given in [section 5.4](#). These results are also presented in [\[121\]](#).

5.1 DEVICES

The two main aims for implementing anodic oxidation on the hybrid Al-InAs 2DEG structures are:

1. Increasing critical temperature T_c and critical magnetic field B_c of Al by partial oxidation, expanding the parameter space in which Majorana modes could reside at zero energy, see [subsection 2.4.5](#). Especially an increased B_c/T_c ratio is beneficial.

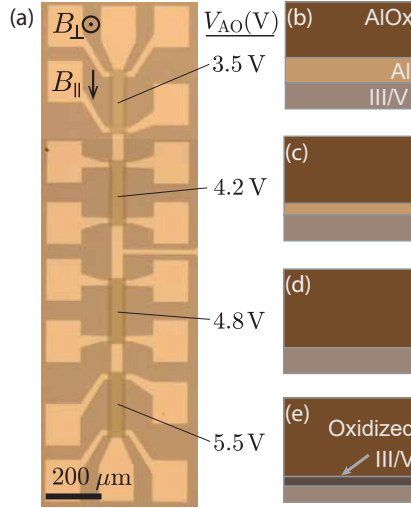


Figure 5.1: **Al on InAs 2DEG devices.** (a) Optical micrograph of an elongated Al/InAs Hall bar (device β) characterized by four different active regions, each of them oxidized and labeled with a different V_{AO} value. (b-e) Expected results of the anodic oxidation process for V_{AO} between 3.5 V and 5.5 V. Increasing V_{AO} increases oxidation depth, effectively thinning down the remaining metallic Al until only alumina is left, depicted in (d). Further increasing V_{AO} oxidizes the underlying III/V, indicated in (e).

2. A complete oxidation of Al should passivate the 2DEG, decreasing the surface scattering that is associated with it being shallow. Reduced scattering would enable stable quantum Hall states at lower fields. Combined with an increased perpendicular critical field of the Al, proximitized quantum Hall states might be realizable.

To accomplish these the right anodic oxidation voltages V_{AO} have to be used. The higher the voltage, the deeper the oxidation, see [subsection 3.3.2](#). Initial tests indicated that full oxidation would happen within a voltage range $V_{\text{AO}} \sim 4 - 6$ V.

Two elongated Hall bars were fabricated simultaneously on the same chip. We'll call them device α and device β . Device β is displayed

in [figure 5.1\(a\)](#). After a mesa etch, AO was performed at four different voltages in four sequential lithography steps. The voltages $V_{AO} = [3.5, 4.2, 4.8, 5.5]$ V, were applied to oxidize different segments of the two devices confined by electron beam lithography. The exposed areas each constitute a Hall bar with four side leads (two on each side), allowing measurement of longitudinal and Hall resistivities, ρ_{xx} and ρ_{xy} . After the anodic oxidations, dielectric was grown and Ti/Au was deposited for top gating.

When the devices were cooled in a dilution refrigerator with base temperature of 20 mK, the devices exposed to 3.5 and 4.2 V were superconducting, suggesting metallic aluminum being left behind, indicated in [figure 5.1\(b,c\)](#). The 4.8 and 5.5 V exposed Hall bars on the other hand showed finite resistance and were gateable, suggesting a full oxidation of aluminum, [figure 5.1\(d\)](#), and potentially oxidation into the underlying III/V semiconductor [figure 5.1\(e\)](#).

5.2 ENHANCED CRITICAL FIELDS OF THINNED Al ON InAs 2DEG

Transport measurements of superconducting anodized Al on a InAs 2DEG heterostructure show similar trends in field and temperature as the anodized Al on insulating GaAs, with the addition of transport signatures from the 2DEG at $B_{\perp} > B_{c,\perp}$.

[Figure 5.2\(a\)](#) shows $B_{c,\parallel}(T)$ (defined as $\rho_{xx}(B_{c,\perp}) = 0.01\rho_N$) for the superconductive bars: Hall bars on device α and β with $V_{AO} = 3.5$ V and 4.2 V as well as the bar with as grown epitaxial Al (AG), displayed in [figure 3.5](#). The data is extracted from $\rho_{xx}(B_{\parallel})$ scans at fixed temperatures. Lower-left inset displays $\rho_{xx}(B_{\parallel})$ from AG and 3.5 V Hall bars measured at 20 mK, showing a sharp superconducting transition. Top-right inset presents 4.2 V measurements of $\rho_{xx}(B_{\parallel})$ at 1.8 K, showing a smooth superconducting transitions. The full set of measurements is included in the appendix [section C.2](#).

AG has a normal state resistivity $\rho_{N,AG} = 6\Omega/\square$. On both device α and β , the aluminum anodized with 3.5 V has $\rho_{N,3.5,\alpha} = \rho_{N,3.5,\beta} = 61\Omega/\square$. The aluminum anodized with 4.2 V came out were not identical

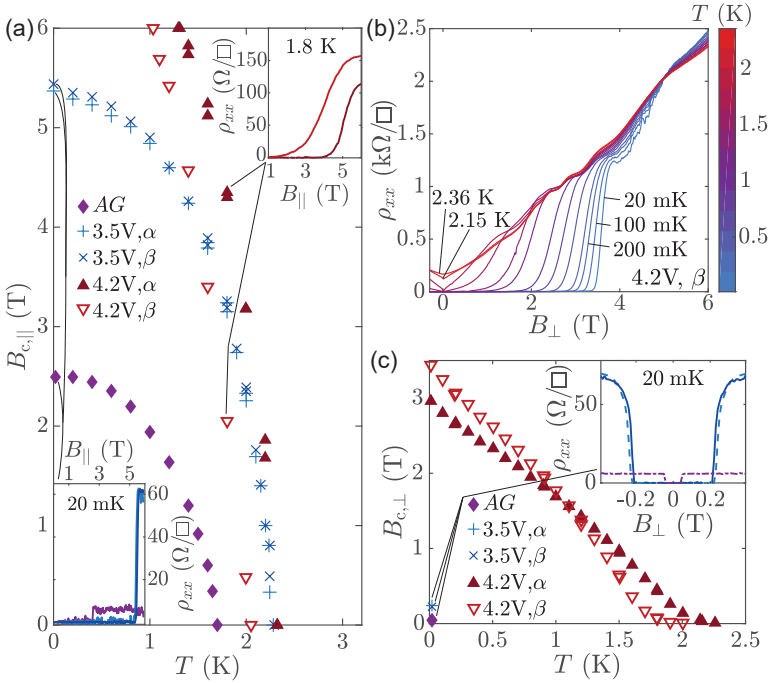


Figure 5.2: Enhanced Al on InAs 2DEG. (a) Temperature dependence of $B_{c||}$ for Hall bar of as grown Al (AG) and for Hall bars with AO performed at 3.5 and 4.2 V. Data from both devices, α and β , are included. Some of the 4.2 V points were measured twice. Examples of $\rho_{xx}(B_{||})$ scans are included in the insets, acquired at the stated temperatures. (b) ρ_{xx} as a function of B_{\perp} at different temperatures for the Al film on device β anodized at 4.2 V. (c) Extraction of $B_{c,\perp}(T)$ for both Al films anodized at 4.2 V. Base temperature $B_{c,\perp}$ for both Hall bars anodized at 3.5 V and AG are included. Those data are extracted from scans displayed in the inset.

on the two devices with $\rho_{N,4.2,\alpha} = 120\Omega/\square$ and $\rho_{N,4.2,\beta} = 160\Omega/\square$. Both 4.2 V Hall bars have broad superconducting transitions. The critical fields are extracted as $\rho_{xx}(B_{c,\parallel}) = 0.01 \cdot \rho_N$. T_c at 0 and 6 T was obtained through temperature sweeps at those fields. The critical field and temperature for AG are $B_{c,\parallel} = 2.49$ T and $T_c = 1.70$ K while for the 3.5 V exposed films, we find $B_{c,\parallel} = 5.44$ T and $T_c = 2.31$ K. The thinnest films, the 4.2 V anodized Hall bars on device α and β , both have in-plane critical fields exceeding 6 T. The critical temperatures at 0 and 6 T are 2.32 K and 1.30 K for 4.2 V, α and 1.03 K and 2.05 K for 4.2 V, β .

Both of the 4.2 V devices have normal state resistivities an order of magnitude lower than the resistivity of AO_1 on GaAs, supposedly due to having the less resistive 2DEG in parallel. The fact that $\rho_{N,4.2,\beta} > \rho_{N,4.2,\alpha}$ tells us that the Hall bar on device β has a thinner or more disordered Al film. Simultaneously it has a lower T_c indicating that we are beyond the optimal thickness and disorder after which T_c is expected to drop [42, 43].

The significant differences of the two 4.2 V Hall bars indicates a lack of repeatability. For these few mono-layer (ML) thick aluminum films a small change in thickness and disorder has a significant impact on the Al properties since the films are close to the superconductor-insulator transition. Even a difference on the order of a ML, would affect these devices. This fact makes the films good probes for repeatability of the used AO procedure. Even though the devices were made simultaneously in the same fabrication steps, the points mentioned in subsection 3.3.3 cause the different outcomes. Another source could be slight non-uniformity in Al growth thickness.

Figure 5.2(b) shows $\rho_{xx}(B_{\perp})$ scans at different temperatures of the $V_{AO} = 4.2$ V, β device, while data from $V_{AO} = 4.2$ V, α is shown in appendix section C.2. Data for AG and 3.5 V anodized Hall bars were only measured at base temperature and are displayed in inset of figure 5.2(c). In both 4.2 V anodized bars we see a crossing of the isotherms as was observed on the GaAs substrate, figure 4.3(b). There, the $\rho_{xx}(B_{\perp})$ saturated shortly after the crossing. Saturation is not observed in fig:InAsScTransport(b), but might happen at larger fields.

Other features that clearly indicate the presence of InAs 2DEG is the ρ_{xx} oscillating and increasing with B_{\perp} . These oscillations are elaborated in [chapter 7](#).

Even though the normal state resistance increases in B_{\perp} , to extract $B_{c,\perp}(T)$, we use 1% of the same ρ_N that was used when extracting $B_{c,\parallel}(T)$. The result is displayed in [figure 5.2\(c\)](#) together with extractions from the other four Hall bars. Both of the 3.5 V Hall bars and the AG bar were only measured at base temperature, line scans shown in the inset. $B_{c,\perp}(T \sim 20 \text{ mK}) = 40 \text{ mT}$ for AG bar, 230 mT for the 3.5 V Hall bars, while 4.2 V, α and β have $B_{c,\perp} = 2.96 \text{ T}$ and 3.45 T, respectively. As observed for anodized Al on GaAs substrate, [figure 4.3\(c\)](#), $B_{c,\perp}$ is increased by more than two orders of magnitude. For the thinnest Al bars, the $B_{c,\perp}(T)$ dependence is close to linear with an upward curvature close to T_c .

As found in [chapter 4](#), T_c and especially B_c of epitaxially grown Al films were found to increase significantly through partial oxidation. Of the two 4.2 V Hall bars, β has both the lowest T_c and highest $B_{c,\perp}$, indicating that it is the thickness and/or disorder that enables these 2 orders of magnitude increases of $B_{c,\perp}$.

5.3 SURFACE PASSIVATION

Further increase of V_{AO} enables full oxidation of the as-grown Al film, entirely turning it into alumina. Such a process allows for both passivation of the semiconductor underneath and for removal of the metallic Al. As the electrostatic screening of metallic Al is removed, it enables manipulation of the charge carrier density in the semiconductor via a top-gate, see [subsection 2.1.2](#).

[Subsection 5.3.1](#) studies the changes in carrier density and mobility while [subsection 5.3.2](#) presents a high perpendicular magnetic field B_{\perp} study of the highest mobility Hall bar to investigate quantum Hall effect.

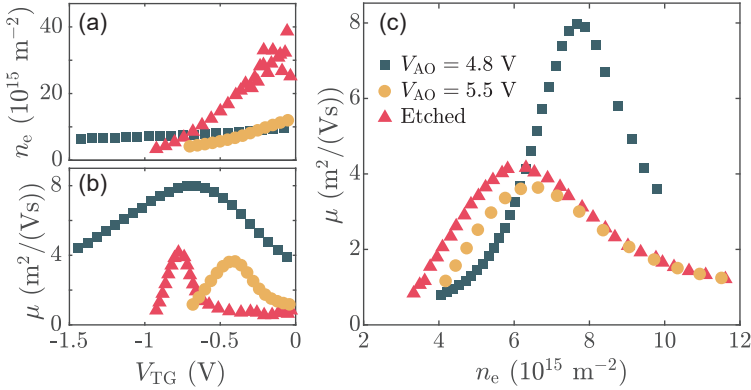


Figure 5.3: **Increased carrier mobility with AO.** Comparison of Hall bar mobility and density versus top-gate voltage for three different devices, identified by the legend in (c). The red triangles represent data from the etched Hall bar in [figure 3.4](#). The yellow circles and blue squares are from Hall bars anodized at 5.5 V and 4.8 V respectively.

(a) Carrier density as a function of top-gate voltage. (b) Carrier mobility as a function of top-gate voltage. (c) Carrier mobility as a function of carrier density.

5.3.1 Increased carrier mobility

Top-gate biasing was found to be possible on Hall bars anodized at $V_{AO} = 4.8 \text{ V}$ and 5.5 V , see [figure 5.3\(a-b\)](#), suggesting that the residual metallic Al film is discontinuous or completely oxidized. Here in the main text we present Hall bars anodized at $V_{AO} = 4.8 \text{ V}$ and 5.5 V from device α while data from $V_{AO} = 4.8 \text{ V}$, β is presented in [Appendix section C.3](#) and [section C.4](#).

Characterization of the two Hall bars was done by measuring longitudinal resistivity ρ_{xx} and Hall resistivity ρ_{xy} as a function of out of plane magnetic field B_{\perp} and top-gate voltage V_{TG} to extract carrier density n_e and carrier mobility μ , as shown in [subsection 2.1.1](#). These are compared to the Hall bar produced by Al wet etch, presented in [figure 3.4](#). In

Hall bar	$\max \mu$	$n_e(\max \mu)$	$\max l_e$
4.8 V	$8.0 \cdot 10^4 \text{ cm}^2/\text{Vs}$	$n = 7.7 \cdot 10^{11} \text{ cm}^{-2}$	$1.16 \text{ } \mu\text{m}$
5.5 V	$3.2 \cdot 10^4 \text{ cm}^2/\text{Vs}$	$n = 6.5 \cdot 10^{11} \text{ cm}^{-2}$	492 nm
Etched	$4.2 \cdot 10^4 \text{ cm}^2/\text{Vs}$	$n = 6.1 \cdot 10^{11} \text{ cm}^{-2}$	541 nm

Table 3: **Carrier properties for various Hall bars.** Mobility peak and corresponding density is extracted from [figure 5.3\(c\)](#) and mean free path is calculated by [equation 2.17](#).

[figure 5.3](#) we display V_{TG} dependence of μ versus n_e for the three Hall bars.

Measured carrier densities are displayed in [figure 5.3\(a\)](#) as a function of V_{TG} . For all Hall bars, n_e decreases monotonically by negatively biasing V_{TG} with an exception of the etched having fluctuations for $V_{\text{TG}} > -0.3$ V. At $V_{\text{TG}} = 0$, the etched Hall bar has $n_e \sim 4.0 \cdot 10^{12} \text{ cm}^{-2}$, while the Hall bars anodized at 5.5 V and 4.8 V have $n_e = 1.1 \cdot 10^{12} \text{ cm}^{-2}$ and $n_e = 9.8 \cdot 10^{11} \text{ cm}^{-2}$ respectively. The same order is observed in the slope of n_e vs V_{TG} , with the etched Hall bar having the steepest slope and the 4.8 V Hall bar slope being the flattest.

The corresponding mobilities are shown in [figure 5.3\(b\)](#) as a function of V_{TG} and in [figure 5.3\(c\)](#) as function of n_e . The shape of mobility versus density curves is similar for etched and anodized Hall bars. They are therefore all interpreted according to the explanation given in [subsection 3.1.4](#).

The mobility peak and corresponding density and mean free path are presented in [table 3](#). We see a factor ~ 2 increase of peak mobility from the $V_{\text{AO}} = 4.8$ V Hall bar compared to the etched Hall bar, while the $V_{\text{AO}} = 5.5$ V Hall bar has a decreased peak mobility.

Two factors could play a role in the increased mobility peak after AO at 4.8 V. The lack of being exposed to an Al etch, such as Transene, and an alumina passivation of the III/V, as depicted in [figure 5.1\(d\)](#). Together, these decrease surface scattering compared to the etched Hall bar.

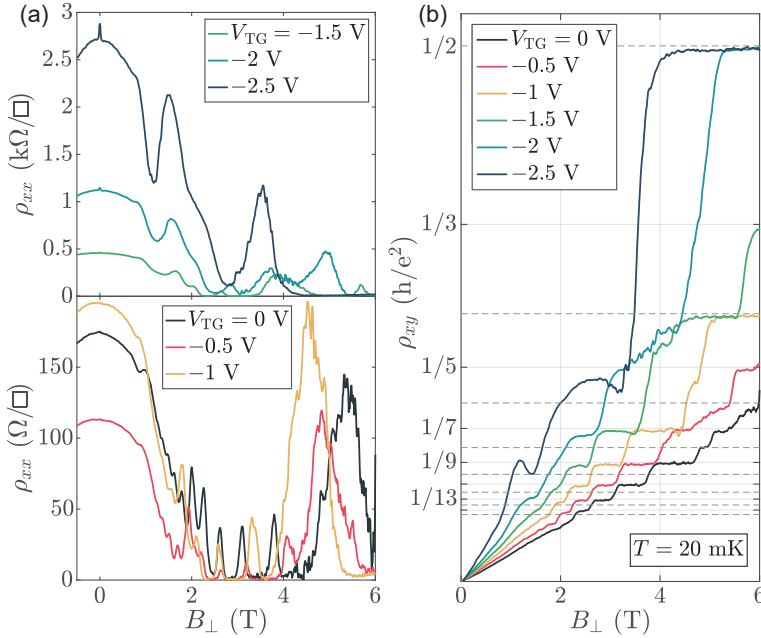


Figure 5.4: **SdHO and Hall quantization.** Quantum Hall effect data at 20 mK from the Hall bar anodized at 4.8 V. Longitudinal (a) and Hall (b) resistivities as a function of B_{\perp} for different top-gate voltages in between 0 and -2.5 V with a step of 0.5 V. Hall resistivity is displayed in integer fractions of h/e^2 . Even denominators are displayed by dashed lines while odd denominators are marked as solid lines.

AO at 5.5 V showed decreased mobility peak compared to the etched Hall bar. We suspect that 5.5 V introduces disorder by contributing to oxidation of the semiconductor underneath, as depicted in figure 5.1(e).

5.3.2 Integer quantum Hall effect in shallow InAs 2DEG

Measurements of ρ_{xx} and ρ_{xy} as a function of top-gate voltage V_{TG} and high perpendicular magnetic field B_{\perp} (up to 6 T) was done for the Hall bars with the highest mobilities, anodized at 4.8 V. This subsection

presents data from the highest mobility Hall bar on from device α while the data from device β is presented in [section C.4](#).

[Figure 5.4\(a\)](#) shows ρ_{xx} as a function of B_{\perp} for different V_{TG} between 0 and -2.5 V. Shubnikov de Haas oscillations (SdHO) are visible for $B_{\perp} > 1$ T with vanishing minima of ρ_{xx} for $B_{\perp} \sim 2.5$ T. This is ~ 1 T lower than our highest superconducting $B_{c,\perp}$ reported in [section 5.2](#). Concurrently with vanishing ρ_{xx} , resistance plateaus are observed in [figure 5.4\(b\)](#) for ρ_{xy} with $B_{\perp} > 2$ T, which is consistent with quantum Hall effect signatures, see [subsection 2.2.4](#).

Besides SdHO, additional ρ_{xx} peaks are present in [figure 5.4\(a\)](#). Starting at the three least negative $V_{\text{TG}} = [0, -0.5, -1.0]$ V, a broad and tall resistivity spike is observed between 4 and 6 T and a smaller increment to ρ_{xx} is observed just below 2 T. For the most negative V_{TG} , the high field spike moves towards 3 T, and the increment below 2 T becomes more prominent. Lastly a weak localization peak as discussed in [subsection 2.2.2](#) is observed around $B_{\perp} = 0$.

As for ρ_{xx} , additional features are observed in the Hall resistivity as well. At fields where ρ_{xx} has additional spikes, ρ_{xy} exhibits noise and forms non-integer plateaus. Below 4T, ρ_{xy} only has plateaus at odd fractions. This fact is more clear in [figure 5.5\(a\)](#), displaying a color map of $\rho_{xy}(V_{\text{TG}}, B_{\perp})$, from which we extract the filling factor ν and display it across the map. The same ν are added to a color map of $\rho_{xx}(V_{\text{TG}}, B_{\perp})$, [figure 5.5\(b\)](#), showing a Landau fan diagram with additional features. The most obvious of these is a resonance crossing the Landau fan at high fields, marked by red arrows, which is the origin of the high field resistance spikes mentioned above. We notice that above the resonance, ν has regular even integer counting with spin-splitting into odd values around $B_{\perp} \sim 5$ T. Below the resonance, ν has odd integer counting. Another, less prominent resonance, marked by the blue arrow, is the origin of the increment and spikes below 2 T in [figure 5.4\(a\)](#). A better visualization of the low-field features is obtained from an un-saturated color map of $\rho_{xx}(V_{\text{TG}}, B_{\perp})$, displayed in [figure 5.5\(c\)](#).

Similar ρ_{xx} resonances and odd ρ_{xy} counting turning into even counting when crossing a high field resonance was observed in the high field

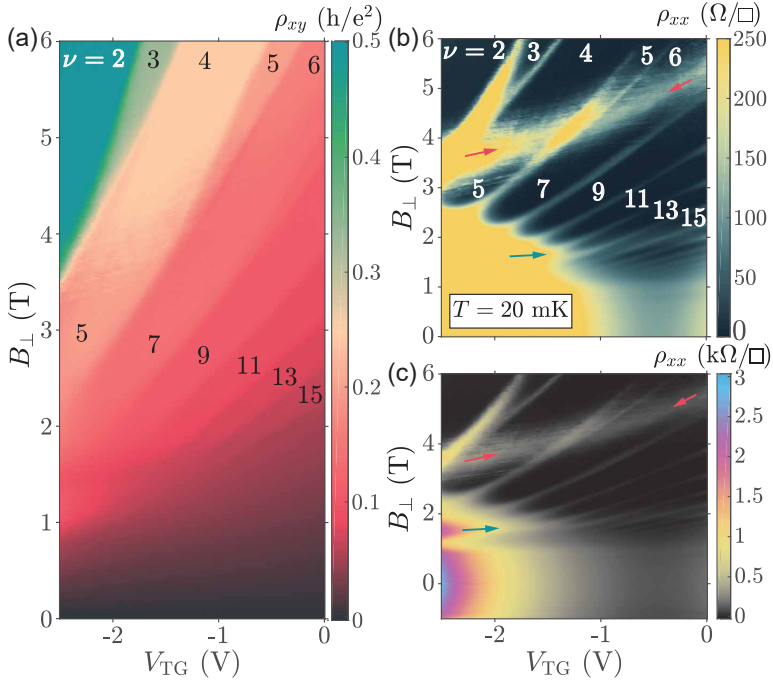


Figure 5.5: **QHE resistivity maps.** Quantum Hall effect data at 20 mK from the Hall bar anodized at 4.8 V. 2D map of the (a) Hall and (b) longitudinal resistivities as a function of B_{\perp} and top-gate V_{TG} . Longitudinal resistivity is saturated to highlight the Landau fan. Extracted filling factors are indicated on the maps. Arrows in (b) highlight additional resonances. (c) Same data as shown in (b), but without color saturation, allowing us to see more features. Additional resonances are marked with arrows. Especially the resonances below 2 T, (blue arrows) are more striking on the unsaturated plot.

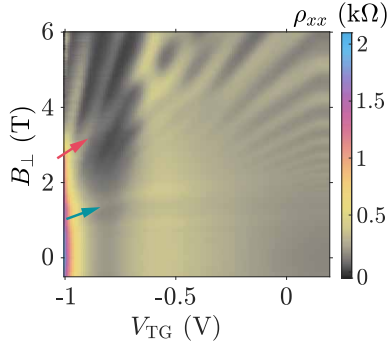


Figure 5.6: **High B_{\perp} ρ_{xx} -measurements of etched Hall bar.** 2D maps of the longitudinal resistivity as a function of B_{\perp} and top-gate V_{TG} . Arrows highlight additional resonances.

study, done on the 4.8 V Hall bar on device β , presented in Appendix section C.4.

Speculations about the origin of extra resonances in ρ_{xx} and the addition to ν that comes with them lead to an interpretation including a low density 2nd band from an additional quantum well. The extra resonances represent its fan-diagram, superimposed on the other. The broad fans indicate a low mobility. To explain the observed combined filling factor ν , we suggest that crossing the high field resonance, marked by red arrows in figure 5.5(b-c), takes the 2nd 2DEG filling factor from $\nu_{2nd} = 1$ to 0. Depletion of a Hall bar with B_{\perp} is commonly observed in the study of disordered 2DEGs [131]. The origin of such a 2nd band and where it would reside is not clear. It could live in an unintentional quantum well deeper in the heterostructure. One might also expect the AO process to be the cause. To verify whether the additional band is intrinsic for the material we measured an etched Hall in large perpendicular fields, see figure 5.6. Extra resonances are also observed here, suggesting that the extra bands are not AO-related. When studying new growths, we propose to do similar IQHE measurements to verify whether a single or multiple quantum wells are present in a given heterostructure. This knowledge makes interpreting device data a lot easier.

5.4 CONCLUSION

This chapter studied the effect of AO on Hall bars made out of shallow InAs 2DEG heterostructures with epitaxially grown Al on the top. We have shown that oxidizing the Al on the Hall bars, rather than stripping it by wet etching, can lead to enhanced properties of the Al and the 2DEG. Different oxidation depths were obtained by applying different anodic oxidation voltages: 3.5, 4.2, 4.8, and 5.5 V.

Partially oxidized Al showed enhanced critical fields with $B_{c,\parallel} > 6$ T and $B_{c,\perp}$ up to ~ 3.5 T. Compared to the AG bar, this is more than a doubling of $B_{c,\parallel}$ and 2 orders of magnitude increase of $B_{c,\perp}$. With only a slight relative increase in T_c , up to 2.3 K, the ratio $B_{c,\parallel}/T_c \propto B_{c,\parallel}/\Delta$ is increased significantly. This is promising for Majorana physics applications, since it increases the topological gap, see [subsection 2.4.5](#).

The very high critical fields are possible due to the Al film being disordered. It is to our knowledge a novel material system to have a disordered superconductor in strong proximity coupling to a 2DEG. In [chapter 7](#), we will further study this new system.

Coating the heterostructure with alumina, through full oxidation of the grown Al, increases mobility peak up to $80 \cdot 10^3 \text{cm}^2/\text{Vs}$, twice the value obtained with regular Al etch. Oxidizing too deep reduces the mobility peak.

Within the 600 – 700 mV spacing between the different applied V_{AO} there are, most likely, voltages that could result in even higher B_c or μ .

Integer quantum Hall effect ($\rho_{xx} = 0$) was observed at ~ 2.5 T, giving 1 T overlap with the highest superconducting $B_{c,\perp}$, enabling future research into superconductor-IQHE hybrids. This is intriguing since we know that the interface is pristine, insuring close to unity Andreev reflection probability. With this approach, the superconductor can be patterned on top of the IQH liquid while for other material systems the superconductor only interacts with QH-states from the edge [[85](#), [96](#), [98](#), [99](#), [101](#), [132](#)].

Anodic oxidation voltages in between 4.2 V and 4.8 V has not yet been tested. It might be that higher critical field or better 2DEG passivation could be achieved by trying other anodization voltages.

These results encourage a reconsideration of the processes we apply to pattern Al on our hybrid structures. Not only 2DEGs, but also vapor-liquid-solid nanowires and selective area growth could potentially benefit. Ideas are elaborated in [section 8.4](#).

ENABLING HIGH RESOLUTION LITHOGRAPHY WITH ANODIC OXIDATION

A crucial part in many modern solid state experiments is the ability to define objects on a nanometer scale to promote quantum mechanical features. The devices made out of anodic oxidation (AO) in [chapter 4](#) and [5](#) were micrometer-sized bars for which good lateral resolution was not necessary. To make small junctions or 1D wires for Majorana experiments, lateral resolution is a key requirement. This chapter presents our results in obtaining good lithographic resolution with AO by implementing a metal masks rather than regular electron-beam resists.

[Section 6.1](#) elaborates the problem with regular electron beam resists and introduces the idea of using a metal mask instead. [Section 6.2](#) presents the devices fabricated with a metal mask and [section 6.3](#) presents a in-depth study of a magnetic field resilient Josephson junction. Conclusions are made in [section 6.4](#).

These results are also presented in [[121](#)].

6.1 METAL MASKING

Combining lithography processes with anodic oxidation would open a new path to pattern the Al films on shallow semiconductor heterostruc-

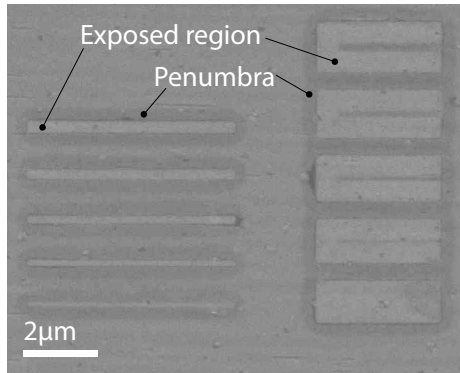


Figure 6.1: **Scanning electron microscopy of a test patterning by AO with an electron beam lithography resist mask.** The light regions are the developed regions directly exposed by anodic oxidation. The darker 'penumbra' are regions around the exposed areas, unintendedly being affected by anodic oxidation.

tures. In the pursuit of realizing this combination, different lithography masks were tested for compatibility. First attempts were done by trying various E-beam resist masks, all having the same problem. Broad regions on the order of 0.5 to 2 μm (penumbrae) formed under the resist masks, not enabling nanometer sized devices. The penumbra was observed with scanning electron microscopy (SEM), see [figure 6.1](#)

Subsequently, the use of metal masks was tried and showed an improved accuracy. The process steps are displayed in [figure 6.2](#). The idea is based on the assumption that the oxidation depth only is controlled by the applied voltage V_{AO} [117]. An initial global AO defines the overall Al thickness through a partial oxidation. Deposition of a thin metal mask is patterned where Al should stay metallic. A final AO, with a larger voltage, fully oxidizes the Al not covered by the mask as well as oxidizing the mask itself. This approach assumes that the result of the final AO does not depend on whether or how the initial AO was done.

To avoid having floating metal hovering above devices, we evaporated thin metal masks that would get fully oxidized when shielding the grown Al from AO, leaving behind an extra dielectric. Titanium was used since

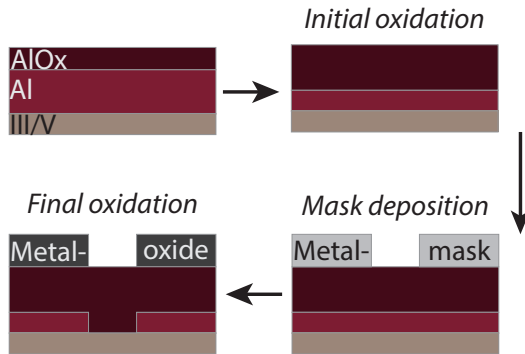


Figure 6.2: **Metal mask process flow.** Schematic illustration of the fabrication process combining standard lithography techniques with metal masks and anodic oxidation. An initial AO defines the overall Al thickness. The metal mask is patterned on top of places where Al should stay metallic. A final oxidation fully oxidizes exposed Al as well as the metal mask.

we could deposit a continuous layer of only 2-3 nm thickness. Liftoff of such thin Ti films proved tedious. Sonication was necessary for the Ti not to redeposit in random places on the chip, see [section B.6](#).

A mask of Al would be preferable, but we did not have a sufficiently cooled evaporation chamber, necessary to get uniform Al layers of a few nm thickness [10].

SEM micrographs didn't show any signs of penumbrae, but they could be hiding under the Ti. Therefore, narrow devices, such as the one in [figure 6.5\(a\)](#), were designed to validate the lateral extent of the oxidation in transport measurements.

6.2 DEVICES FOR EVALUATING THE FAB

A chip from M26 (see [subsection 3.1.4](#)) was fabricated using double AO and a Ti mask, as elaborated in [section 6.1](#). Different devices were made including a Hall bar, an Al Bar, Josephson junctions and S-QPC-N devices (see [figure 3.6](#)). The latter didn't show clear spectroscopy of an induced gap. Various colleagues have stated that some forms of titanium

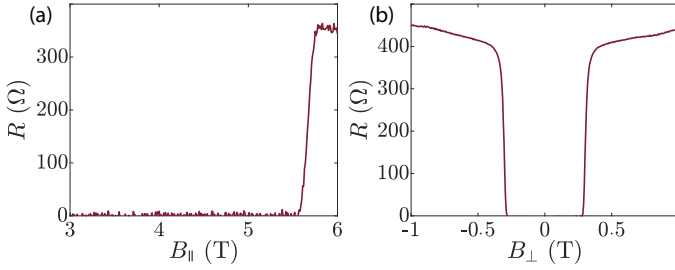


Figure 6.3: **Characterization of superconducting bar after double AO with Ti mask.** (a) Resistance versus in-plane magnetic field. (b) Resistance versus perpendicular magnetic field.

oxide has charge traps that will absorb and disperse charges. We thus suspect the presence of titanium oxide to be the reason for unsuccessful spectroscopy.

The Hall bar and Al bar were used to characterize the quality of the semiconductor and the Al film after AO. The initial oxidation was done at 3.5 V for 5 min. This value was chosen to obtain a high critical field, but still below our magnets limit of 6 T, similar to 3.5 V in figure 5.2. The resulting Al film had $B_{c,||} \approx 5.6$ T and $B_{c,\perp} \approx 300$ mT, see figure 6.3. The agreement between results of the two 3.5 V exposures indicates consistency of the AO setup.

To obtain a favorable mobility, $V_{AO} = 4.8$ V was used for second AO, inspired by the good results from figure 5.3. The resulting Hall bar showed a mobility peak of $11.6 \cdot 10^3$ cm²/Vs at a density of $7.2 \cdot 10^{11}$ cm⁻², see figure 6.4. This value is much lower than expected, suggesting the oxidation process was too deep and impacted the semiconductor. An unintended oxidation depth could be due to a time-dependent AO process. This was later confirmed in a separate test elaborated in section 8.2. Without a time-dependence, the final AO, with the largest V_{AO} , solely controls the oxidation thickness. With a time-dependence, the depth of the initial and final oxidation would add up, making our current setup non-ideal for the metal mask recipe.

The Josephson junctions (JJs) were made narrow with 100 nm thin and 5 μ m long elongated superconductor leads, displayed with an electron

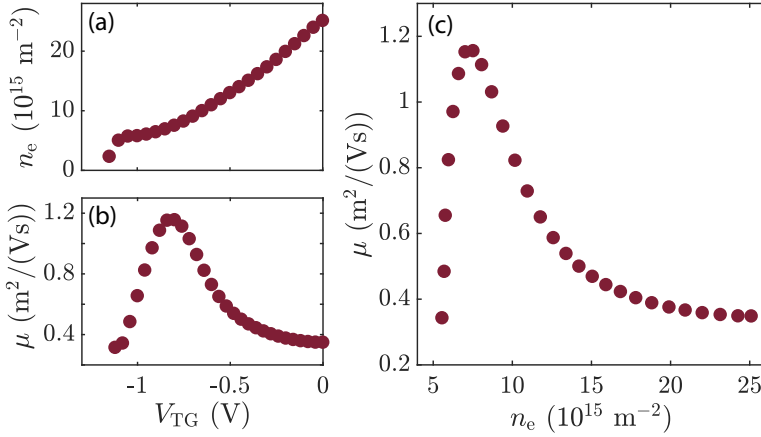


Figure 6.4: **Characterization of semiconducting bar after double AO with Ti mask.** (a) Hall bar carrier density as a function of top-gate voltage V_{TG} . (b) Hall bar carrier mobility as a function of top-gate voltage. (c) Hall bar carrier mobility as a function of carrier density.

micrograph in [figure 6.5\(a\)](#). The distance between the two superconducting leads, the junction width, was varied between 100 and 400 nm. If the devices come out functional, the lateral resolution has to be better than 50 nm in either direction.

These design dimensions are subject to possible changes during fabrication, eg. from a lateral oxidation. The 100 nm wide junction is presented in this chapter, while data from the three broader junctions can be found in the appendix [section C.5](#).

A schematic of measurement setup and applied field directions are also shown in [figure 6.5\(a\)](#). An out-of-plane field B_{\perp} is used in combination with an in-plane field B_z , specifically oriented perpendicular to the junction. An AC current bias of 0.5 nA was applied with possibility of adding DC bias, I_{DC} , while an AC voltage drop was measured. A top-gate V_{TG} was used to deplete or populate the junction with carriers. The two wire gates V_W , biased at -1.6 V, were used to form the nar-

row junction in the InAs 2DEG enabled by electrostatic screening of the metallic aluminum, as elaborated in [79].

Gateability of the critical current is displayed in figure 6.5(b) where the differential resistance (dV/dI) is measured as a function of I_{DC} and V_{TG} . A critical current of $\sim 1.1 \mu\text{A}$ is obtained at $V_{TG} = 0 \text{ V}$. It decreases by negatively biasing V_{TG} until pinch-off. Before pinch-off, the red part of the map corresponds to the normal state of the Al films, while green corresponds to the normal state of the junction.

The impact of B_{\perp} on the critical current is shown in figure 6.5(c), acquired with $V_{TG} = 0 \text{ V}$. As elaborated in subsection 2.4.4, a Fraunhofer pattern, described by equation 2.74:

$$I_c(B_{\perp}) = I_c(0) \left| \frac{\sin(\pi B_{\perp} A / \Phi_0)}{\pi B_{\perp} A / \Phi_0} \right|,$$

is expected for an ideal JJ. Φ_0 is the flux quantum and A the junction area. In our case, $A \sim 0.1 \times 5 \mu\text{m} = 0.50 \mu\text{m}^2$.

We do observe the critical current oscillating with B_{\perp} . Though periodic, figure 6.5(c) does not display well-defined sinusoidal nodes, possibly due to the narrow and elongated superconducting leads. For comparison, a Fraunhofer pattern is superimposed the data of figure 6.5(c) using equation 2.74 with $I_c(B_{\perp} = 0) = 1.23 \mu\text{A}$ and $\Phi_0/A = 4.6 \text{ mT}$. The period of $\sim 4.6 \text{ mT}$ matches with our data. It corresponding to an area of $0.45 \mu\text{m}^2$ not far from the expected value. The corresponding junction width is 90 nm , very close to the intended 100 nm , suggesting a good lateral lithographic resolution.

The perpendicular critical field is estimated to 310 mT as evidenced in the large field Fraunhofer pattern of figure 6.6. This value is consistent with the critical field of full-sheet anodized Al, figure 6.3. The amplitude of the anti-nodes doesn't follow the expected $\propto 1/B_{\perp}$ dependence from equation 2.74, but seem to flatten out at high fields.

6.3 FIELD-INDUCED SUPERCURRENT OSCILLATIONS

Josephson junctions based on shallow 2DEGs should, according to theoretical proposals [7, 8], have a B_z driven topological phase transition.

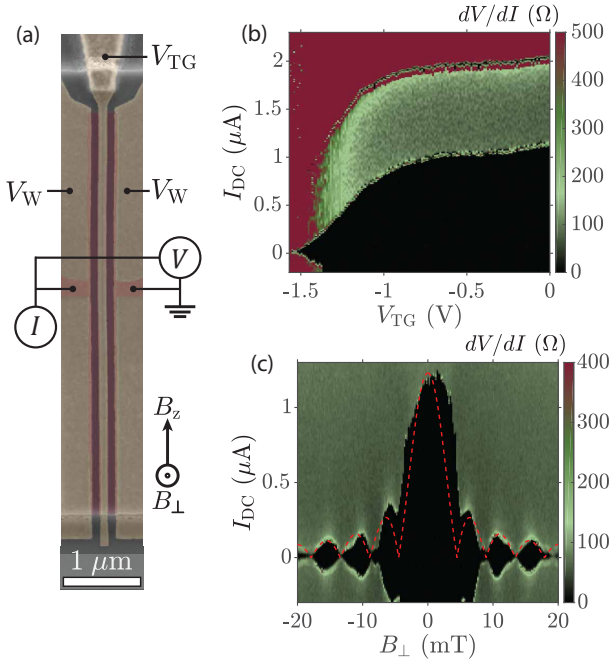


Figure 6.5: **AO defined Josephson junction.** (a) False-color scanning electron micro-graph of the reported narrow Josephson junction. The remaining thin Al layer is in red, and the gates are colored yellow. The two side gates V_W are kept at -1.6 V for the experiments. Transport was current-biased and 4-terminal voltage drop (V) was measured. Field directions B_\perp and B_z are defined in the bottom left part of the figure. (b) Saturated color map of the differential resistance dV/dI as a function of current bias I_{DC} and top-gate voltage V_{TG} . (c) Saturated color map of dV/dI as a function of current bias and perpendicular field. Data taken with $V_{TG} = 0$. Red dashed curve is an actual Fraunhofer pattern from equation 2.74 using $I_c(B_\perp = 0) = 1.23 \mu\text{A}$ and $\Phi_0/A = 4.6$ mT.

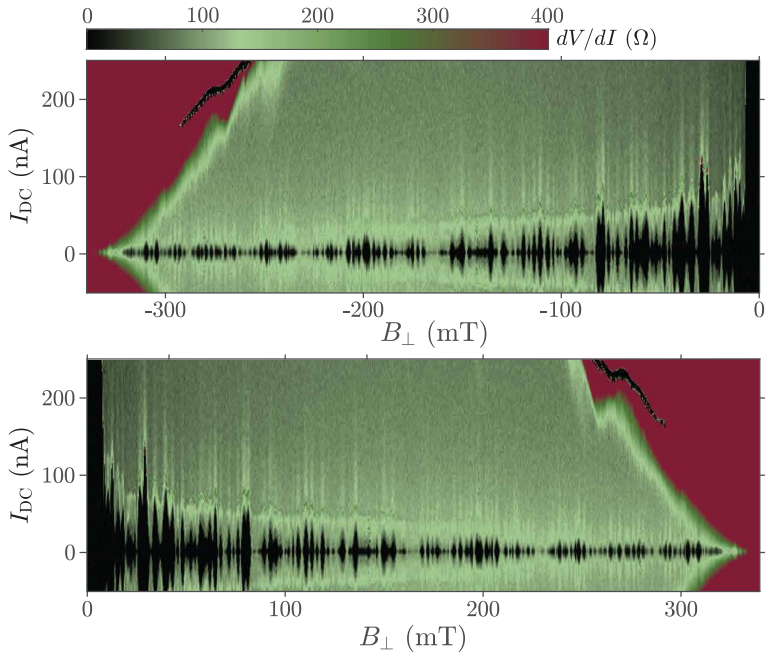


Figure 6.6: **Josephson junction in high B_{\perp} .** Saturated color map of dV/dI as a function of current bias and perpendicular field. Data taken with $V_{TG} = 0$.

Critical current is expected to oscillate with B_z having nodes at the phase transition. Motivated hereby, two reported experiments [79, 113] explored the effect of in-plane critical field on JJs in Al/InAs 2DEG heterostructures. Though limited by the critical field of as-grown Al, both experiments reports oscillations of critical current with B_z . Ref. [79] associates the oscillations with a Fraunhofer-like effect from the in-plane field.

Having a JJ made from a high critical field superconductor, we test the field limitations of the supercurrent, which we define as places in parameter space where resistance can't be distinguished from our measurement noise floor. Differential resistance dV/dI was measured at $I_{DC} = 0$ as a function of B_z and B_\perp with $V_{TG} = 0$, displayed in figure 6.7. Similar maps were taken at different V_{TG} values. The field directions were aligned to the device axes before data acquisition. A complicated pattern is observed with quenching and reappearance of the supercurrent as a function of both field directions.

The following observations are made for $V_{TG} = 0$: At low $B_z < 1$ T, supercurrent persists for all $B_\perp \in [-20 : 20]$ mT. Beyond 1 T resistive regimes emerges and broadens out. No supercurrent is present after $B_z > 4$ T, besides two superconducting blobs appearing at high fields $B_z \sim 5.5$ T, just before the Al turns normal.

Independent of V_{TG} , certain B_z values [~ 1.8 T and ~ 5.5 T] has dips in dV/dI . To get a more qualitative characterization, we studied the switching current I_{sw} , defined as the maximum critical current for any B_\perp in a 10 mT interval, extracted from scans like figure 6.5(c). I_{sw} was extracted with fixed B_z values between -0.3 T and 5.8 T.

Figure 6.8(a) displays evolution of I_{sw} as a function of B_z for different V_{TG} values between +0.35 V and -1.3 V. For $V_{TG} = -1.3$ V and -1.1 V, we observe the supercurrent being quenched around $B_z \sim 1$ T. For $V_{TG} = -0.6$ V, the junction goes resistive as well, but superconductivity reemerges between 1.5 and 2 T. For $V_{TG} = 0$ and +0.35 V, I_{sw} sustains up to ~ 3.4 T, with a local peak around 1.7 T. As observed on figure 6.7(a-b) I_{sw} reemerges between 5.2 and 5.5 T, close to the critical field of the superconductor itself. V_{TG} was not driven more positive due to emergence of gate-leakage.

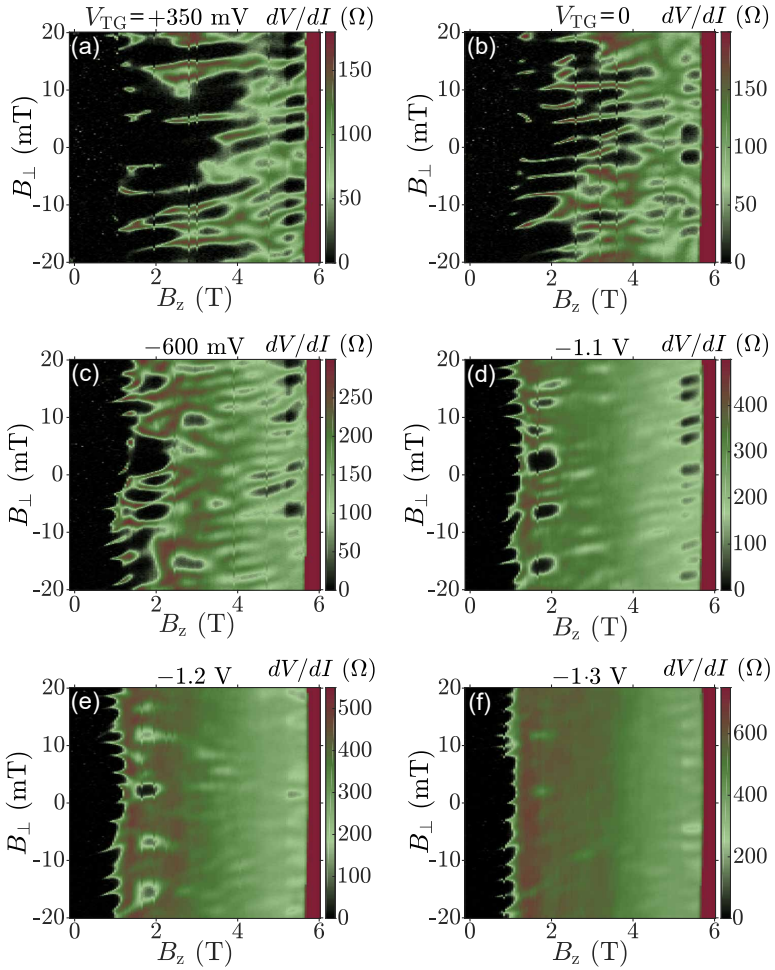


Figure 6.7: **Supercurrent oscillations.** Study of supercurrent oscillations as a function of magnetic field and top-gate voltage. Differential resistance is plotted versus B_z and B_{\perp} for different V_{TG} , indicated above the maps: (a) +350 mV, (b) 0, (c) -600 mV, (d) -1.1 V, (e) -1.2 V, and (f) -1.3 V.

Resistance of the junction in the normal regime also oscillates with B_z . To quantify this, we extract the minimum dV/dI for every value of B_z in each map of [figure 6.7](#). We call it the background resistance $R_{bg}(B_z, V_{TG})$ and plot it for the different V_{TG} in [figure 6.8\(b\)](#).

Field values causing dips in R_{bg} are clearly correlated with the fields causing peaks in I_{sw} across all V_{TG} . Those field values are thus independent of the InAs chemical potential. The B_z value resulting in a topological phase transition is expected to have a chemical potential dependence. We therefore attribute the oscillations to be B_z -induced orbital effects as reported in [79]. For an orbital effect, periodic nodes and anti-nodes should be expected. With I_{sw} peaks at $B_z \sim 1.7$ T and ~ 5.4 T, we could be observing 1st and 3rd anti-node, while a 2nd anti-node around $B_z \sim 3.5$ T could be suppressed.

6.4 CONCLUSION

A thin titanium layer was evaporated to mask AO instead of using a regular E-beam mask that results in penumbrae. An initial AO thinned down Al to a desired thickness with $B_{c,\parallel} \approx 5.6$ T and $B_{c,\perp} \approx 300$ mT. The final AO, done after Ti evaporation, lead to a too deep oxidation of the areas not covered by Ti, giving a carrier mobility of $11.6 \cdot 10^3$ cm²/Vs.

Narrow JJs were made to verify the resolution of the AO lithography with metal masks. A gateable junctions verifies that the Al leads are not shorted and the period of Fraunhofer-like oscillations indicates that the leads are not broken. This tells us that the horizontal lithographic resolution is better than 50 nm, both away from and in-under the metal mask.

With a high critical field, supercurrent oscillations are studied as a function of B_z (an in-plane magnetic field, perpendicular to the junction). The oscillations in B_z are not correlated with a topological phase transition due to independence of the chemical potential.

Though allowing good lateral lithography, this method lead to an over-oxidized semiconductor region and spectroscopy did not turn out well. Ideas on how to address these issues are presented in [section 8.3](#).

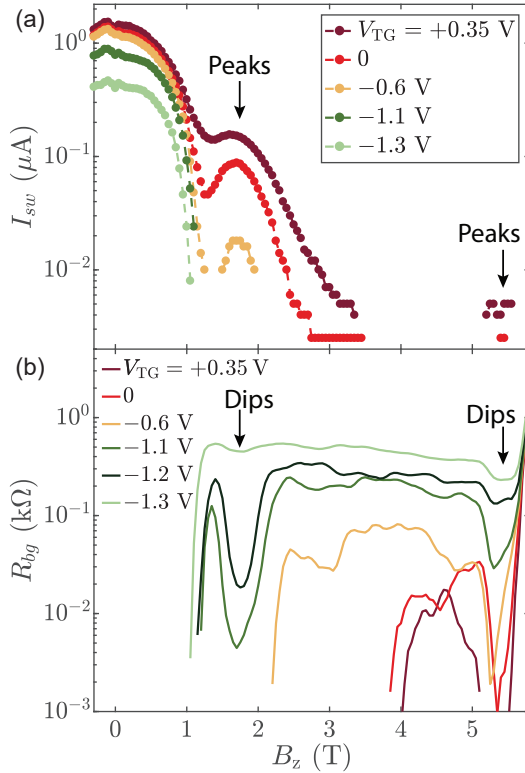


Figure 6.8: **Oscillations of switching current and background resistance.** (a) Oscillation and re-emergence of switching current, I_{sw} (defined in text) versus B_z for different V_{TG} . (b) Background resistance versus B_z for different V_{TG} . Extracted from figure 6.7.

$\rho(B_{\perp})$ OSCILLATIONS IN SUPERCONDUCTOR / 2DEG HYBRID

In [chapter 5](#) we introduced the use of anodic oxidation (AO) to oxidize epitaxial Al grown on shallow InAs 2DEG heterostructures, resulting in a novel material system with disordered Al in strong proximity coupling to an underlying InAs 2DEG. The Hall bar anodized at 4.2 V on device β had the highest measured critical perpendicular field $B_{c,\perp} \approx 3.5$ T, while the similar bar on device α had $B_{c,\perp} \approx 3.0$ T. This chapter explores these hybrid structures by presenting observations and studies of $1/B_{\perp}$ periodic magnetoresistivity oscillations in 4.2 V anodized Hall bar on device β . Qualitatively similar observations from device α are displayed in [section C.6](#).

[Section 7.1](#) presents isotherms of magnetoresistivity as a function of $B_{c,\perp}$ leading to observation of $1/B_{\perp}$ periodic magnetoresistivity oscillations above and below $B_{c,\perp}$ of the Al film. The temperature and B_{\perp} dependencies of the oscillations below $B_{c,\perp}$ are reported in [section 7.2](#) and their DC current dependence in [section 7.3](#). The observations are summarized in [section 7.4](#) together with suggestions for more experiments to be done.

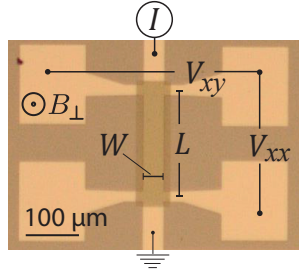


Figure 7.1: **Optical micrograph of the studied device**, the $V_{AO} = 4.2$ V Hall bar from device β , reported in [chapter 5](#). The Hall bars width W and length L are displayed with $L/W = 5$. AC current bias was applied to the Hall bar where V_{xx} and V_{xy} was measured as a function of perpendicular field B_{\perp} , temperature and DC current.

7.1 OBSERVATION OF MAGNETORESISTIVITY OSCILLATION

The device we study in this chapter is displayed in [figure 7.1](#). The Hall bar with length L and width W is defined in a shallow InAs 2DEG heterostructure with transparent proximity coupling to an epitaxially grown Al film. The Al was oxidized *ex situ* into a disordered superconductor, see [chapter 5](#). We will show data from measurements of magnetoresistivity, both longitudinal ρ_{xx} and Hall ρ_{xy} as a function of a perpendicular magnetic field, B_{\perp} , temperature, T , and DC current, I_{DC} .

A good place to start an exploratory study of a new superconducting system is looking at its isotherms which can help indicating phase transitions as the superconductor-insulator transition, see [subsection 2.3.7](#). Isotherms of $\rho_{xx}(B_{\perp})$ and $\rho_{xy}(B_{\perp})$ are presented in [figure 7.2](#). Below 2 K the device is superconducting. Once temperature drives Al in the normal state, the device has a significant Hall effect. Using [equation 2.15](#) we extract a density $n_e = 1.15 \cdot 10^{12} \text{ cm}^{-2}$ from the zero field Hall slope, very similar to the $n_e(V_{TG} = 0)$ of the anodized InAs 2DEGs presented in [subsection 5.3.1](#). The low density together with a critical superconducting temperature $T_c \sim 2$ K indicates a very strong electron-electron interaction [[28](#)].

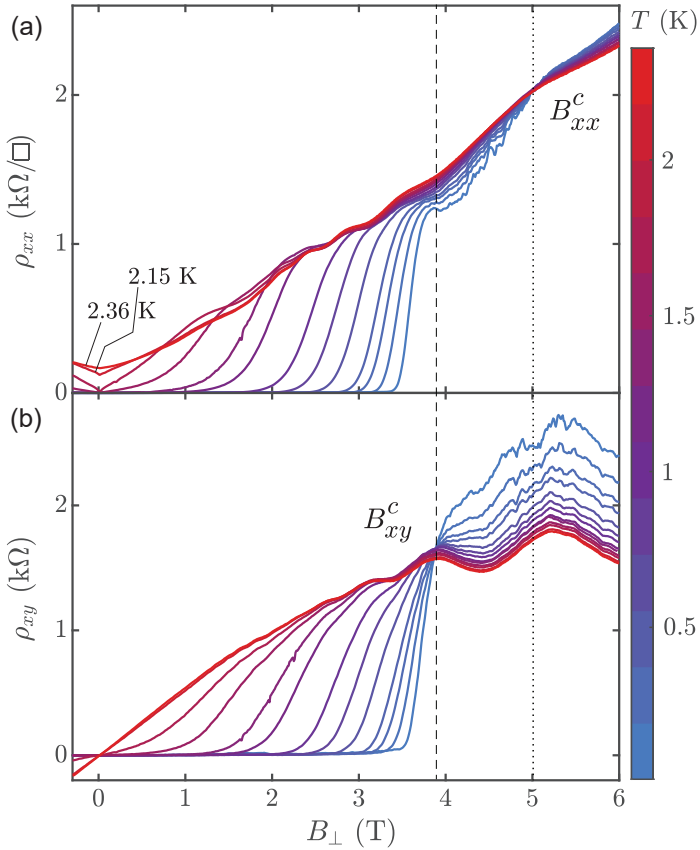


Figure 7.2: **Magneto-resistivity isotherms.** (a) Longitudinal and (b) Hall magneto-resistivity isotherms were measured simultaneously. Crossing of isotherms, B_{xx}^c are marked with dots and B_{xy}^c with stripes. The data of (a) is the same presented in figure 5.2(b).

Having Al in parallel with the 2DEG would usually lead to a vanishing Hall effect due to the high carrier density of Al. The Hall resistance from two channels in parallel is given by [133]

$$R_{xy} = \frac{B}{e} \frac{(\mu_1^2 n_{e,1} + \mu_2^2 n_{e,2}) + (\mu_1 \mu_2 B)^2 (n_{e,1} + n_{e,2})}{[(\mu_1 n_{e,1} + \mu_2 n_{e,2})^2 + (\mu_1 \mu_2 B)^2 (n_{e,1} + n_{e,2})^2]}, \quad (7.1)$$

with μ_1, μ_2 and $n_{e,1}, n_{e,2}$ being the carrier mobility and density of the two respective materials; in our case InAs and Al. At low fields where the Hall slope is extracted the expression is simplified to

$$R_{xy} = \frac{B}{e} \frac{\mu_{Al}^2 n_{e,Al} + \mu_{InAs}^2 n_{e,InAs}}{[(\mu_{Al} n_{e,Al} + \mu_{InAs} n_{e,InAs})^2]}. \quad (7.2)$$

In chapter 4, we saw a significant increase in the longitudinal resistance of anodized Al, which according to equation 2.14 suggests a reduced $n_{e,Al} \cdot \mu_{Al}$ product. For $n_{e,Al} \cdot \mu_{Al} \ll n_{e,InAs} \cdot \mu_{InAs}$, equation 7.2 reduces to

$$R_{xy} \approx \frac{B \mu_{InAs}^2 n_{e,InAs}}{e [(\mu_{InAs} n_{e,InAs})^2]} = \frac{B}{e n_{InAs}}. \quad (7.3)$$

Due to the high resistivity of the oxidized aluminum, the Hall effect we see from the hybrid could thus be dominated by the InAs 2DEG contribution.

Both ρ_{xx} and ρ_{xy} exhibit oscillations for $T > T_c$ showing similar $1/B_{\perp}$ periodicities. These are extracted by fast Fourier transform of their residuals using a Hamming window. Residuals were extracted by a smoothing spline fit ¹. Assuming that the oscillations are of SdHO-nature, a density $n_e \sim 7.5 \cdot 10^{11} \text{ cm}^{-2}$ is extracted from both using equation 2.34. The density is lower than that extracted from the zero field Hall slope. Assuming that μ_{Al} is very low, SdH is only expected from the InAs channel. The additional density extracted from the zero field Hall slope could be a carrier contribution from the oxidized Al. Another explanation for the difference in extracted densities the presence of e-e interaction, which only affects the Hall slope [134].

¹ <https://www.mathworks.com/help/curvefit/smoothing-splines.html>

Looking at $B_{\perp} > B_{c,\perp}$, we find that all the isotherms on [figure 7.2](#) cross at certain magnetic fields, which is characteristic for superconductor insulator transitions (SITs), see [subsection 2.3.7](#). The ρ_{xy} isotherms cross at $B_{xy}^c = 3.9$ T and later the ρ_{xx} crossing happens at $B_{xx}^c = 5.0$ T.

Field-driven SITs have been observed in several different disordered superconductors [[47–49](#), [111](#), [135–137](#)]. Some of those studies [[47–49](#)] report on the relationship between the isotherm crossing in ρ_{xx} and ρ_{xy} in indium-oxide films. Increasing B_{\perp} they first observe B_{xx}^c , relating it to a transition to a Bose-insulator, while at higher fields B_{xy}^c marks the global transition out of the superconducting phase. Early work [[48](#)] shows that B_{xx}^c/B_{xy}^c decreases from 1 by increasing disorder. A more recent study on TaN [[49](#)] also report on both B_{xx}^c and B_{xy}^c , but here a metallic density distinguished their samples from earlier studies that showed Bose insulator features. Still they report $B_{xx}^c < B_{xy}^c$.

The observation of $B_{xx}^c > B_{xy}^c$, different from all earlier observations, could be due to our system being shorted to a 2DEG with additional orbital effects or due to our hybrid having little enough disorder that $B_{xx}^c/B_{xy}^c > 1$.

When plotting the magneto-resistivities of [figure 7.2](#) on log scale, finite resistivity oscillations are found for $B_{\perp} < B_{c,\perp}$, in both ρ_{xx} and ρ_{xy} , see [figure 7.3](#). These oscillations and their dependence on B_{\perp} , T , and I_{DC} are the main research topic of this chapter.

Clear $B_{\perp} < B_{c,\perp}$ oscillations were not observed in the 4.2 V anodized Hall bar on device α , but a similar, though smaller, resistance increase between 1 and 3 T was observed.

With the amplitude of the oscillations being small and temperature dependent, measurement parameters had to be optimized. The frequency of the AC current was set to 13 and 21 Hz (one for each Hall bar). An AC amplitude of 1 nA, sourced through 1 G Ω , was found to give good signal-to-noise ratio without introducing heating. The sample itself was used as temperature sensor. The parameters for minimizing heating effects were found by optimizing $B_{c,\perp}$. Heating was also introduced by sweeping the magnet. Rather than lowering the ramping rate, a longer Lock-in time constant was found efficient in reducing the temperature of the sample during magnet field sweeps and simultaneously yielded

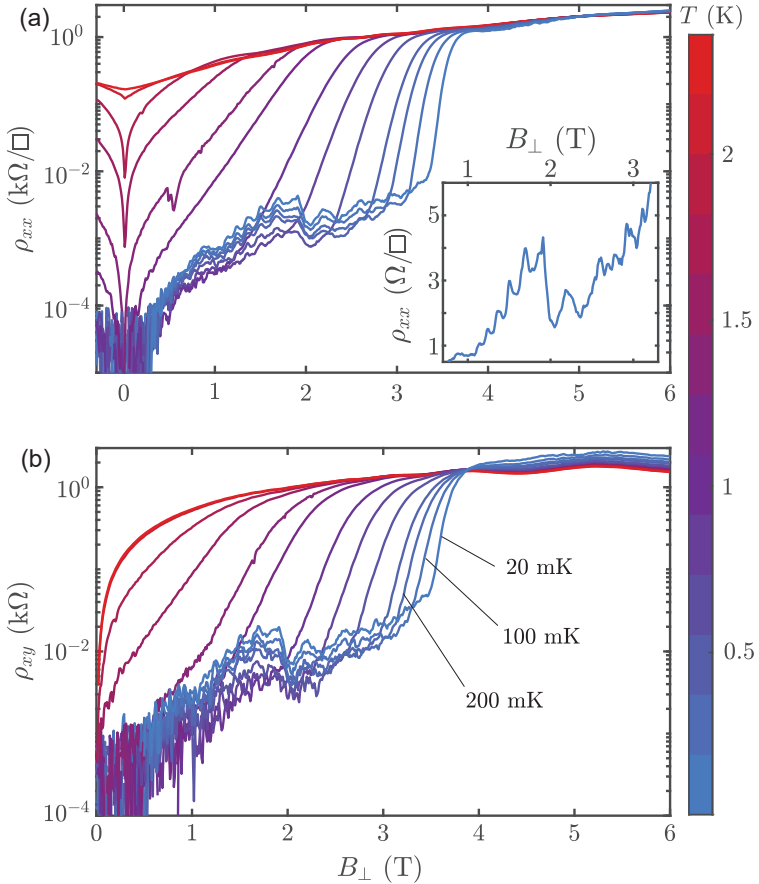


Figure 7.3: **Magneto-resistivity isotherms, log axis.** Same data as on [figure 7.2](#), both plotted on a log-scale to highlight the small but finite (a) longitudinal and (b) Hall resistivity for $B < B_{c,\perp}$. Small resistivity oscillations are visible for both measurements, highlighted by the inset of (a) showing a zoom of the longitudinal resistivity on a linear axis.

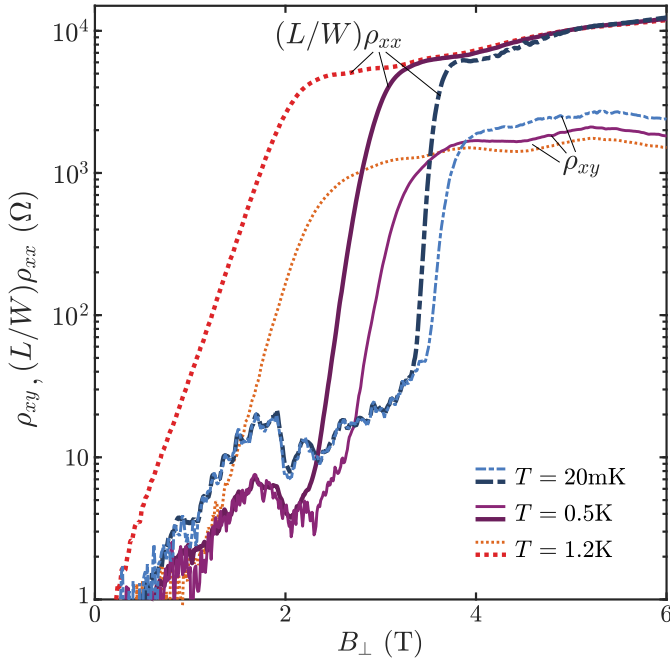


Figure 7.4: **Comparing $R_{xx}(B_{\perp})$ and $R_{xy}(B_{\perp})$.** Both resistances are plotted for three different temperatures, 20 mK, 500 mK, and 1.2 K.

better a signal-to-noise ratio. A long time-constant of 10 sec was applied for the field sweeps.

In [figure 7.3](#), the sub- $B_{c,\perp}$ Hall resistivity is larger than the corresponding longitudinal resistivity. The same observation is also true for [figure C.10](#). For $B_{\perp} < B_{c,\perp}$ the ratio ρ_{xy}/ρ_{xx} turns out to be 5, the aspect ratio of the bars. With $R_{xx} = (L/W)\rho_{xx}$ and $R_{xy} = \rho_{xy}$, we find that $R_{xx} = R_{xy}$ for $B < B_{c,\perp}$, which was observed on both bars, as displayed on [figure 7.4](#) and [figure C.11](#).

The $R_{xx} = R_{xy}$ equality holds true for a range of temperatures, until T brings $B_{c,\perp}$ to very low fields. We haven't figured out the physics behind the equality yet. The relation was first realized a while after the experiment ended. A couple tests, yet to be done, that could shed light

on the physics are:

Measure other bars with other aspect ratios.

If the $R_{xx} = R_{xy}$ equality holds true for different aspect ratios, it would indicate a lack of dependence on the bulk. Another devices could be made were multiple probes contact the region exposed to anodic oxidation. Here it would be interesting to check if R_{xx} of the oscillations is constant on a given Hall bar, independent of the distance between measurement probes.

Measure the various voltage drops.

Measurements of V_{xx} on both sides of the Hall bar, both V_{xy} , the diagonal voltage V_D , and the off-diagonal voltage $V_{\overline{D}}$ could be compared with Landauer-Bütikker analysis [16]. [Appendix D](#) displays an analysis based on the single $V_{xx} = V_{xy}$ dataset we have, assuming that it is true for all combinations of V_{xx} and V_{xy} . The analysis suggests that V_D and/or $V_{\overline{D}}$ would be zero, depending on the field-direction. It would be interesting to measure all voltage drops in both field directions to test this prediction.

7.2 TEMPERATURE AND $1/B_{\perp}$ DEPENDENCE

[Figure 7.4](#) clearly shows resistances at intermediate fields having an inverse temperature dependence. To highlight this observation, [figure 7.5](#) displays longitudinal resistivity as a function of temperature for a selection of B_{\perp} . Between 0.5 and 3 T, ρ_{xx} decreases with increasing T , until $T_c(B)$ is reached. Increased resistance from decreased temperature is usually known for energy-gapped materials such as insulators and undoped semiconductors, suggesting the observed resistance having a semiconductor-nature from the 2DEG under the oxidized aluminum.

Besides the overall resistance, the resistance oscillation amplitudes also decrease when increasing temperature. This is highlighted in [figure 7.6](#) by extracting the residual of the longitudinal resistivity. The residuals

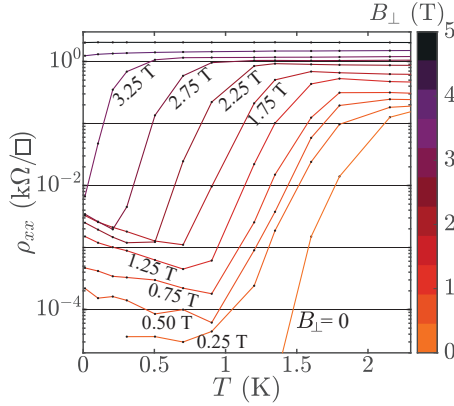


Figure 7.5: **Inverse temperature dependence.** Data from figure 7.3 plotted as $\rho(T)$ for various constant B_{\perp} . At low T and intermediate B_{\perp} , ρ_{xx} has an inverse temperature dependence.

were extracted by fitting a 2nd order polynomial between 1.1 and 1.75 T. Base temperature example is displayed on figure 7.6(a).

In figure 7.6(b) we show the extract residuals for several temperatures. The oscillation periods seem to increase with B_{\perp} . When as $1/B_{\perp}$ in figure 7.6(c) the residuals look periodic. Verification of a periodicity is done with fast Fourier transform (FFT), using a Hamming window. The result is displayed in figure 7.6(d). The $1/B_{\perp}$ frequency is ~ 14 T.

The observed oscillations resemble Shubnikov-de Haas oscillations (SdHO), reviewed in subsection 2.2.3. They are $1/B_{\perp}$ periodic and their amplitudes decrease with increasing temperature. Assuming that they are SdHO, quasiparticle properties can be extracted from the FFT presented in figure 7.6(d). The FFT frequency (in tesla) can be plugged into equation 2.34 and results in an electron density

$$n_e = 2 \frac{e}{h} \cdot 14 \text{ T} = 6.8 \cdot 10^{11} \text{ cm}^{-2}, \quad (7.4)$$

lower than both the zero field Hall slope density $n_e = 1.15 \cdot 10^{12} \text{ cm}^{-2}$ and the $T > T_c$ oscillation density $n_e \sim 7.5 \cdot 10^{11} \text{ cm}^{-2}$. For the latter, the

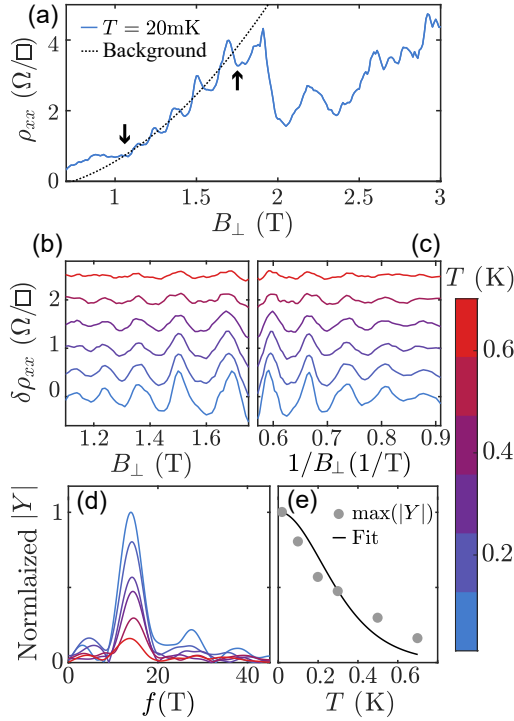


Figure 7.6: $1/B_{\perp}$ dependence of sub- $B_{c,\perp}$ ρ_{xx} oscillations. **(a)** Extraction of magnetoresistivity background, here shown at base temperature scan. For all temperatures, the extraction was done with a 2nd order polynomial between 1.1 and 1.75 T, marked by arrows. The resulting residuals at different temperatures are plotted as a function of **(b)** B_{\perp} and **(c)** $1/B_{\perp}$ offset by $0.5 \Omega/\square$. The colorbar is marking temperatures for all subfigures. **(d)** The $1/B_{\perp}$ periods are extracted with FFT showing a frequency $f \sim 14$ T for all temperatures. Axis is normalized to the base temperature peak height. **(e)** Peak height as a function of temperature is fitted using [equation 2.36](#) to extract an effective mass $m^* = 0.77 \pm 0.22m_e$.

difference is small, and could possibly be explained by a temperature dependent density.

With the temperature dependence of SdHO, effective mass of the carriers can be extracted using [equation 2.36](#). Rather than using the height of a single peak, the FFT amplitudes can be used. The fit, displayed in [figure 7.6\(e\)](#), extracts an effective mass $m^* = 0.77 \pm 0.22m_e$. For comparison, the effective mass of bulk InAs carriers is $0.023 m_e$, see [table 2](#).

Such a high effective mass can, to our knowledge, not be a property of the 2DEG alone but must be due to having the disordered Al in close proximity. With both SdHO and superconductivity being quenched by temperature, a correlation of the two could have a stronger temperature dependence than regular SdHO, which would result in an overestimate of the effective mass.

7.3 DC CURRENT DEPENDENCE

Another way to probe the physics of the sub- $B_{c,\perp}$ oscillations, is to measure the I_{DC} dependence of $\tilde{\rho}_{xx}$ and $\tilde{\rho}_{xy}$, defined as

$$\tilde{\rho}_{xx} = (W/L) \left. \frac{dV_{xx}}{dI_{AC}} \right|_{I_{DC}=0}, \quad \tilde{\rho}_{xy} = \left. \frac{dV_{xy}}{dI_{AC}} \right|_{I_{DC}=0}.$$

This study, done at base temperature (20 mK), is displayed in [figure 7.7](#). Data was taken by sweeping I_{DC} and stepping B_{\perp} .

Finite DC current bias suppresses sub $B_{c,\perp}$ oscillations, both in $\tilde{\rho}_{xx}$ and $\tilde{\rho}_{xy}$, similar to when increasing the temperature. Decrease of oscillation amplitude with I_{DC} is another feature, known from SdHO [[138](#)].

The turn-on of higher resistances happens earlier in I_{DC} and B_{\perp} for $\tilde{\rho}_{xx}$, [figure 7.7\(a\)](#), than for $\tilde{\rho}_{xy}$, [figure 7.7\(b\)](#). The extended red region in $\tilde{\rho}_{xx}$ is interpreted as an onset of vortex flow which, as mentioned in [subsection 2.3.6](#), is expected to only give a longitudinal voltage drop (\hat{x} direction) due to the Lorentz force accelerating the vortices in the \hat{y} direction.

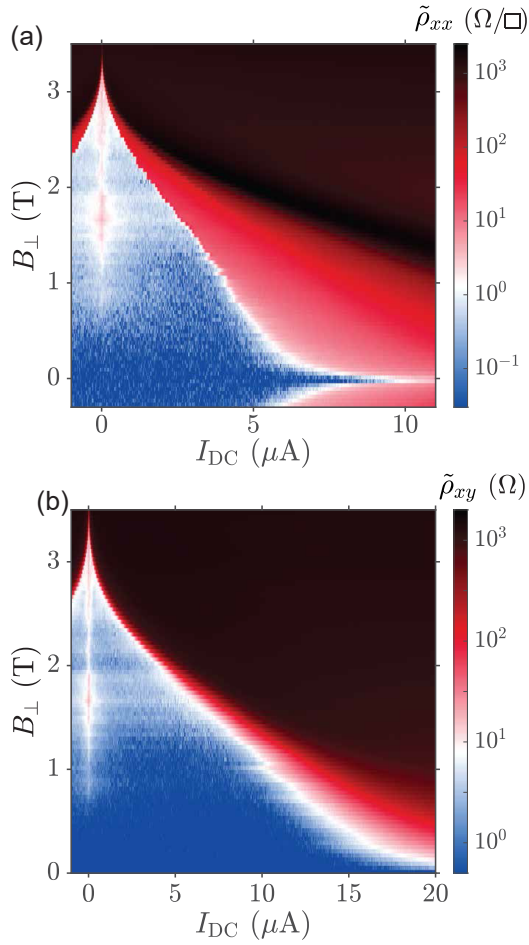


Figure 7.7: I_{DC} dependence of ρ_{xx} and ρ_{xy} , measured at $T = 20$ mK. (a) Longitudinal and (b) Hall resistivity as a function of DC current and perpendicular field. Notice that $I_{DC} < 0$ is included and that the I_{DC} range of the two plots is not identical.

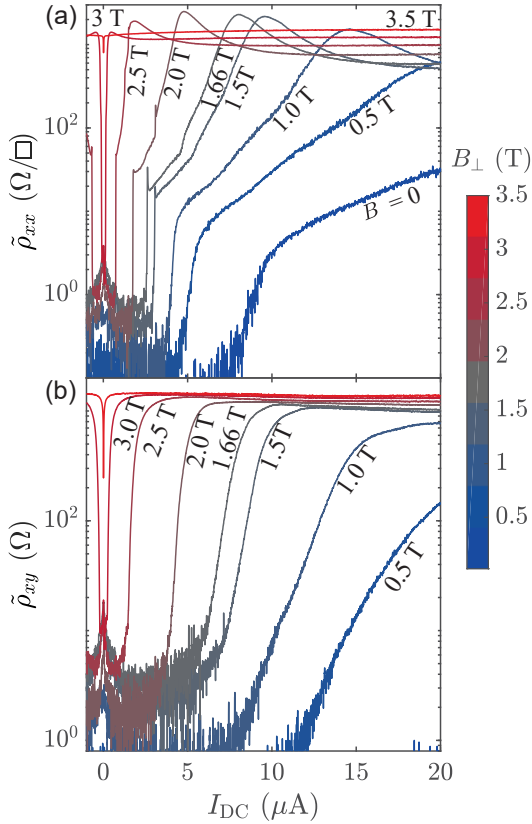


Figure 7.8: **Line cuts of I_{DC} dependence of $\tilde{\rho}_{xx}$ and $\tilde{\rho}_{xy}$.** (a) Longitudinal and (b) Hall resistivity as a function of DC current for various perpendicular fields. Data extracted from [figure 7.7](#).

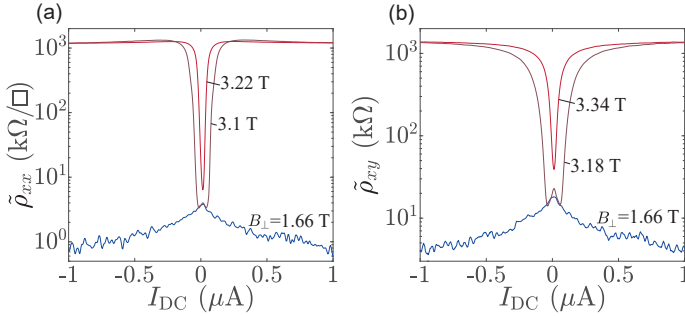


Figure 7.9: **Line cuts of small I_{DC} dependence of $\tilde{\rho}_{xx}$ and $\tilde{\rho}_{xy}$.** (a) Longitudinal and (b) Hall resistivity as a function of DC current for selected perpendicular fields. Data extracted from figure 7.7.

Lines cuts from figure 7.7, displayed on figure 7.8, are useful for extracting the resistance slopes around $B_{c,\perp}$. The abrupt onset of $\tilde{\rho}_{xx}$ suggests a vortex creep where the current is just enough for vortices to jump between pinning sites. The presence of pinning is not unexpected if the oxidized Al has a similar morphology as seen on figure 4.2. This interpretation is backed by the lack of sudden jumps of $\tilde{\rho}_{xy}$, see figure 7.8(b).

At $B_{\perp} > 3.2$ T the critical current becomes low enough to increase the resistance at $I_{DC} = 0$, turning the SdHO peak into a dip in resistivity, both for longitudinal and Hall, displayed on figure 7.9.

7.4 CONCLUSION AND WORK TO BE DONE

In this chapter a study was conducted on bars defined in epitaxial Al on InAs 2DEG exposed to $V_{AO} = 4.2$ V. This produces a novel material system of an disordered superconductor with transparent coupling to an underlying 2DEG.

We observe small ($< 20 \Omega$) resistance oscillations appearing at finite B_{\perp} below $B_{c,\perp}$, both in longitudinal and Hall resistance. A few important observations regarding the oscillations are made, suggesting that they could be related to Shubnikov-de Haas physics from the 2DEG:

- The oscillations are $1/B_{\perp}$ periodic.

- Assuming they are SdHO, a density of $6.6 \cdot 10^{11} \text{ cm}^{-2}$ is extracted, which could be the density of the underlying 2DEG.
- The oscillation amplitudes decrease with increasing temperature or DC current.

Other $1/B_{\perp}$ periodic oscillations were observed at multiple tesla for $T > T_c$. Their period is comparable to a density of $n_e = 7.5 \cdot 10^{11} \text{ cm}^{-2}$. The density is close to but larger than that extract from the small oscillations. This additional density could maybe be due to the higher temperature.

An even higher density $n_e = 1.15 \cdot 10^{12} \text{ cm}^{-2}$ was extracted from the zero field Hall slope at $T > T_c$. Here, both the aluminum and e-e-interaction could cause the higher density.

Current dependence was extracted from 2D sweeps of I_{DC} and B_{\perp} , measuring both $\tilde{\rho}_{xx}$ and $\tilde{\rho}_{xy}$. Resistance of the $B_{\perp} < B_{c,\perp}$ oscillations are decreased by application of a DC current. The data suggests that vortices are pinned at low currents, but starts creeping after a few μA , depending on B_{\perp} .

The following two observations, are currently not fully understood:

- The above mentioned Shubnikov-de Haas-like oscillations were observed in both longitudinal and Hall resistivities. Moreover, when plotted as resistances, the relation $R_{xx} = R_{xy}$ is true as long as the oscillations are present, which is from $\sim 0.5 \text{ T}$ until $B_{c,\perp}$.
- From the temperature dependence of the oscillation amplitudes, an effective mass $m^* = 0.77 \pm 0.22m_e$ is extracted.

Here is a list of things we suggest to be studied to shed light on the underlying physics of the above-mentioned observations.

- Diagonal and off-diagonal voltage drops should be measured on the bar since Landauer-Bütikker analysis, see [Appendix D](#), predicts one of them being 0, depending on the sign of B_{\perp} . Prediction was found by applying $R_{xx} = R_{xy}$.

- The bars measured had an aspect ratio of 1 : 5. Observing $R_{xx} = R_{xy}$ for other aspect ratios would indicate the measured resistances having a lack of dependence on the bulk.
- To extract the effective mass of the 2DEG alone, measurements of SdHO temperature dependence should be done for an etched Hall bar and a Hall bar with fully oxidized aluminum. Those data would be useful in understanding the $m^* = 0.77 \pm 0.22m_e$ observation for the studied bar.

IDEAS FOR FUTURE PROJECTS

This thesis has introduced anodic oxidation as a novel way of processing epitaxially grown Al on shallow InAs 2DEG heterostructures, see [subsection 3.3.2](#). Under the right conditions the method can result in improved electrical transport performances of the superconductor and the 2DEG. [Chapter 5](#) reports significant increases in $B_{c,\parallel}$ and $B_{c,\perp}$ from a partial oxidation and Hall bar mobility peak can be increased by at least a factor 2 through semiconductor surface passivation from a fully oxidized aluminum. [Chapter 6](#) presented results on obtaining high lateral resolution with AO using a metal mask defined by electron beam lithography. Though high resolution was obtained, that recipe led to unfavorable 2DEG properties such as low carrier mobility and noisy spectroscopy. With those results in mind, this final chapter will elaborate on ideas on how to further improve the semiconductor and superconductor properties of these hybrids, to enable the next generation of devices and experiments.

The ideas are separated into four sections. First, unrelated to oxidation, [section 8.1](#) elaborates on thoughts on changes to the III/V heterostructure stack that could be advantageous in the hunt for exotic physics like Majorana modes, recall [subsection 2.4.5](#). [Section 8.2](#), elaborates the problem of a time-dependent AO process and thoughts on how to solve

it. Our ability of making high quality superconductor/semiconductor junctions with AO can be affected by the time-dependence. [Section 8.3](#) goes through ideas for masking that would work, even with a time-dependence. Lastly, [section 8.4](#) introduces ideas on how to obtain selective areas of fully oxidized Al, without the use of electrochemical anodic oxidation.

8.1 III/V GROWTH IMPROVEMENTS WITH SB

[Subsection 3.1.3](#) mentioned the use of GaSb substrates enabling growth of high quality InAs quantum wells due to the close lattice match of GaSb and InAs. Another use of Sb is to add it to the quantum well, forming a InAsSb 2DEG. The ternary is interesting due to its strong spin-orbit coupling. It is stronger than that of both InAs and InSb¹ and therefore would be useful for realizing Majorana modes, see [subsection 2.4.5](#). Besides controlling the lattice constant, the As/Sb ratio also changes the size of the g-factor as well as the Fermi-level pinning.

[Subsection 3.1.3](#) also mentioned the antimonides being prone to oxidation compared with the arsenides. Besides avoiding pure AlSb (use AlGaSb instead), a good habit is to arrange fab such that ALD is done immediately after the mesa etch. This limits the amount of exposure the antimonides have to *ex-situ* environments before being passivated by ALD.

8.2 AO TIME-DEPENDENCE

Besides the improvements to our AO process mentioned in [subsection 3.3.3](#), its time-dependence could be looked into. Ideally, the oxidation depth of barrier-type films is only dependent on one parameter: the anodization voltage V_{AO} . With the GaAs based material, see [section 4.1](#), we were able to confirm that the oxidation depth, with the setup elaborated

¹ Mentioned in this APS talk: <https://ui.adsabs.harvard.edu/abs/2018APS.MARA07009P/abstract>

in [subsection 3.3.2](#), has an unintended time-dependence as well. This was realized at the end of this study.

To verify a time-dependent oxidation, a test was conducted on Al grown epitaxially on GaAs. With electron beam lithography a confined region was defined on a newly-cleaved chip. Two-terminal resistance was measured at room temperature with a DMM both prior to and after AO. Electrical connection was established through aluminum bonds to a glass slide with multiple leads, see [figure 3.12\(c\)](#). Before AO, a low resistance $R \sim 15 \Omega$ of the metallic Al was measured. AO was done as described in [subsection 3.3.2](#), but at a low voltage $V_{AO} = 3.0 \text{ V}$ and with the process running for 25 min. After AO, the resistance was measured, through the same bonds, to be $R > 1 \text{ M}\Omega$, indicating a full oxidation of the aluminum. A low V_{AO} (lower than any of the values used for experiments in this thesis) could with enough time fully oxidize the aluminum, thus indicating a time-dependence.

The time-dependent oxidation might have been accounted for by trying other pH values for the ammonium tartrate electrolyte or even by trying other electrolyte solutions. A material-related suspicion for the time-dependence is the grain boundaries, which might be oxidized more easily than the grains. Or maybe some grains oxidize faster than others. With enough time, maybe the oxidation could soak through the weak points and isolate the grains. This could be studied by comparing short AO exposures with large V_{AO} against long AO exposures with small V_{AO} .

Getting rid of the time-dependence would significantly increase the reproducibility of the AO process.

8.3 UPGRADING AO LITHOGRAPHY

Though enabling good lateral resolution for electrochemical AO, the Ti mask introduced in [chapter 6](#) had limitations, which we suspect to be related to the presence of Ti and/or TiOx. Two possible workarounds, yet untested, are presented in this section.

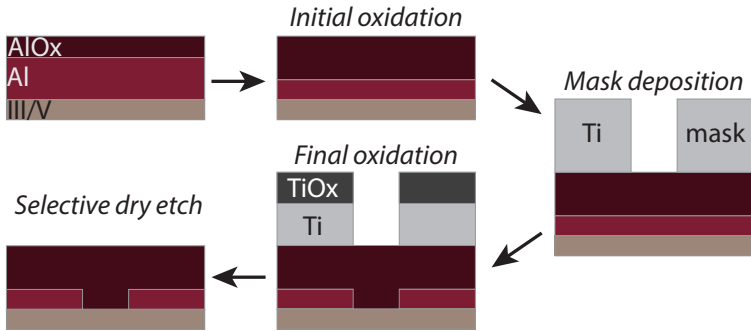


Figure 8.1: **Implementing Ti mask removal.** An initial oxidation determines the desired final thickness of metallic Al. Ti is evaporated in regions desired to be superconducting. A final oxidation is chosen to oxidize the exposed Al all the way through, without going into the semiconductor. A selective etch is implemented to remove the Ti mask.

8.3.1 Removing Ti mask selectively with dry etch

Karl Petersson recently mentioned² that a fluorine dry etch have great selectivity in attacking Ti/TiOx over Al/AlOx. Implementing this could allow for fabrication of devices with all the desired properties: Good lateral resolution, optimal mobility for the III/V and flexibility in choosing a desired Al thickness. This would be possible, even with a time-dependent AO process. The fabrication order is displayed in [figure 8.1](#).

First step would be to deposit alignment marks. Remember, refrain from using Au marks for AO fab as mentioned in [subsection 3.3.3](#). Ti/Al marks could be used instead. A global anodic oxidation determines an Al thickness. A Ti mask, > 5 nm thick³, should be evaporated in regions desired to be superconducting, to shield the Al from a second AO that oxidizes the exposed Al all the way down to the III/V. Lastly, a selective dry etch would be used to strip the Ti. The whole chip would still be covered with Al/AlOx, and is thus protected from the dry etch. Now, a

² Private communication

³ The thicker films are easier to lift off without debris.

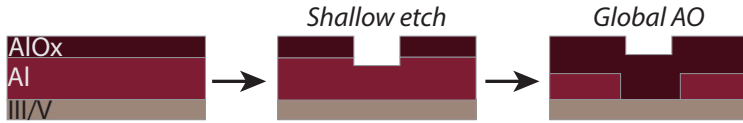


Figure 8.2: **Shallow etch masking AO.** A masked shallow etch followed by a global AO can also be used to pattern anodic oxidation.

mesa etch could be executed followed by ALD and lastly gate deposition. This process would also be compatible with Sb-based materials due to the mesa etch being executed just before ALD.

One possible addition to the recipe is a few sec HF wet etch dip after the dry etch, to remove any kind of surface damage/impurities done to AlOx from the dry etch. This might make the surface AlOx a cleaner dielectric with less charge noise.

8.3.2 *Shallow etch mask*

Another option for patterning AO is the use of a shallow wet or dry etch to turn the epitaxial Al into its own mask, displayed in [figure 8.2](#). As in [subsection 8.3.1](#), the figure shows the process steps in between alignment marks and mesa etch.

Thought should be put into the choice of etch depth and V_{AO} . One constraint is that AO of the etched regions should oxidize all remaining Al, but not attack the III/V. Thus the etch depth controls thickness of remaining metallic aluminum. A shallow etch requires a big V_{AO} , resulting in little metallic Al remaining. A deeper etch only allows a small V_{AO} , thus giving a thicker metallic Al.

8.4 OTHER TECHNIQUES APPLYING OXIDATION OF AL

Electrochemical anodic oxidation is not the only way to oxidize Al. This section introduces two other methods for oxidizing epitaxial Al; local anodic oxidation with AFM and growing Pb on top Al *in-situ*, before breaking vacuum.

8.4.1 Local anodic oxidation using AFM

Anodic oxidation with an atomic force microscope (AFM) is a well known and established process [139, 140]. A moist atmosphere is used to trap a water droplet in between the substrate and a conductive AFM tip. By sourcing a voltage difference between tip and substrate, oxygen ions from the water can be used for anodic oxidation. By the right choice of parameters, a sub-100 nm oxidation line can be formed. To our knowledge, no published study extensively studied how to control the oxidation depth. As we saw in figure 5.3, an oxidation beyond the Al and into the semiconductor decreases the mobility of the III/V. Thus, a study is needed to find the set of parameters that allow for a consistent and controlled oxidation depth, while maintaining good lithographic resolution. Some of these parameters are: V_{AO} , humidity, tip quality, tip vibration, and distance between tip and substrate.

8.4.2 Growing Pb on top of Al

This final idea combines the two following results:

- Passivation of III/V through complete Al oxidation
- Enhancing the Al gap, Δ_{Al} , by proximity effect of a second superconductor with a larger gap [108].

Instead of *ex-situ* deposition of the second superconductor, as in ref [108], it should be grown epitaxially *in-situ* on top of the Al, ensuring a good proximity effect between the two. This already puts limitations on the choice of superconductor. Adding too much heat during the growth increases the risk of the Al bulking up, thus it must be possible to grow the second superconductor epitaxially at low temperatures. Another constraint is the existence of a process that selectively etches the superconductor over Al. One great candidate is Pb.

Pb is a fragile material, but with good superconducting properties, see figure A.1. Recently Pb was grown with epitaxial match on InAs vapor-liquid-solid nanowires where it induced a large gap $\Delta^* = 1.25$ meV that survived large magnetic fields $B_{c||} > 8.5$ T [92]. The Pb could be

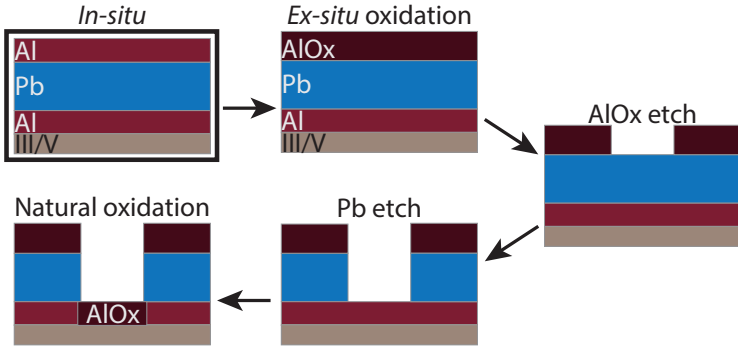


Figure 8.3: **Process for Pb hybrid.** Instead of pure epitaxial Al, an Al/Pb/Al stack is grown. The aluminum layers are thin enough to oxidize fully by themselves. Once taken out of vacuum, the surface Al oxidizes naturally, passivating the Pb. To make a junction, first the surface alumina is etched and then the Pb is etched selectively without stripping the bottom Al. Once being exposed, the bottom Al now oxidizes and passivates the III/V.

etched by H_2O , making it promising in terms of etch selectivity with Al, but also worrying in terms of it being vulnerable. Therefore, a thin Al layer could be grown on top of Pb for passivation. This is displayed in [figure 8.3](#) together with the proposed fab steps.

The proposed superconducting stack, to be put on top of a shallow InAs 2DEG heterostructure is Al/Pb/Al, with both Al being $\sim 2 - 3$ nm. The right thickness is not determined yet, but it should be a thickness that allows the Al layers to oxidize fully by themselves when exposed to atmosphere. Once the wafer is taken out of vacuum, the surface Al will oxidize, creating an alumina passivation layer on the Pb.

To define junctions, the alumina and then the Pb has to be etched. The post etch rinse for the alumina etch should not be H_2O , but rather IPA, which won't etch the Pb. Therefore a developer for optical resist (like MF 321) is suggested for alumina etching. A couple options are available for etching the Pb selectively:

- H₂O can be used, but the etch rate can only be controlled by temperature. Mixing water with IPA creates a E-beam resist developer, which would attack our resist mask. It might still work if the patterned surface alumina serves as an etch mask.
- Nitric acid etches Pb⁴ and promotes Al oxidation [123], making it an interesting candidate. A downside is that pure Nitric acid strongly attacks E-beam resists⁵, and diluting it with IPA can produce explosives [141]. Ideally, the etched surface alumina is sufficient as a mask for the Pb etch.
- Acetic acid etches Pb as well⁴. Instead of oxidizing Al, it forms aluminum acetate that prevents further corrosion⁶. Whether aluminum acetate would create electrostatic noise is, to our knowledge, yet to be determined. Pure phosphoric acid attacks E-beam resists⁵ as well, but can safely be diluted with IPA. The dilution also allows for good control of the etch rate.

The order of the different fab steps becomes important when incorporating Pb. We don't yet know how fragile the exposed Pb edges will be. Maybe, ALD should be done right after the Pb etch. On the other hand, we should keep in mind that the mesa etch consists mostly of water. Therefore, it could be preferable to do the Pb etch before the mesa etch. The device designs should ensure that Pb edges are significantly far away from the mesa edges and thus fully covered by resist during the mesa etch step.

Maybe the solution is to have two separate Pb etches. An outer one, prior to the mesa etch, and then an inner one for small features followed by ALD.

4 <https://database.metallographic.com/pace-etchant.php>

5 <https://www.industrial-spec.com/resources/acrylic-aka-pmma-chemical-compatibility-chart>

6 <https://pubchem.ncbi.nlm.nih.gov/compound/Acetic-acid>

Heterostructures of shallow InAs 2DEGs capped with epitaxially grown Al have enabled many publications within a few years and still leave much work to be done. Especially when implementing new processes and/or material combinations. Those results could then be transferred to other hybrid material platforms such as vapor-liquid-solid nanowires and selective-area-growth.

Appendices

A

SUPERCONDUCTING PROPERTIES OF BULK ELEMENTS

For comparison, a table of critical temperature and critical magnetic field for bulk elemental superconductors is shown in [figure A.1](#). Keep in mind that larger critical temperatures and fields are found in some alloys and by changing the shape, morphology and/or disorder of the elemental superconductors.

FABRICATION RECIPES

This chapter includes all the recipes used for fabrication of devices presented in the this thesis. The recipes are not ordered chronologically. Instead, each section should be read as a separate part and the complete recipe for a given chip will be a collection of these parts. Here is an overview of the different recipes presented:

B.1	Mixing ammonium tartrate for AO	142
B.2	Initial clean	143
B.3	Evaporating Ti/Au alignment marks	143
B.4	Mesa etch	144
B.5	Aluminum etch	145
B.6	Ti mask for anodic oxidation	147
B.7	E-Beam resist mask for anodic oxidation	147
B.8	Anodic oxidation	148
B.9	Etch of anodized Al	149
B.10	Hafnia deposition with ALD	149
B.11	Inner gates deposition	150
B.12	Outer gates deposition	151

Before going through all the recipes, we will elaborate one crucial part for most of them. To obtain reproducible high resolution features with electron beam lithography, *proximity effect correction* (PEC) needs to be taken into use. Rather than exposing all features with a uniform exposure time, PEC takes substrate-dependent back-scattering of electrons into account, ensuring that PEC localized features like edges and corners won't be underexposed compared to the bulk. To do PEC, we implement the program *Beamer*¹. With a perfect PEC, a single dose is sufficient for all features. The PEC in Beamer is developed for fab on silicon, where the back-scattering is different from that of III/V. Even when we type in the right material parameters, we still have to make small corrections to the dose depending on the geometry of the exposed pattern. Another useful parameter to change is the Clearing/Contrast setting in the PEC. With 100% contrast, features will be sharp, but the bulk of big exposed regions has a tendency of getting underexposed. With 100% clearing, the bulk will not be underexposed at the cost of losing feature sharpness.

B.1 MIXING AMMONIUM TARTRATE FOR AO

Making tartaric acid:

Take bottle/jar with a volume ≥ 2 L

Add a magnet for stirring

Add 1455 g MQ water

Add 45 g Tartaric acid powder

Stir until powder is fully dissolved.

pH buffering with NH_4OH :

Add NH_4OH to increase pH to the desired value. Ref. [119] suggests a pH of 5 to 5.5 to achieve a barrier type alumina film.

The pH increase is not linear, so add NH_4OH carefully in small amounts and measure pH in between each addition. At least 40 mL of NH_4OH (30% < konc. < 33%) was used.

¹ <https://www.genisys-gmbh.com/beamer.html>

B.2 INITIAL CLEAN

Sonication in dioxolane for 5 min @ 80 kHz, 100% pwr.
Acetone Squirt, IPA squirt, Blow dry with nitrogen gun.

B.3 EVAPORATING TI/AU ALIGNMENT MARKS**Resist:**

EL6 @ 4000 RPM, 45 sec
185 degC for 3 min
A4 @ 4000 RPM, 45 sec
185 degC for 3 min

Exposure:

- Fine features: 500 pA, 150 μm field, 60k dots, dose of 0.08 $\mu\text{s}/\text{dot}$, area dose: 640 $\mu\text{C}/\text{cm}^2$, InP PEC, Optimal contrast.
Change beam with a 10 min wait time.
- Large features: 20 nA, 600 μm field, 20k dots, dose of 0.315 $\mu\text{s}/\text{dot}$, area dose: 700 $\mu\text{C}/\text{cm}^2$, InP PEC, 70 % Optimal contrast.

Develop:

60 sec MIBK:IPA, then 20 sec IPA, blowdry.
Ash 2 min

Evaporation:

No stage tilt or rotation

10 nm Ti
100 nm Au

Liftoff:

Couple hours in dioxolane, acetone squirt, IPA squirt, blow dry

B.4 MESA ETCH**Resist:**

A4 @ 4000 RPM, 45 sec, 185 degC for 3 min

Exposure:

- Fine features: 500 pA, 300 μm field, 60k dots, dose of 0.32 $\mu\text{s}/\text{dot}$, area dose: 640 $\mu\text{C}/\text{cm}^2$ w. InP PEC, 100 % Optimal contrast

Change beam with a 10 min wait time

- Large features: 20 nA, 600 μm field, 20k dots, dose of 0.2925 $\mu\text{s}/\text{dot}$, area dose: 650 $\mu\text{C}/\text{cm}^2$ w. InP PEC, 80 % Uniform clearing

Develop:

30 sec MIBK:IPA, then 15 sec IPA blowdry.

Ash 1 min

Post Bake: 2:00 min @ 115 degC

Al-etch:

Prepare 3 small beakers with equal amounts of liquid: two with Transene Al etch D, the third with MQ water. Put all of them in a hot bath. Fill up the water bath until its level matches the surface level of the beakers' liquid. Set the water bath temperature to 52-53 degC and don't put on a lid. Once saturated, this results in a Transene temperature around 50 degC. The optimal set-point might vary between different setups. Take a medium sized beaker and fill it with MQ as well. One Transene beaker is used for etching, the other is used for temperature measurement with a thermometer. Confirm Transene temperature before etching. Etching procedure is (in all steps swirl rigorously):

- (a): 6s in Al Etch D.
- (b): 20s in MQ in hotbath
- (c): 40s in MQ outside hotbath.
- Blowdry²

² It is good practice to blowdry the chip, then blow dry the tweezers and then blow dry the chip again. With wet tweezers, droplets will always be blown down on the chip.

The Transene etch time of 6 sec has been sufficient to clear all exposed Al. For a growth with thicker Al, >6 sec might be necessary.

III/V-etch:

Using standard mesa etch solution:

$\text{H}_2\text{O} : \text{C}_6\text{H}_8\text{O}_7 : \text{H}_3\text{PO}_4 : \text{H}_2\text{O}_2$ (220:55:3:3 ratio). Use wide beaker with magnetic stirrer. First, add water and start stirring. Add citric acid and add H_3PO_4 . H_2O_2 is added just before starting the Al etching step, or a couple minutes before doing the etch.

Etch for 9:30 mins

Immediately after etching, wash in MQ water for 30 sec with rigorous swirling followed by nitrogen blow dry.

Strip: >5 min in dioxalene, acetone squirt, IPA squirt, blow dry.

B.5 ALUMINUM ETCH**Resist:**

A4 @ 4000 RPM, 45 sec, 185 degC for 3 min

Exposure:

- Fine features: 100 pA, 150 μm field, 60k dots, dose of 0.38 $\mu\text{s}/\text{dot}$, area dose: 608 $\mu\text{C}/\text{cm}^2$ w. InP PEC, Optimal contrast

Change beam with a 10 min wait time

- Large features: 20 nA, 600 μm field, 20k dots, dose of 0.3 $\mu\text{s}/\text{dot}$, area dose: 666.667 $\mu\text{C}/\text{cm}^2$ w. InP PEC, Uniform clearing

Develop:

30 sec MIBK:IPA, then 20 sec IPA, blowdry.

Ash 45 sec

Post Bake: 2 min @ 115degC

Al-etch:

Prepare 3 small beakers with equal amounts of liquid: two with Transene Al etch D, the third with MQ water. Put all of them in a hot bath. Fill up the water bath until its level matches the surface level of the beakers' liquid. Set the water bath temperature to 52-53 degC and don't put on a lid. Once saturated, this results in a Transene temperature around 50 degC. The optimal set-point might vary between different setups. Take a medium sized beaker and fill it with MQ as well. One Transene beaker is used for etching, the other is used for temperature measurement with a thermometer. Confirm Transene temperature before etching. Etching procedure (in all steps swirl rigorously.):

- (a): X s dip in Al Etch D.
- (b): 20 s in MQ in hotbath
- (c): 40 s in MQ outside hotbath.
- Blowdry

The exact length of X depends on a couple factors. The exact etch time-dependence on your Al thickness and how new the Transene solution is. A change of 0.5-1 s is significant here. Newer solutions seems to etch faster. Also, different users might count the etch time differently. The right etch time for a given user can be found by measuring the resulting features in SEM or AFM and adjust the etch time accordingly. This recipe should be able to result a etch run less than 10 nm, compared to designed features. A good starting point is 5 sec.

Stripping resist:

>15 min dioxalene, acetone squirt, IPA dip, blow dry.

B.6 TI MASK FOR ANODIC OXIDATION**Resist:**

A2 @ 4000 RPM, 45 sec, 185 degC for 3 min

Exposure:

- Fine features: 500 pA, 150 μm field, 60k dots, dose of 0.078 $\mu\text{s}/\text{dot}$, area dose: 620 $\mu\text{C}/\text{cm}^2$ w. InP PEC, optimal contrast.

Change beam with a 10 min wait time

- Large features: 20 nA, 600 μm field, 20k dots, dose of 0.3 $\mu\text{s}/\text{dot}$, area dose: 666.667 $\mu\text{C}/\text{cm}^2$ without PEC

Develop:

30 sec MIBK:IPA, then 10 sec IPA blowdry

Ash 45 sec

Evaporation:

No stage tilt or rotation

3 nm Ti, rate of 1.2 $\text{\AA}/\text{s}$

Liftoff:

Sonication in Dioxolane for 5 min @ 80 kHz, 100% pwr.

Optical inspection in IPA to verify success of liftoff. Use more sonication if needed.

Acetone squirt, IPA squirt and blow dry.

B.7 E-BEAM RESIST MASK FOR ANODIC OXIDATION**Resist:**

EL9 @ 4000 RPM, 45 sec, 185 degC for 3 min

EL9 @ 4000 RPM, 45 sec, 185 degC for 3 min

Exposure:

Large features: 20 nA, 600 mu field, 20k dots, dose of 0.1575 us/dot, area dose: 350 muC/cm² w. InP PEC

Develop:

60 sec MIBK:IPA, then 20 sec IPA blowdry.

Ash 1 min

B.8 ANODIC OXIDATION**Sticking chip on glass slide:**

Place droplet of A6 resist on glass slide and place the chip. Remember the importance of orientation, recall [figure 3.13](#).

Heat glass slide @ 115 degC for 3 min to harden the resist

Bonding from Ti/Au on glass slide to exposed regions on the chip

Anodic Oxidation at x.x V:

- Put in Tartaric Acid
- Put on alligators
- Ramp up to x.x V with 0.1 V/sec
- Let it sit at x.x V for 5 min
- Ramp down with 0.1 V/sec
- Unhook alligators
- Put in MQ

Remove chip from glass and strip resist:

Few minutes in dioxalene, acetone squirt, IPA squirt, blow dry

Sometimes, small residues, visible with optical microscope are left after AO. These can be washed away in MQ water.

B.9 ETCH OF ANODIZED AL**Resist:**

EL9 @ 4000 RPM, 45 sec, 185 degC for 3 min

Exposure:

Large features: 20 nA, 600 μm field, 20k dots, dose of 0.1 $\mu\text{s}/\text{dot}$, area dose: 200 $\mu\text{C}/\text{cm}^2$ w. GaAs³ PEC, 100 % Uniform clearing

Develop:

40 sec MIBK:IPA, then 20 sec IPA blowdry.

Ash 2 min

Reflow: 2 min @ 115 degC

MF 321 etch:

Put in 15 mL MF 321 for 5 min

Wash 30 sec in MQ

Strip Resist:

Dioxolane for ~10 min, acetone squirt, IPA squirt, blow dry

B.10 HAFNIA DEPOSITION WITH ALD**Baking**

After loading the chip, pump for 10 hours with stages heated to 95 degC.

Growing Hafnia

Set stage temperatures to 90 degC.

Stabilize only the inner heater.

The following sequence is run 120 times:

³ Or InP, depending on substrate. Remember to also change the area dose according to the substrate

- Hf pulse, 0.5 s
- wait 180 sec
- H₂O pulse, 0.02 s
- wait 180 sec

The 120 rounds will deposit ~14 nm of hafnia.

B.11 INNER GATES DEPOSITION

Resist:

A4 @ 4000 RPM, 45 sec, 185 degC for 3 min

Exposure:

Fine features: 100 pA, 150 μ m field, 60k dots, dose of 0.38 μ s/dot, area dose: 608 μ C/cm², InP PEC, Optimal contrast

Develop:

30 sec MIBK:IPA, then 15 sec IPA and blowdry.

Ash 1 min

Evaporation:

No stage tilt or rotation

3 nm Ti

20 nm Au

Liftoff:

Leave in Dioxolane 1/2 hour or more

Acetone squirt, IPA squirt and blow dry

B.12 OUTER GATES DEPOSITION

Resist:

EL9 @ 4000 RPM, 45 sec, 185 degC for 3 min

EL9 @ 4000 RPM, 45 sec, 185 degC for 3 min

A4 @ 4000 RPM, 45 sec, 185 degC for 3 min

Exposure:

- Fine features: 500 pA, 300 μm field, 60k dots, dose of 0.32 $\mu\text{s}/\text{dot}$, area dose: 640 $\mu\text{C}/\text{cm}^2$, w. InP PEC 60/40 Contrast/Clearing.

Change beam with a 10 min sec wait time.

- Large features: 20 nA, 600 μm field, 20k dots, dose of 0.315 $\mu\text{s}/\text{dot}$, area dose: $\sim 700 \mu\text{C}/\text{cm}^2$, w. InP PEC, 30/70 Contrast/Clearing.

- Gate bonding squares: 20 nA, 600 μm field, 20k dots, dose of 0.315 $\mu\text{s}/\text{dot}$, area dose: $\sim 700 \mu\text{C}/\text{cm}^2$, without PEC

Develop:

40 sec MIBK:IPA, then 20 sec IPA and blowdry.

Ash 1 min.

Evaporation:

Stage rotation with ~ 1 revolution pr 2 sec.

10 nm Ti, 5 deg stage tilt, rate $< 1 \text{ \AA}/\text{s}$

50 nm Au, 5 deg stage tilt, rate $\sim 1.5 \text{ \AA}/\text{s}$

250 nm Au, 0 deg stage tilt, rate $\sim 1.5 \text{ \AA}/\text{s}$

50 nm Au, 10 deg stage tilt, rate $\sim 1.5 \text{ \AA}/\text{s}$

Liftoff:

Scratch chip on the side to help dioxolane get under the Ti/Au.

Leave in dioxolane for an hour or more.

Acetone squirt and hard IPA squirt.

Check under microscope while still in IPA.

Spray IPA until excess Au is cleared.

Blow dry.

ADDITIONAL DATA

This chapter includes data that was mentioned, but not shown, in various main text chapters.

c.1	$R(B, T)$ of Al on GaAs	154
c.2	$R(B, T)$ of Al on InAs	155
c.3	Carrier properties of Hall bar anodized at 4.8 V, β	157
c.4	Quantum Hall effect of Hall bar with $V_{AO} = 4.8$ V, β	158
c.5	Other AO-defined Josephson Junctions	161
c.6	Magnetoresistivity study of 4.2 V, α	163

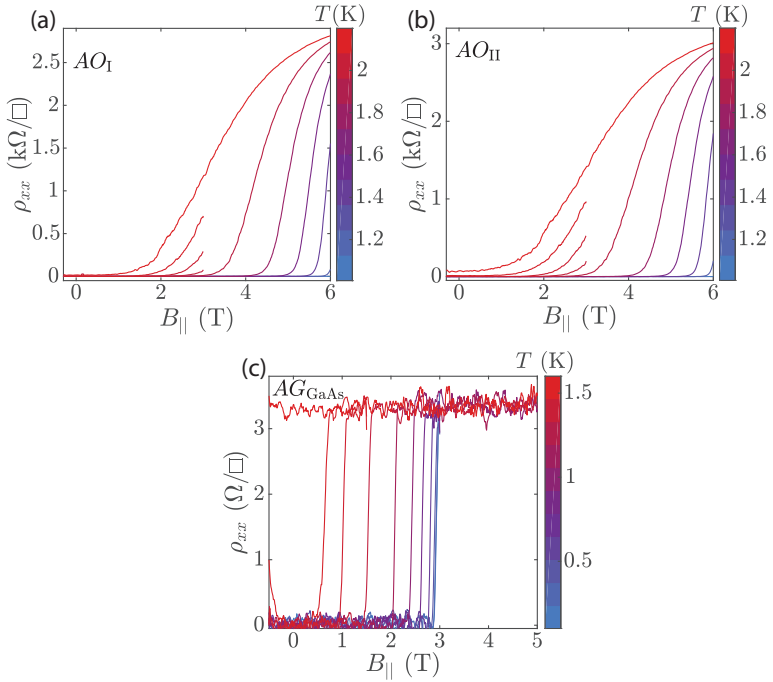
C.1 $R(B, T)$ OF AL ON GAAS

Figure C.1: **Resistivity isotherms of Al on GaAs as a function of $B_{||}$.** All three devices are included: **(a)** AO_I bar. **(b)** AO_{II} bar. **(c)** As-grown Al, AG_{GaAs} bar. For (a) and (b) the lowest temperature plotted is 1 K, where both devices stay superconducting beyond 6 T. The data was used to extract $B_{c,||}(T)$ for [figure 4.3](#) in the main text.

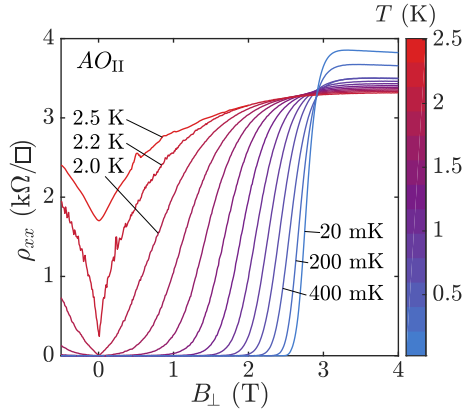


Figure C.2: **Resistivity isotherms of Al on GaAs as a function of B_{\perp} .** Measurements from the AO_{II} bar. The data was used to extract $B_{c,\perp}(T)$ for [figure 4.3](#) in the main text.

C.2 $R(B, T)$ OF AL ON INAS

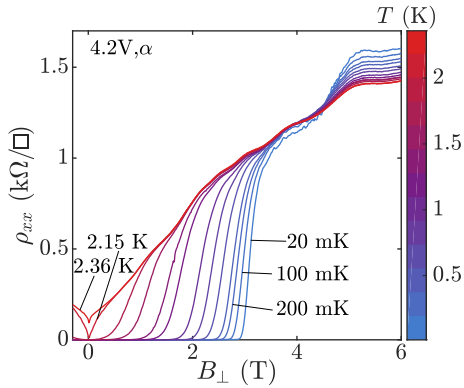


Figure C.3: **Resistivity isotherms from $V_{AO} = 4.2$ V of device α , as a function of B_{\perp} .** The data was used to extract $B_{c,\perp}(T)$ for [figure 5.2\(c\)](#) in the main text.

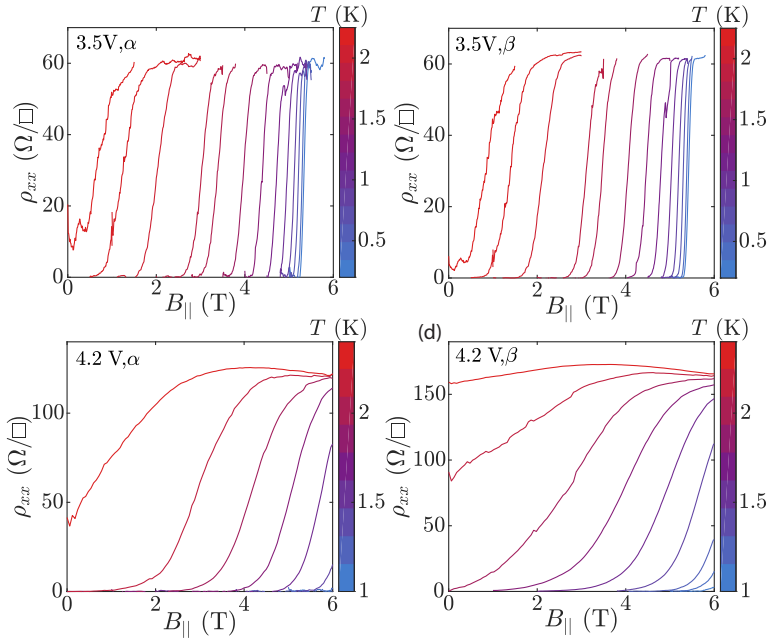


Figure C.4: **Resistivity isotherms as a function of B_{\parallel} for bars anodized at 3.5 V and 4.2 V on device α and β .** The data has bar-labels in the top-left corner of each sub-figure. The data was used to extract $B_{c,\parallel}(T)$ for [figure 5.2\(a\)](#) in the main text.

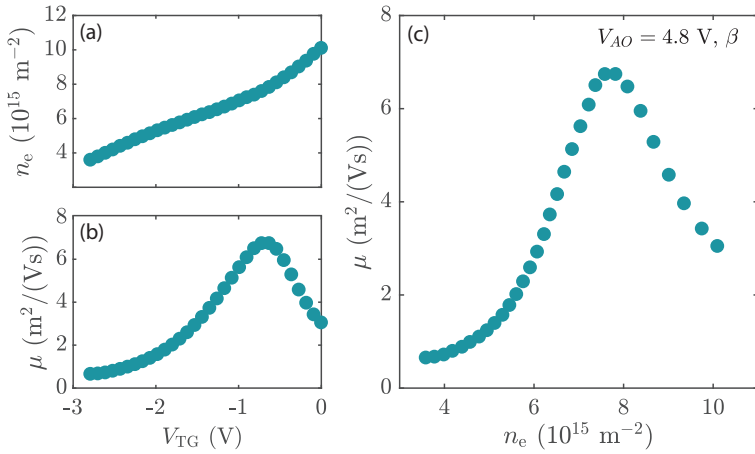


Figure C.5: **Hall measurements for 4.8 V Hall bar on device β .**
(a) Carrier density as a function of top-gate voltage. **(b)** Carrier mobility as a function of top-gate voltage. **(c)** Carrier mobility as a function of carrier density.

C.3 CARRIER PROPERTIES OF HALL BAR ANODIZED AT 4.8 V, β

In addition to the anodized Hall bars mentioned in the main text [section 5.3](#), another Hall bar, also exposed to AO at 4.8 V but on device β , was fabricated and measured, see [figure C.5](#). Its mobility peak of $67 \cdot 10^3 \text{ cm}^2/\text{Vs}$ at $n_e = 7.7 \cdot 10^{11} \text{ cm}^{-2}$ is slightly lower than the 4.8 V bar in the main text, which had $80 \cdot 10^3 \text{ cm}^2/\text{Vs}$ at an equal density. The corresponding longest l_e is 971 nm, calculated by [equation 2.17](#).

As mentioned in the main text [subsection 3.3.3](#) the used AO setup is not sufficient to reproduce results close to full oxidation of the Al, where a small change in oxidation depth significantly impacts superconducting properties before full oxidation. After full Al oxidation the semiconductor properties are sensitive the oxidation depth.

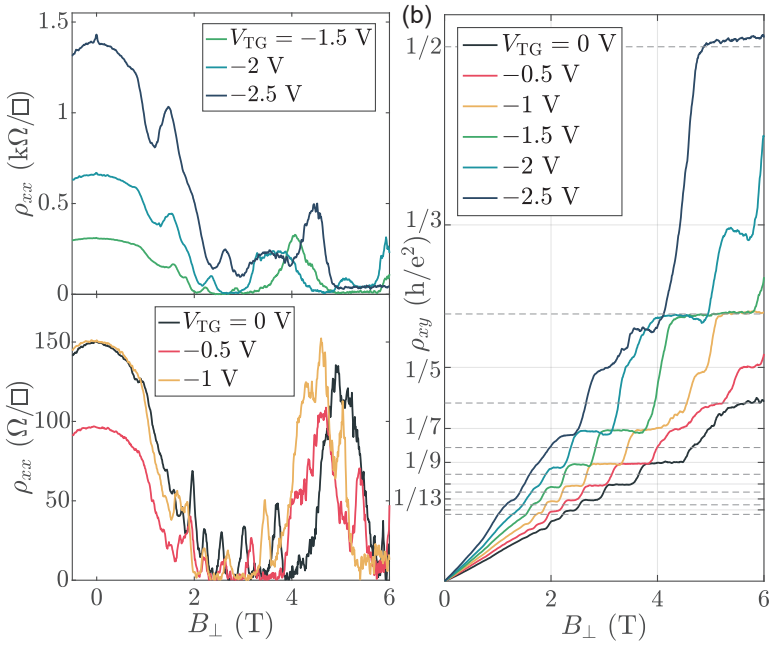
C.4 QUANTUM HALL EFFECT OF HALL BAR WITH $V_{AO} = 4.8$ V, β 

Figure C.6: **Shubnikov-de Haas oscillations and Hall quantization from Hall bar with $V_{AO} = 4.8$ V on device β .**

Longitudinal (a) and Hall (b) resistivities as a function of B_{\perp} for different top-gate voltages in between 0 and -2.5 V in steps of 0.5 V. Hall resistivity is displayed in integer fractions of h/e^2 , with even and odd denominators being marked by dashed and solid lines respectively.

Data is extracted from maps in [figure C.7](#).

[Figure C.6](#) and [C.7](#) presents high perpendicular magnetic fields data from the Hall bar anodized at 4.8 V from device β .

Shubnikov-de Haas oscillations are observed in [figure C.6\(a\)](#) and ρ_{xx} almost reaches zero for intermediate B_{\perp} . Therefore, the plateaus in Hall resistivity, seen [figure C.6\(b\)](#), are close to the expected integer values.

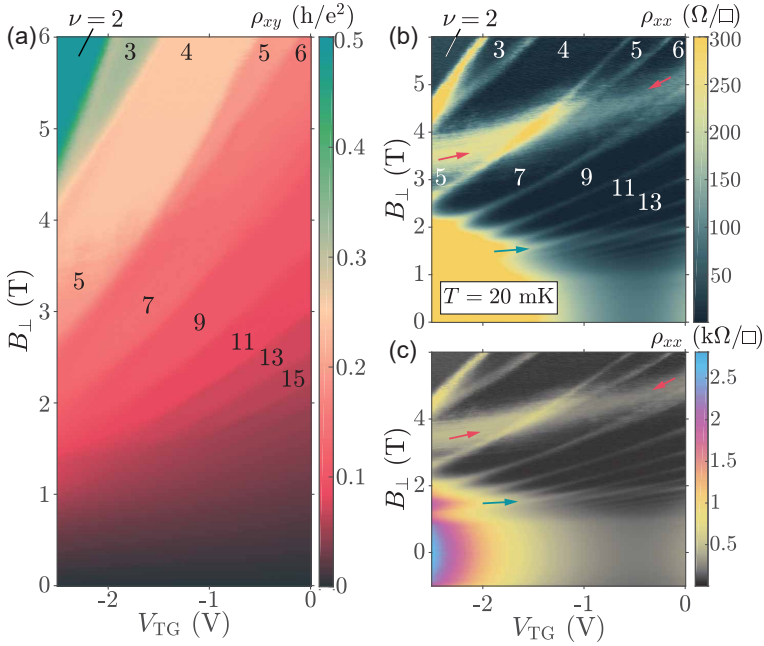


Figure C.7: **Quantum Hall measurements for Hall bar with $V_{AO} = 4.8 \text{ V}$ on device β .**

2D maps of the Hall (a) and longitudinal (b) resistivities as a function of B_{\perp} and top-gate V_{TG} . Extracted filling factors are indicated on the maps. (c) Same data as shown in (b), but without color saturation, allowing us to see more features including the weak localization peak around zero perpendicular magnetic field and negative top-gate voltages. Arrows in (b-c) highlight additional resonances.

Weak localization is also present in ρ_{xx} of this Hall bar similar to that observed in the 4.8 V Hall bar on device α from main text.

Inspecting the ρ_{xx} data from [figure C.6\(a\)](#) and [C.7\(b-c\)](#), we again see additional resonances (marked by arrows in [figure C.7](#)), similar to those observed in [figure 5.4](#) and [5.5](#) of the main text. Both bars showing similar resonances indicates that they are material or process related, not just a spurious effect on a single device.

Number of edge modes, ν , is extracted from [figure C.7\(a\)](#) and added to the ρ_{xx} map. We observe, as for the $V_{AO} = 4.8\text{V}$ Hall bar on device α , that crossing the resonance in [figure C.7\(b\)](#) (marked by red arrows) adds 1 to ν .

C.5 OTHER AO-DEFINED JOSEPHSON JUNCTIONS

Besides the Josephson junction (JJ) reported in [chapter 6](#), other JJs were fabricated on the same chip with increased separations, ζ , between the superconducting leads, indicated on [figure C.8\(a\)](#). The rest of the figure shows supercurrent gate-ability and Fraunhofer oscillations in JJs with $\zeta = 200$ nm, 300 nm, and 400 nm. We have thus shown that thin elongated structures reproducibly can be manufactured with AO using a metal mask.

The gate voltages used for scans in [figure C.8](#) are shown in the table below:

ζ	V_w (V)	V_{TG} (V) in Fraunhofer scan
200 nm	-1.2	-0.56
300 nm	-1.50	0.36
400 nm	-0.70	-0.55

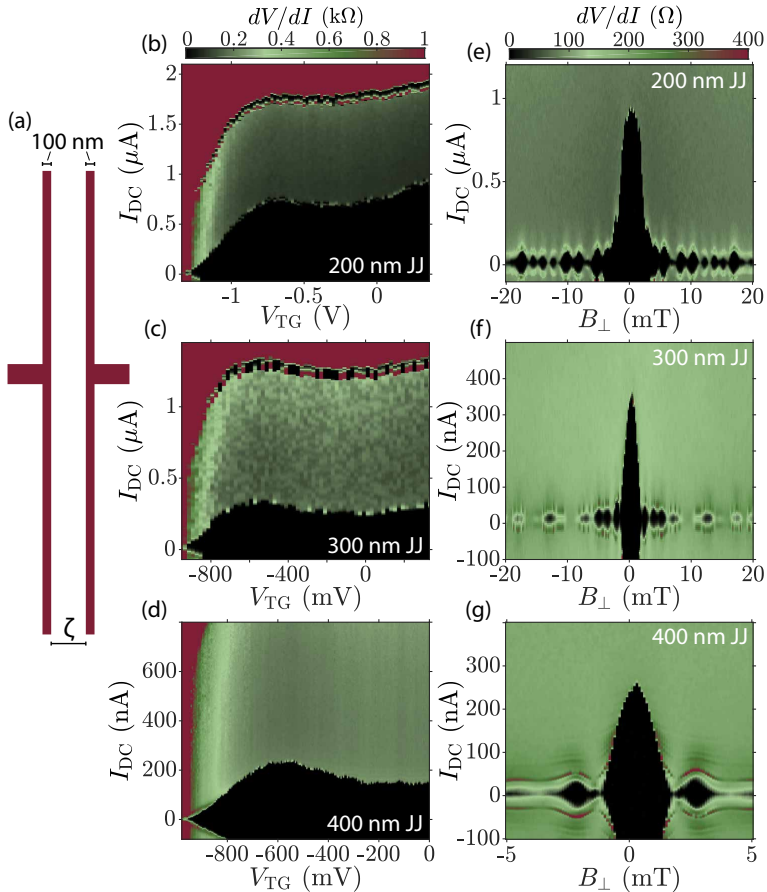


Figure C.8: **Other AO-defined Josephson Junctions** Data from other Josephson junctions (JJs) on the same chip as the 100 nm devices reported in [chapter 6](#). **(a)** Schematic of the design shape of Al for the JJs, introducing the superconductor separation, ζ . **(b-d)** Resistance as a function of DC current bias and top-gate voltage, for devices with $\zeta = 200$ nm, 300 nm, and 400 nm. The maps share color bar. **(e-g)** Resistance as a function of DC current bias and perpendicular magnetic field, for devices with $\zeta = 200$ nm, 300 nm, and 400 nm, marked in right corner of each sub-figure. The maps share color bar.

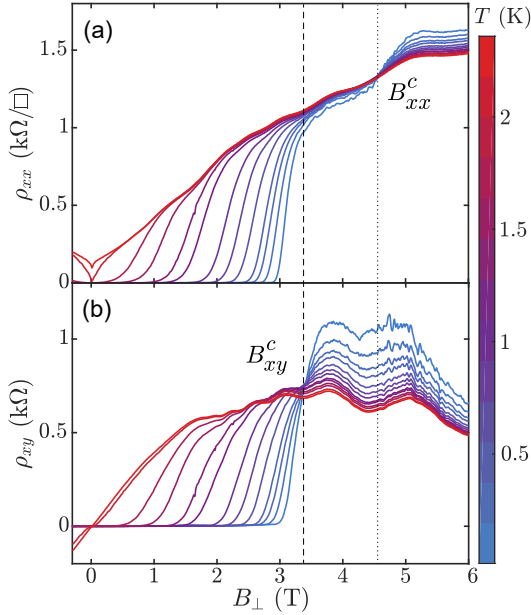


Figure C.9: **Magneto-resistivity isotherms from bar α .** (a) Longitudinal and (b) Hall magneto-resistivity isotherms were measured simultaneously. Crossing of isotherms, B_{xx}^c are marked with dots and B_{xy}^c with stripes. The data of (a) is the same presented in figure C.3.

C.6 MAGNETORESISTIVITY STUDY OF 4.2 V, α

Chapter 7 studied magneto-resistivity of the 4.2 V anodized Hall bar on device β as a function of B_{\perp} , T and I_{DC} . In this section we show similar studies for the 4.2 V Hall bar but from device α . In this section, we will just call the two $V_{\text{AO}} = 4.2$ V Hall bars α and β . As seen on figure 5.2, α had $B_{c,\perp} \sim 3$ T, lower than the $B_{c,\perp} \sim 3.5$ T of β , suggesting the latter to be thinner and/or have more disorder.

From the Hall slope of figure C.9(b) at high temperature, we extract a density $n_e = 1.47 \cdot 10^{12} \text{ cm}^{-2}$. This is higher than the $1.15 \cdot 10^{12} \text{ cm}^{-2}$ extracted from β . The difference could be due to a higher density contribution from the Al, again suggesting more metallic Al being present

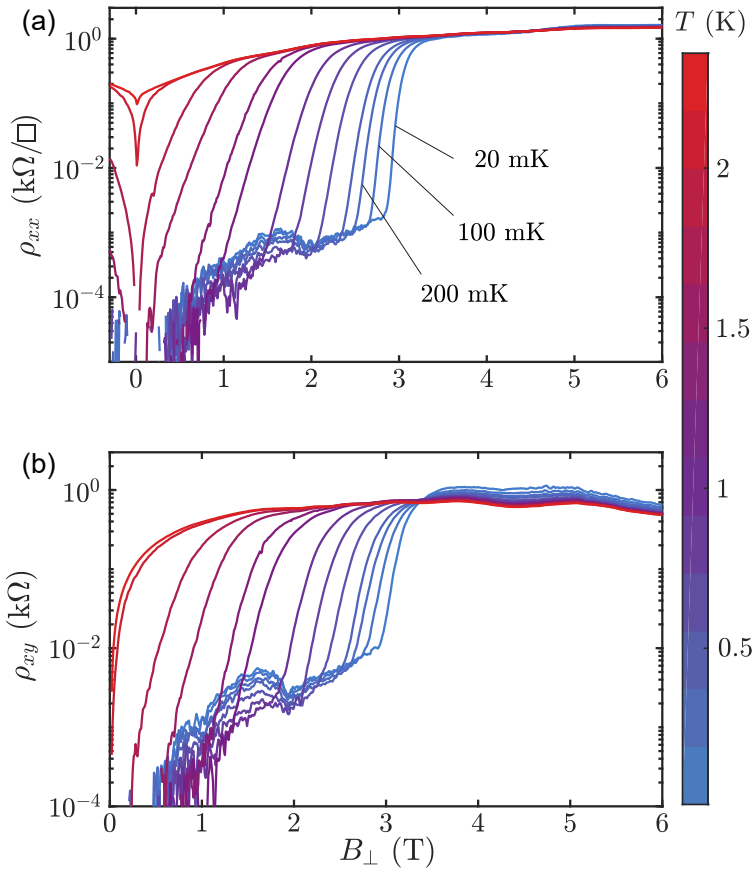


Figure C.10: **Magneto-resistivity isotherms from bar α .** Same data as on [figure C.9](#), but plotted on a log-scale to highlight the small but finite (a) longitudinal and (b) Hall resistivity for $B < B_{c,\perp}$. Resistivity oscillations such as those observed in bar β , [figure 7.3](#), are not as clear for this slightly thicker Al film.

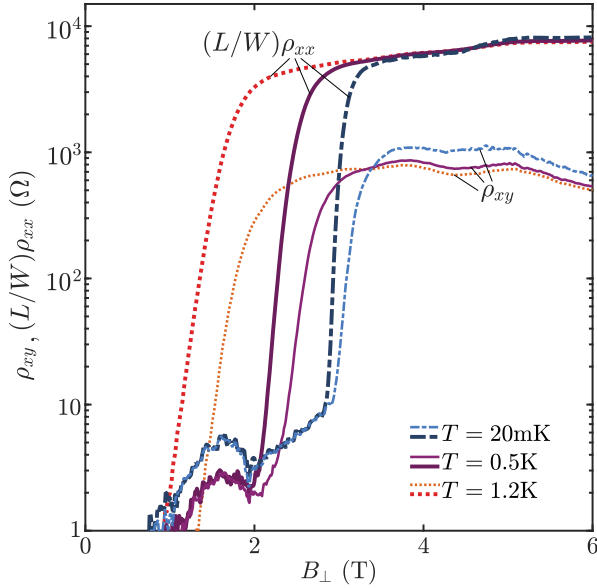


Figure C.11: **Comparing** $R_{xx}(B_{\perp})$ and $R_{xy}(B_{\perp})$. Both resistances are plotted for three different temperatures, 20 mK, 500 mK, and 1.2 K.

in α . The density extracted from the high temperature oscillations of ρ_{xx} and ρ_{xy} are $\sim 7.2 \cdot 10^{11} \text{ cm}^{-2}$ and $7.6 \cdot 10^{11} \text{ cm}^{-2}$, respectively. These are extracted as in the main text: A smoothing spline is used to remove the background and fast Fourier transform with a Hamming window is used to extract the period of the data when plotted versus $1/B_{\perp}$. Density is then calculated using [equation 2.34](#).

Isotherm crossings are also observed for both ρ_{xx} and ρ_{xy} in α , see [figure 5.2](#). As for β , we observe $B_{xx}^c > B_{xy}^c$, opposite to other reports in the literature [[47](#), [48](#)].

As for β we see finite resistivities in α for intermediate $B_{\perp} < B_{c,\perp}$, when plotting ρ_{xx} and ρ_{xy} on a log scale, displayed on [figure C.10](#). The resistivities in α are smaller than those measured in β and clear oscillations as on [figure 7.3](#) are not observed. Thus the amplitude of the

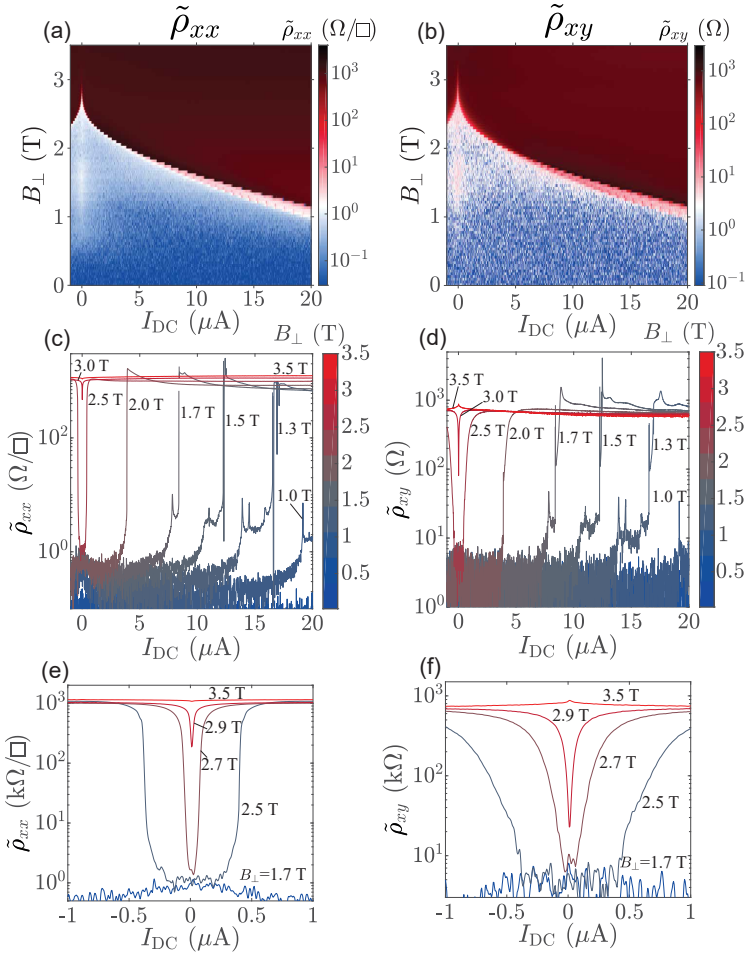


Figure C.12: I_{DC} dependence of ρ_{xx} and ρ_{xy} , measured at $T = 20$ mK. **(a)** Longitudinal and **(b)** Hall resistivity as a function of DC current and perpendicular field. **(c,e)** Longitudinal and **(d,f)** Hall resistivity as a function of DC current for various perpendicular fields. Data extracted from (a) and (b).

small resistances and their oscillations seem to be correlated with the amount of disorder in the aluminum.

A striking observation in [chapter 7](#) was that $R_{xx} = R_{xy}$ for the small resistances. This also is the case for α , displayed [figure C.11](#).

A current dependence study of α is presented in [figure C.12](#). Here, there is no clear evidence of vortex creep besides just before I_c . This suggests a stronger vortex pinning than for β , where a significant vortex motion was observed, causing finite longitudinal voltage drop, reported in [figure 7.7\(a\)](#).

D

LANDAU-BÜTTIKER ANALYSIS WITH $R_{xx} = R_{xy}$

Based on the $R_{xx} = R_{xy}$ observation made in [chapter 7](#) and [section C.6](#), a Landauer-Büttiker analysis [[16](#)] was executed. [Figure D.2](#) shows voltage probe naming convention, while [figure D.2](#) shows the setups used for the analyses. A current is sourced between probe 1 and 4, while probes 2, 3, 5, and 6, have high impedance and are only used for voltage measurements. In the two experiments only one set of V_{xx} and V_{xy} was measured, but the following analysis assumes that $R_{xx} = R_{xy}$ is true in all four configurations:

$$|V_6 - V_5| = |V_2 - V_3| = |V_2 - V_6| = |V_3 - V_5| \quad (\text{D.1})$$

In the analysis, we will use the term "common probe", which denotes the probe being used for both longitudinal and Hall voltage drop.

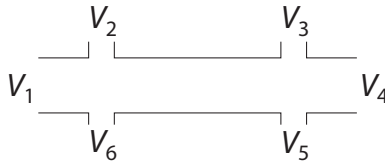


Figure D.1: **Voltage probes on Hall bar**

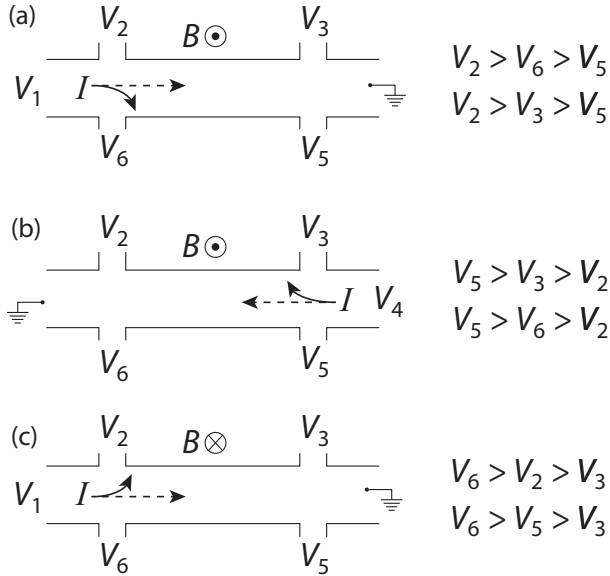


Figure D.2: **Setups used for Landauer-Büttiker analysis.** (a) Current runs from probe 1 to 4. (b) Current runs from probe 4 to 1. (c) Current runs from probe 1 to 4, but B is reversed.

We start with the configuration of [figure D.2\(a\)](#). The calculations, displayed in [table 4](#), predict a diagonal voltage drop $V_D = V_6 - V_3 = 0$.

Common probe	
6	$\left. \begin{aligned} I \cdot R_L &= V_6 - V_5 \\ I \cdot R_H &= V_2 - V_6 \end{aligned} \right\} \rightarrow 2V_6 = V_2 + V_5$
5	$\left. \begin{aligned} I \cdot R_L &= V_6 - V_5 \\ I \cdot R_H &= V_3 - V_5 \end{aligned} \right\} \rightarrow V_6 = V_3$
3	$\left. \begin{aligned} I \cdot R_L &= V_2 - V_3 \\ I \cdot R_H &= V_3 - V_5 \end{aligned} \right\} \rightarrow 2V_3 = V_2 + V_5$
2	$\left. \begin{aligned} I \cdot R_L &= V_2 - V_3 \\ I \cdot R_H &= V_2 - V_6 \end{aligned} \right\} \rightarrow V_6 = V_3$

Table 4: Landau-Bütikker calculations using setup from [figure D.2\(a\)](#) and the condition [equation D.1](#). Combining results from common probe 6 and 3, we find the same result as the two others: $V_6 = V_3$.

Changing the current direction, [figure D.2\(b\)](#), results in the same condition, here only shown for the common probe 5 calculation:

$$\left. \begin{aligned} I \cdot R_L &= V_5 - V_6 \\ I \cdot R_H &= V_5 - V_3 \end{aligned} \right\} \rightarrow V_6 = V_3. \quad (\text{D.2})$$

Changing the field-direction instead, see [figure D.2\(c\)](#), leads to another condition, here shown from the common probe 6 calculation:

$$\left. \begin{aligned} I \cdot R_L &= V_6 - V_5 \\ I \cdot R_H &= V_6 - V_2 \end{aligned} \right\} \rightarrow V_2 = V_5. \quad (\text{D.3})$$

We now find a prediction for the off-diagonal voltage drop

$$V_{\overline{D}} = V_5 - V_2 = 0. \quad (\text{D.4})$$

These predictions could easily be tested with another cool down.

BIBLIOGRAPHY

- [1] R. P. Feynman, "Simulating physics with computers," *Int. J. Theor. Phys.*, vol. 21, p. 467, 1982. (Cited on page 1.)
- [2] P. Shor, "Algorithms for quantum computation: discrete logarithms and factoring," in *Proc. 35th Annu. Symp. Found. Comput. Sci.*, 1994. (Cited on page 1.)
- [3] F. Arute, K. Arya, R. Babbush, D. Bacon, J. C. Bardin, R. Barends, R. Biswas, S. Boixo, F. G. Brandao, D. A. Buell, B. Burkett, Y. Chen, Z. Chen, B. Chiaro, R. Collins, W. Courtney, A. Dunsworth, E. Farhi, B. Foxen, A. Fowler, C. Gidney, M. Giustina, R. Graff, K. Guerin, S. Habegger, M. P. Harrigan, M. J. Hartmann, A. Ho, M. Hoffmann, T. Huang, T. S. Humble, S. V. Isakov, E. Jeffrey, Z. Jiang, D. Kafri, K. Kechedzhi, J. Kelly, P. V. Klimov, S. Knysh, A. Korotkov, F. Kostritsa, D. Landhuis, M. Lindmark, E. Lucero, D. Lyakh, S. Mandrà, J. R. McClean, M. McEwen, A. Megrant, X. Mi, K. Michielsen, M. Mohseni, J. Mutus, O. Naaman, M. Neeley, C. Neill, M. Y. Niu, E. Ostby, A. Petukhov, J. C. Platt, C. Quintana, E. G. Rieffel, P. Roushan, N. C. Rubin, D. Sank, K. J. Satzinger, V. Smelyanskiy, K. J. Sung, M. D. Trevithick, A. Vainsencher, B. Viallonga, T. White, Z. J. Yao, P. Yeh, A. Zalcman, H. Neven, and

- J. M. Martinis, “Quantum supremacy using a programmable superconducting processor,” *Nature*, vol. 574, p. 505, 2019. (Cited on page 2.)
- [4] S. Das Sarma, M. Freedman, and C. Nayak, “Topological quantum computation,” *Phys. Today*, vol. 59, p. 32, 2006. (Cited on page 2.)
- [5] Y. Oreg, G. Refael, and F. Von Oppen, “Helical liquids and Majorana bound states in quantum wires,” *Phys. Rev. Lett.*, vol. 105, p. 177002, 2010. (Cited on pages 2, 41, and 42.)
- [6] R. M. Lutchyn, J. D. Sau, and S. Das Sarma, “Majorana fermions and a topological phase transition in semiconductor-superconductor heterostructures,” *Phys. Rev. Lett.*, vol. 105, p. 077001, 2010. (Cited on pages 2, 41, and 42.)
- [7] F. Pientka, A. Keselman, E. Berg, A. Yacoby, A. Stern, and B. I. Halperin, “Topological superconductivity in a planar Josephson junction,” *Phys. Rev. X*, vol. 7, p. 021032, 2017. (Cited on pages 2, 45, and 104.)
- [8] M. Hell, M. Leijnse, and K. Flensberg, “Two-Dimensional Platform for Networks of Majorana Bound States,” *Phys. Rev. Lett.*, vol. 118, p. 107701, 2017. (Cited on pages 2, 45, and 104.)
- [9] D. J. Clarke, J. Alicea, and K. Shtengel, “Exotic circuit elements from zero-modes in hybrid superconductor–quantum-Hall systems,” *Nat. Phys.*, vol. 10, p. 877, 2014. (Cited on pages 2, 45, and 46.)
- [10] P. Krogstrup, N. L. Ziino, W. Chang, S. M. Albrecht, M. H. Madsen, E. Johnson, J. Nygård, C. M. Marcus, and T. S. Jespersen, “Epitaxy of semiconductor-superconductor nanowires,” *Nat. Mater.*, vol. 14, p. 400, 2015. (Cited on pages 3, 50, 52, and 101.)
- [11] J. Shabani, M. Kjaergaard, H. J. Suominen, Y. Kim, F. Nichele, K. Pakrouski, T. Stankevic, R. M. Lutchyn, P. Krogstrup, R. Feidenhans’L, S. Kraemer, C. Nayak, M. Troyer, C. M. Marcus,

- and C. J. Palmstrøm, "Two-dimensional epitaxial superconductor-semiconductor heterostructures: A platform for topological superconducting networks," *Phys. Rev. B*, vol. 93, p. 155402, 2016. (Cited on pages 3, 50, 51, 52, 53, and 66.)
- [12] F. Krizek, J. E. Sestoft, P. Aseev, S. Marti-Sanchez, S. Vaitiekėnas, L. Casparis, S. A. Khan, Y. Liu, T. Stankevič, A. M. Whiticar, A. Fursina, F. Boekhout, R. Koops, E. Uccelli, L. P. Kouwenhoven, C. M. Marcus, J. Arbiol, and P. Krogstrup, "Field effect enhancement in buffered quantum nanowire networks," *Phys. Rev. Mater.*, vol. 2, p. 093401, 2018. (Cited on pages 3 and 50.)
- [13] W. Chang, *Superconducting Proximity Effect in InAs Nanowires*. Ph.d., Harvard, 2014. (Cited on page 3.)
- [14] J. H. Davies, *The Physics of Low-Dimensional Semiconductors: An Introduction*. Cambridge University Press, 1998. (Cited on pages 6, 11, 12, and 56.)
- [15] C. Kittel, *Introduction to Solid State Physics*. Wiley, 2010. (Cited on pages 6, 10, 13, 25, and 140.)
- [16] T. Ihn, *Semiconductor Nanostructures*. Oxford University Press, 2010. (Cited on pages 6, 12, 14, 15, 17, 18, 20, 43, 44, 51, 54, 118, and 169.)
- [17] S. H. Simon, *The Oxford Solid State Basics*. Oxford, 2013. (Cited on pages 6, 7, and 13.)
- [18] H. L. Störmer, A. C. Gossard, and W. Wiegmann, "Observation of intersubband scattering in a 2-dimensional electron system," *Solid State Commun.*, vol. 41, p. 707, 1982. (Cited on page 12.)
- [19] D. J. Griffiths, *Introduction to Quantum Mechanics*. Pearson Prentice Hall, 1995. (Cited on page 13.)
- [20] V. Umansky, R. De-Picciotto, and M. Heiblum, "Extremely high-mobility two dimensional electron gas: evaluation of scattering mechanisms," *Appl. Phys. Lett.*, vol. 71, p. 683, 1997. (Cited on page 13.)

- [21] M. J. Manfra, “Molecular Beam Epitaxy of Ultra-High-Quality AlGaAs/GaAs Heterostructures: Enabling Physics in Low-Dimensional Electronic Systems,” *Annu. Rev. Condens. Matter Phys.*, vol. 5, p. 347, 2014. (Cited on page 13.)
- [22] T. Tschirky, S. Mueller, C. A. Lehner, S. Fält, T. Ihn, K. Ensslin, and W. Wegscheider, “Scattering mechanisms of highest-mobility InAs/AlxGa1-xSb quantum wells,” *Phys. Rev. B*, vol. 95, p. 115304, 2017. (Cited on pages 13 and 53.)
- [23] A. T. Hatke, T. Wang, C. Thomas, G. C. Gardner, and M. J. Manfra, “Mobility in excess of 10^6 cm²/V s in InAs quantum wells grown on lattice mismatched InP substrates,” *Appl. Phys. Lett.*, vol. 111, p. 142106, 2017. (Cited on pages 13 and 53.)
- [24] C. Thomas, A. T. Hatke, A. Tuaz, R. Kallaher, T. Wu, T. Wang, R. E. Diaz, G. C. Gardner, M. A. Capano, and M. J. Manfra, “High-mobility InAs 2DEGs on GaSb substrates: A platform for mesoscopic quantum transport,” *Phys. Rev. Mater.*, vol. 2, p. 104602, 2018. (Cited on pages 13, 53, and 54.)
- [25] C. R. Dean, A. F. Young, I. Meric, C. Lee, L. Wang, S. Sorgenfrei, K. Watanabe, T. Taniguchi, P. Kim, K. L. Shepard, and J. Hone, “Boron nitride substrates for high-quality graphene electronics,” *Nat. Nanotechnol.*, vol. 5, p. 722, 2010. (Cited on page 13.)
- [26] D. G. Purdie, N. M. Pugno, T. Taniguchi, K. Watanabe, A. C. Ferrari, and A. Lombardo, “Cleaning interfaces in layered materials heterostructures,” *Nat. Commun.*, vol. 9, p. 5387, 2018. (Cited on page 13.)
- [27] E. C. O’Farrell, A. C. Drachmann, M. Hell, A. Fornieri, A. M. Whiticar, E. B. Hansen, S. Gronin, G. C. Gardner, C. Thomas, M. J. Manfra, K. Flensberg, C. M. Marcus, and F. Nichele, “Hybridization of Subgap States in One-Dimensional Superconductor-Semiconductor Coulomb Islands,” *Phys. Rev. Lett.*, vol. 121, p. 256803, 2018. (Cited on pages 15, 45, and 66.)

- [28] Y. Cao, V. Fatemi, S. Fang, K. Watanabe, T. Taniguchi, E. Kaxiras, and P. Jarillo-Herrero, “Unconventional superconductivity in magic-angle graphene superlattices,” *Nature*, vol. 556, no. 7699, p. 43, 2018. (Cited on pages 21 and 112.)
- [29] A. L. Sharpe, E. J. Fox, A. W. Barnard, J. Finney, K. Watanabe, T. Taniguchi, M. A. Kastner, and D. Goldhaber-Gordon, “Emergent ferromagnetism near three-quarters filling in twisted bilayer graphene,” *Science*, vol. 365, p. 605, 2019. (Cited on page 21.)
- [30] H. K. Onnes, “Further experiments with liquid helium. D. On the change of the electrical resistance of pure metals at very low temperatures, etc. V. The disappearance of the resistance of mercury.,” *Leiden Comm.*, vol. 122b, p. 264, 1911. (Cited on page 22.)
- [31] F. Pobell, *Matter and methods at low temperatures*. Springer, 2007. (Cited on pages 22 and 73.)
- [32] J. Bardeen, L. N. Cooper, and J. R. Schrieffer, “The microscopic theory of superconductivity,” *Phys. Rev.*, vol. 106, p. 162, 1957. (Cited on page 22.)
- [33] J. Bardeen, L. N. Cooper, and J. R. Schrieffer, “Theory of superconductivity,” *Phys. Rev.*, vol. 108, p. 1175, 1957. (Cited on page 22.)
- [34] V. L. Ginzburg and L. D. Landau, “On the theory of superconductivity,” *Zh. Eksperim. i Teor. Fiz.*, vol. 20, p. 1064, 1950. (Cited on page 24.)
- [35] L. P. Gor’kov, “Microscopic derivation of the Ginzburg-Landau equations in the theory of superconductivity,” *Sov. Phys.-JETP*, vol. 9, p. 1364, 1959. (Cited on page 24.)
- [36] M. Tinkham, *Introduction to Superconductivity*. New York: McGraw-Hill Book Co., second ed., 1996. (Cited on pages 25, 27, 28, 29, and 41.)
- [37] B. S. Chandrasekhar, “A note on the maximum critical field of high-field superconductors,” *Appl. Phys. Lett.*, vol. 1, pp. 7–8, 1962. (Cited on page 28.)

- [38] A. M. Clogston, “Upper limit for the critical field in hard superconductors,” *Phys. Rev. Lett.*, vol. 9, p. 266, 1962. (Cited on page 28.)
- [39] P. M. Tedrow and R. Meservey, “Critical magnetic field of very thin superconducting aluminium films,” *Phys. Rev. B*, vol. 25, p. 171, 1982. (Cited on page 28.)
- [40] H. Nam, H. Chen, T. Liu, J. Kim, C. Zhang, J. Yong, T. R. Lemberger, P. A. Kratz, J. R. Kirtley, K. Moler, P. W. Adams, A. H. MacDonald, and C.-K. Shih, “Ultrathin two-dimensional superconductivity with strong spin-orbit coupling,” *Proc. Natl. Acad. Sci.*, vol. 113, p. 10513, 2016. (Cited on page 28.)
- [41] F. E. Harper and M. Tinkham, “The mixed state in superconducting thin films,” *Phys. Rev.*, vol. 172, p. 441, 1968. (Cited on page 29.)
- [42] R. W. Cohen and B. Abeles, “Superconductivity in Granular Aluminum Films,” *Phys. Rev.*, vol. 168, p. 444, 1968. (Cited on pages 29, 30, 82, and 89.)
- [43] Y. Ivry, C. S. Kim, A. E. Dane, D. De Fazio, A. N. McCaughan, K. A. Sunter, Q. Zhao, and K. K. Berggren, “Universal scaling of the critical temperature for thin films near the superconducting-to-insulating transition,” *Phys. Rev. B*, vol. 90, p. 214515, 2014. (Cited on pages 29 and 89.)
- [44] M. Strongin, R. S. Thompson, O. F. Kammerer, and J. E. Crow, “Destruction of Superconductivity in Disordered Near-Monolayer Films,” *Phys. Rev. B*, vol. 1, pp. 1078–1091, 1970. (Cited on page 30.)
- [45] K. K. Man’koskii, V. V. Pilipenko, Y. F. Komnik, and I. M. Dmitrenko, “Critical Temperature of Superconducting Transition of Thin Tin Films,” *Sov. Phys. JETP*, vol. 32, p. 404, 1971. (Cited on page 30.)
- [46] D. B. Haviland, Y. Liu, and A. M. Goldman, “Onset of superconductivity in the two-dimensional limit,” *Phys. Rev. Lett.*, vol. 62, p. 2180, 1989. (Cited on page 30.)

-
- [47] N. P. Breznay, M. A. Steiner, S. A. Kivelson, and A. Kapitulnik, "Self-duality and a Hall-insulator phase near the superconductor-to-insulator transition in indium-oxide films," *Proc. Natl. Acad. Sci. U. S. A.*, vol. 113, p. 280, 2016. (Cited on pages 30, 31, 115, and 165.)
- [48] M. A. Paalanen, A. F. Hebard, and R. R. Ruel, "Low-temperature insulating phases of uniformly disordered two-dimensional superconductors," *Phys. Rev. Lett.*, vol. 69, p. 1604, 1992. (Cited on pages 30, 31, 115, and 165.)
- [49] N. P. Breznay, M. Tendulkar, L. Zhang, S. C. Lee, and A. Kapitulnik, "Superconductor to weak-insulator transitions in disordered tantalum nitride films," *Phys. Rev. B*, vol. 96, p. 134522, 2017. (Cited on pages 31 and 115.)
- [50] A. F. Andreev, "The thermal conductivity of the intermediate state in superconductors," *Sov. Phys. JETP*, vol. 19, p. 1228, 1964. (Cited on page 31.)
- [51] G. E. Blonder, M. Tinkham, and T. M. Klapwijk, "Transition from metallic to tunneling regimes in superconducting microconstrictions: Excess current, charge imbalance, and supercurrent conversion," *Phys. Rev. B*, vol. 25, p. 4515, apr 1982. (Cited on page 31.)
- [52] T. Schäpers, *Superconductor/Semiconductor Junctions*, vol. 174. Springer, 2001. (Cited on pages 32, 34, 35, 37, and 39.)
- [53] A. A. Golubov and M. Y. Kupriyanov, "Quasiparticle current in ballistic F/ScN junctions," *Phys. C*, vol. 259, p. 27, 1995. (Cited on page 35.)
- [54] T. M. Klapwijk, "Proximity effect from an Andreev perspective," *J. Supercond. Nov. Magn.*, vol. 17, p. 593, 2004. (Cited on page 37.)
- [55] G. Eilenberger, "Transformation of Gorkov's equation for type II superconductors into transport-like equations," *Zeitschrift für Phys.*, vol. 214, p. 195, 1968. (Cited on page 38.)

- [56] B. Aminov, A. Golubov, and M. Y. Kupriyanov, "Quasiparticle current in ballistic constrictions with finite transparencies of interfaces," *Phys. Rev. B - Condens. Matter Mater. Phys.*, vol. 53, p. 365, 1996. (Cited on pages 38 and 39.)
- [57] V. Cherkez, J. C. Cuevas, C. Brun, T. Cren, G. Ménard, F. Debontridder, V. S. Stolyarov, and D. Roditchev, "Proximity effect between two superconductors spatially resolved by scanning tunneling spectroscopy," *Phys. Rev. X*, vol. 4, p. 011033, 2014. (Cited on page 38.)
- [58] C. W. J. Beenakker, "Quantum transport in semiconductor-superconductor microjunctions," *Phys. Rev. B*, vol. 46, p. 12841, 1992. (Cited on page 40.)
- [59] B. Josephson, "Possible new effects in superconductive tunnelling," *Phys. Lett.*, vol. 1, p. 251, 1962. (Cited on page 40.)
- [60] K. Inoue and T. Kawakami, "Magnetic field dependencies of critical currents in InAs-coupled Josephson junctions," *J. Appl. Phys.*, vol. 65, p. 1631, 1989. (Cited on page 41.)
- [61] H. J. Suominen, J. Danon, M. Kjaergaard, K. Flensberg, J. Shabani, C. J. Palmstrøm, F. Nichele, and C. M. Marcus, "Anomalous Fraunhofer interference in epitaxial superconductor-semiconductor Josephson junctions," *Phys. Rev. B*, vol. 95, p. 035307, 2017. (Cited on pages 41 and 66.)
- [62] E. Majorana, "Teoria simmetrica dell'elettrone e del positrone," *Nuovo Cim.*, vol. 14, p. 171, 1937. (Cited on page 41.)
- [63] P. A. M. Dirac, "The quantum theory of the electron," *Proc. R. Soc. London. Ser. A, Contain. Pap. a Math. Phys. Character*, vol. 117, p. 610, 1928. (Cited on page 41.)
- [64] C. Nayak, S. H. Simon, A. Stern, M. Freedman, and S. Das Sarma, "Non-Abelian anyons and topological quantum computation," *Rev. Mod. Phys.*, vol. 80, p. 1083, 2008. (Cited on page 41.)

-
- [65] A. Y. Kitaev, "Unpaired Majorana fermions in quantum wires," *Physics-Usppekhi*, vol. 44, p. 131, 2001. (Cited on pages 41 and 42.)
- [66] P. Bonderson, M. Freedman, and C. Nayak, "Measurement-only topological quantum computation via anyonic interferometry," *Ann. Phys. (N. Y.)*, vol. 324, p. 787, 2009. (Cited on page 41.)
- [67] D. Aasen, M. Hell, R. V. Mishmash, A. Higginbotham, J. Danon, M. Leijnse, T. S. Jespersen, J. A. Folk, C. M. Marcus, K. Flensberg, and J. Alicea, "Milestones toward Majorana-based quantum computing," *Phys. Rev. X*, vol. 6, p. 031016, 2016. (Cited on page 41.)
- [68] T. Karzig, C. Knapp, R. M. Lutchyn, P. Bonderson, M. B. Hastings, C. Nayak, J. Alicea, K. Flensberg, S. Plugge, Y. Oreg, C. M. Marcus, and M. H. Freedman, "Scalable designs for quasiparticle-poisoning-protected topological quantum computation with Majorana zero modes," *Phys. Rev. B*, vol. 95, p. 235305, 2017. (Cited on page 41.)
- [69] F. Wilczek, "Majorana returns," *Nat. Phys.*, vol. 5, p. 614, 2009. (Cited on page 41.)
- [70] M. Leijnse and K. Flensberg, "Introduction to topological superconductivity and Majorana fermions," *Semicond. Sci. Technol.*, vol. 27, p. 124003, 2012. (Cited on page 42.)
- [71] L. Fu and C. L. Kane, "Superconducting proximity effect and majorana fermions at the surface of a topological insulator," *Phys. Rev. Lett.*, vol. 100, p. 096407, 2008. (Cited on pages 42 and 45.)
- [72] F. von Oppen, Y. Peng, and F. Pientka, "Topological superconducting phases in one dimension," in *Topol. Asp. Condens. Matter Phys. Lect. Notes Les Houches Summer Sch. Vol. 103*, 2015. (Cited on page 44.)
- [73] V. Mourik, K. Zuo, S. M. Frolov, S. R. Plissard, E. P. a. M. Bakkers, and L. P. Kouwenhoven, "Signatures of Majorana Fermions in Hybrid Superconductor-Semiconductor Nanowire Devices," *Science*, vol. 336, p. 1003, 2012. (Cited on page 45.)

- [74] M. T. Deng, S. Vaitiekenas, E. B. Hansen, J. Danon, M. Leijnse, K. Flensberg, J. Nygård, P. Krogstrup, and C. M. Marcus, “Majorana bound state in a coupled quantum-dot hybrid-nanowire system,” *Science*, vol. 354, p. 1557, 2016. (Cited on page 45.)
- [75] F. Nichele, A. C. C. Drachmann, A. M. Whiticar, E. C. T. O’Farrell, H. J. Suominen, A. Fornieri, T. Wang, G. C. Gardner, C. Thomas, A. T. Hatke, P. Krogstrup, M. J. Manfra, K. Flensberg, and C. M. Marcus, “Scaling of Majorana Zero-Bias Conductance Peaks,” *Phys. Rev. Lett.*, vol. 119, p. 136803, 2017. (Cited on pages 45, 61, and 66.)
- [76] C. Moore, T. D. Stanescu, and S. Tewari, “Two-terminal charge tunneling: Disentangling Majorana zero modes from partially separated Andreev bound states in semiconductor-superconductor heterostructures,” *Phys. Rev. B*, vol. 97, p. 165302, 2018. (Cited on page 45.)
- [77] S. M. Albrecht, A. P. Higginbotham, M. Madsen, F. Kuemmeth, T. S. Jespersen, J. Nyg, P. Krogstrup, and C. M. Marcus, “Exponential Protection of Zero Modes in Majorana Islands,” *Nature*, vol. 531, p. 206, 2016. (Cited on page 45.)
- [78] A. M. Whiticar, A. Fornieri, E. C. T. O. Farrell, A. C. C. Drachmann, T. Wang, C. Thomas, S. Gronin, R. Kallaher, G. C. Gardner, M. J. Manfra, C. M. Marcus, and F. Nichele, “Coherent transport through a Majorana island in an Aharonov – Bohm interferometer,” *Nat. Commun.*, vol. 11, p. 3212, 2020. (Cited on pages 45 and 66.)
- [79] A. Fornieri, A. M. Whiticar, F. Setiawan, E. Portolés, A. C. C. Drachmann, A. Keselman, S. Gronin, C. Thomas, T. Wang, R. Kallaher, G. C. Gardner, E. Berg, M. J. Manfra, A. Stern, C. M. Marcus, and F. Nichele, “Evidence of topological superconductivity in planar Josephson junctions,” *Nature*, vol. 569, p. 89, 2019. (Cited on pages 45, 53, 66, 104, 107, and 109.)
- [80] H. Ren, F. Pientka, S. Hart, A. T. Pierce, M. Kosowsky, L. Lunczer, R. Schlereth, B. Scharf, E. M. Hankiewicz, L. W. Molenkamp, B. I. Halperin, and A. Yacoby, “Topological superconductivity in a

- phase-controlled Josephson junction," *Nature*, vol. 569, p. 93, 2019. (Cited on page 45.)
- [81] A. M. Whiticar, *Flux dependence of topological superconductivity in two-dimensional heterostructures*. Ph.d. thesis, University of Copenhagen, 2020. (Cited on page 45.)
- [82] X. L. Qi, T. L. Hughes, and S. C. Zhang, "Chiral topological superconductor from the quantum Hall state," *Phys. Rev. B*, vol. 82, p. 184516, 2010. (Cited on page 45.)
- [83] R. S. Mong, D. J. Clarke, J. Alicea, N. H. Lindner, P. Fendley, C. Nayak, Y. Oreg, A. Stern, E. Berg, K. Shtengel, and M. P. Fisher, "Universal topological quantum computation from a superconductor-abelian quantum hall heterostructure," *Phys. Rev. X*, vol. 4, p. 011036, 2014. (Cited on page 45.)
- [84] C. W. J. Beenakker, "Angels & Demons: Majorana & Dirac fermions in a quantum Hall edge channel," 2017. (Cited on pages 45 and 46.)
- [85] G.-H. Lee, K.-F. Huang, D. K. Efetov, D. S. Wei, S. Hart, T. Taniguchi, K. Watanabe, A. Yacoby, and P. Kim, "Inducing superconducting correlation in quantum Hall edge states," *Nat. Phys.*, vol. 13, p. 693, 2017. (Cited on pages 45, 46, 47, 51, and 97.)
- [86] O. Gamayun, J. A. Hutasoit, and V. V. Cheianov, "Two-terminal transport along a proximity-induced superconducting quantum Hall edge," *Phys. Rev. B*, vol. 96, p. 241104, 2017. (Cited on page 46.)
- [87] W. Chang, S. M. Albrecht, T. S. Jespersen, F. Kuemmeth, P. Krogstrup, J. Nygård, and C. M. Marcus, "Hard gap in epitaxial semiconductor-superconductor nanowires," *Nat. Nanotechnol.*, vol. 10, p. 232, 2015. (Cited on pages 50 and 52.)
- [88] S. Vaitiekėnas, A. M. Whiticar, M. T. Deng, F. Krizek, J. E. Sestoft, C. J. Palmstrøm, S. Marti-Sanchez, J. Arbiol, P. Krogstrup, L. Casparis, and C. M. Marcus, "Selective-Area-Grown Semiconductor-Superconductor Hybrids: A Basis for Topological Networks," *Phys. Rev. Lett.*, vol. 121, p. 147701, 2018. (Cited on page 50.)

- [89] M. Kjaergaard, F. Nichele, H. J. Suominen, M. P. Nowak, M. Wimmer, A. R. Akhmerov, J. A. Folk, K. Flensberg, J. Shabani, C. J. Palmstrøm, and C. M. Marcus, “Quantized conductance doubling and hard gap in a two-dimensional semiconductor-superconductor heterostructure,” *Nat. Commun.*, vol. 7, p. 12841, 2016. (Cited on pages 50, 52, and 66.)
- [90] M. Pendharkar, B. Zhang, H. Wu, A. Zarassi, P. Zhang, C. P. Dempsey, J. S. Lee, S. D. Harrington, G. Badawy, S. Gazibegovic, J. Jung, A. H. Chen, M. A. Verheijen, M. Hocevar, E. P. A. M. Bakkers, C. J. Palmstrøm, and S. M. Frolov, “Parity-preserving and magnetic field resilient superconductivity in indium antimonide nanowires with tin shells,” arXiv: 1912.06071. (Cited on page 50.)
- [91] D. J. Carrad, M. Bjergfelt, T. Kanne, M. Aagesen, F. Krizek, E. M. Fiordaliso, E. Johnson, J. Nygård, and T. S. Jespersen, “Shadow Epitaxy for In Situ Growth of Generic Semiconductor/Superconductor Hybrids,” *Adv. Mater.*, vol. 32, p. 1908411, 2020. (Cited on page 50.)
- [92] T. Kanne, M. Marnauza, D. Olsteins, D. J. Carrad, J. E. Sestoft, J. de Bruijkere, L. Zeng, E. Johnson, E. Olsson, K. Grove-Rasmussen, and J. Nygård, “Epitaxial Pb on InAs nanowires,” arXiv: 2002.11641. (Cited on pages 50 and 132.)
- [93] S. W. Hieke, B. Breitbach, G. Dehm, and C. Scheu, “Microstructural evolution and solid state dewetting of epitaxial Al thin films on sapphire (α -Al₂O₃),” *Acta Mater.*, vol. 133, p. 356, 2017. (Cited on page 51.)
- [94] J. Eroms, D. Weiss, J. De Boeck, G. Borghs, and U. Zülicke, “Andreev reflection at high magnetic fields: Evidence for electron and hole transport in edge states,” *Phys. Rev. Lett.*, vol. 95, p. 107001, 2005. (Cited on page 51.)
- [95] S. Hart, H. Ren, T. Wagner, P. Leubner, M. Mühlbauer, C. Brüne, H. Buhmann, L. W. Molenkamp, and A. Yacoby, “Induced superconductivity in the quantum spin Hall edge,” *Nat. Phys.*, vol. 10, p. 638, 2014. (Cited on page 51.)

- [96] Z. Wan, A. Kazakov, M. J. Manfra, L. N. Pfeiffer, K. W. West, and L. P. Rokhinson, "Induced superconductivity in high-mobility two-dimensional electron gas in gallium arsenide heterostructures," *Nat. Commun.*, vol. 6, p. 7426, 2015. (Cited on pages 51 and 97.)
- [97] V. E. Calado, S. Goswami, G. Nanda, M. Diez, A. R. Akhmerov, K. Watanabe, T. Taniguchi, T. M. Klapwijk, and L. M. Vandersypen, "Ballistic Josephson junctions in edge-contacted graphene," *Nat. Nanotechnol.*, vol. 10, p. 761, 2015. (Cited on page 51.)
- [98] F. Amet, C. T. Ke, I. V. Borzenets, J. Wang, K. Watanabe, T. Taniguchi, R. S. Deacon, M. Yamamoto, Y. Bomze, S. Tarucha, and G. Finkelstein, "Supercurrent in the quantum Hall regime," *Science*, vol. 352, p. 966, 2016. (Cited on pages 51 and 97.)
- [99] Q. L. He, L. Pan, A. L. Stern, E. C. Burks, X. Che, G. Yin, J. Wang, B. Lian, Q. Zhou, E. S. Choi, K. Murata, X. Kou, Z. Chen, T. Nie, Q. Shao, Y. Fan, S.-C. Zhang, K. Liu, J. Xia, and K. L. Wang, "Chiral Majorana fermion modes in a quantum anomalous Hall insulator–superconductor structure," *Science*, vol. 357, p. 294, 2017. (Cited on pages 51 and 97.)
- [100] S. Matsuo, K. Ueda, S. Baba, H. Kamata, M. Tateno, J. Shabani, C. J. Palmstrøm, and S. Tarucha, "Equal-Spin Andreev Reflection on Junctions of Spin-Resolved Quantum Hall Bulk State and Spin-Singlet Superconductor," *Sci. Rep.*, vol. 8, p. 3454, 2018. (Cited on page 51.)
- [101] S. Guiducci, M. Carrega, G. Biasiol, L. Sorba, F. Beltram, and S. Heun, "Toward Quantum Hall Effect in a Josephson Junction," *Phys. Status Solidi - Rapid Res. Lett.*, vol. 13, p. 1800222, 2019. (Cited on pages 51 and 97.)
- [102] M. Kjaergaard, H. J. Suominen, M. P. Nowak, A. R. Akhmerov, J. Shabani, C. J. Palmstrøm, F. Nichele, and C. M. Marcus, "Transparent Semiconductor-Superconductor Interface and Induced Gap in an Epitaxial Heterostructure Josephson Junction," *Phys. Rev. Appl.*, vol. 7, p. 034029, 2017. (Cited on pages 52, 56, and 66.)

- [103] S. J. Pauka, J. D. S. Witt, C. N. Allen, B. Harlech-Jones, A. Jouan, G. C. Gardner, S. Gronin, T. Wang, C. Thomas, M. J. Manfra, D. J. Reilly, and M. C. Cassidy, “Repairing the Surface of InAs-based Topological Heterostructures,” arXiv: 1908.08689v1. (Cited on pages 52, 53, 56, and 66.)
- [104] K. S. Wickramasinghe, W. Mayer, J. Yuan, T. Nguyen, L. Jiao, V. Manucharyan, and J. Shabani, “Transport properties of near surface InAs two-dimensional heterostructures,” *Appl. Phys. Lett.*, vol. 113, p. 262104, 2018. (Cited on pages 53 and 66.)
- [105] B. Shojaei, A. Drachmann, M. Pendharkar, D. Pennachio, M. Echlin, P. Callahan, S. Kraemer, T. Pollock, C. Marcus, and C. Palmstrøm, “Limits to mobility in InAs quantum wells with nearly lattice-matched barriers,” *Phys. Rev. B*, vol. 94, p. 245306, 2016. (Cited on page 53.)
- [106] T. F. Kuech, ed., *Handbook of Crystal Growth*. Elsevier Science Publishers B.V. (North-Holland), 2015. (Cited on page 54.)
- [107] L. Casparis, M. R. Connolly, M. Kjaergaard, N. J. Pearson, A. Kringhøj, T. W. Larsen, F. Kuemmeth, T. Wang, C. Thomas, S. Gronin, G. C. Gardner, M. J. Manfra, C. M. Marcus, and K. D. Petersson, “Superconducting gatemon qubit based on a proximitized two-dimensional electron gas,” *Nat. Nanotechnol.*, vol. 13, p. 915, 2018. (Cited on pages 54 and 66.)
- [108] A. C. C. Drachmann, H. J. Suominen, M. Kjaergaard, B. Shojaei, C. J. Palmstrøm, C. M. Marcus, and F. Nichele, “Proximity Effect Transfer from NbTi into a Semiconductor Heterostructure via Epitaxial Aluminum,” *Nano Lett.*, vol. 17, p. 1200, 2017. (Cited on pages 55, 56, 66, and 132.)
- [109] H. J. Suominen, M. Kjaergaard, A. R. Hamilton, J. Shabani, C. J. Palmstrøm, C. M. Marcus, and F. Nichele, “Zero-Energy Modes from Coalescing Andreev States in a Two-Dimensional Semiconductor-Superconductor Hybrid Platform,” *Phys. Rev. Lett.*, vol. 119, p. 176805, 2017. (Cited on pages 58 and 66.)

-
- [110] M. Kjaergaard, *Proximity Induced Superconducting Properties in One and Two Dimensional Semiconductors*. Ph.d thesis, University of Copenhagen, 2015. (Cited on page 61.)
- [111] C. G. L. Bøttcher, F. Nichele, M. Kjaergaard, H. J. Suominen, J. Shabani, C. J. Palmstrøm, and C. M. Marcus, “Superconducting, insulating and anomalous metallic regimes in a gated two-dimensional semiconductor–superconductor array,” *Nat. Phys.*, vol. 14, p. 1138, 2018. (Cited on pages 66 and 115.)
- [112] J. S. Lee, B. Shojaei, M. Pendharkar, A. P. McFadden, Y. Kim, H. J. Suominen, M. Kjaergaard, F. Nichele, H. Zhang, C. M. Marcus, and C. J. Palmstrøm, “Transport Studies of Epi-Al/InAs Two-Dimensional Electron Gas Systems for Required Building-Blocks in Topological Superconductor Networks,” *Nano Lett.*, vol. 19, p. 3083, 2019. (Cited on page 66.)
- [113] W. Mayer, J. Yuan, K. S. Wickramasinghe, T. Nguyen, M. C. Dartailh, and J. Shabani, “Superconducting proximity effect in epitaxial Al-InAs heterostructures,” *Appl. Phys. Lett.*, vol. 114, p. 103104, 2019. (Cited on pages 66 and 107.)
- [114] F. Nichele, E. Portolés, A. Fornieri, A. M. Whiticar, A. C. C. Drachmann, S. Gronin, T. Wang, G. C. Gardner, C. Thomas, A. T. Hatke, M. J. Manfra, and C. M. Marcus, “Relating Andreev Bound States and Supercurrents in Hybrid Josephson Junctions,” *Phys. Rev. Lett.*, vol. 124, p. 226801, 2020. (Cited on page 66.)
- [115] C. Baumgartner, L. Fuchs, L. Frész, S. Reinhardt, S. Gronin, G. C. Gardner, M. J. Manfra, N. Paradiso, and C. Strunk, “Josephson inductance as a probe for highly ballistic semiconductor–superconductor weak links,” 2020, arXiv: 2007.08371. (Cited on page 66.)
- [116] G. E. J. Poinern, N. Ali, and D. Fawcett, “Progress in nano-engineered anodic aluminum oxide membrane development,” *Materials (Basel)*, vol. 4, p. 487, 2010. (Cited on page 67.)

- [117] J. W. Diggle, T. C. Downie, and C. W. Goulding, "Anodic oxide films on aluminum," *Chem. Rev.*, vol. 69, p. 365, 1969. (Cited on pages 67 and 100.)
- [118] M. Weides, R. C. Bialczak, M. Lenander, E. Lucero, M. Mariantoni, M. Neeley, A. D. O'Connell, D. Sank, H. Wang, J. Wenner, T. Yamamoto, Y. Yin, A. N. Cleland, and J. Martinis, "Phase qubits fabricated with trilayer junctions," *Supercond. Sci. Technol.*, vol. 24, p. 055005, 2011. (Cited on page 67.)
- [119] V. F. Henley, *Anodic oxidation of aluminum and its alloys*. Pergamon Press, 1982. (Cited on pages 67 and 142.)
- [120] Y. Nakamura, D. L. Klein, and J. S. Tsai, "Al/Al₂O₃/Al single electron transistors operable up to 30 K utilizing anodization controlled miniaturization enhancement," *Appl. Phys. Lett.*, vol. 68, p. 275, 1996. (Cited on page 67.)
- [121] A. C. C. Drachmann, R. E. Diaz, C. Thomas, H. J. Suominen, A. M. Whiticar, A. Fornieri, S. Gronin, T. Wang, G. C. Gardner, A. R. Hamilton, F. Nichele, M. J. Manfra, and C. M. Marcus, "Anodic Oxidation of Epitaxial Superconductor-Semiconductor Hybrids," arXiv: 2009.08190. (Cited on pages 75, 76, 79, 85, and 99.)
- [122] Y. T. Fan, M. C. Lo, C. C. Wu, P. Y. Chen, J. S. Wu, C. T. Liang, and S. D. Lin, "Atomic-scale epitaxial aluminum film on GaAs substrate," *AIP Adv.*, vol. 7, p. 075213, 2017. (Cited on page 75.)
- [123] T. Iwata, T. Matsumoto, S. Terakawa, and H. Kobayashi, "Fabrication of Al₂O₃/Al structure by nitric acid oxidation at room temperature," *Cent. Eur. J. Phys.*, vol. 8, p. 1015, 2010. (Cited on pages 78 and 134.)
- [124] D. Qian, B. Xu, M. Chi, and Y. S. Meng, "Uncovering the roles of oxygen vacancies in cation migration in lithium excess layered oxides," *Phys. Chem. Chem. Phys.*, vol. 16, p. 14665, 2014. (Cited on page 78.)

-
- [125] P. Wissmann and H.-U. Finzel, *Electrical Resistivity of thin Metal Films*. Springer, 2007. (Cited on page 81.)
- [126] O. Dimitrova and M. V. Feigel'man, "Theory of a two-dimensional superconductor with broken inversion symmetry," *Phys. Rev. B*, vol. 76, p. 014522, 2007. (Cited on page 81.)
- [127] T. Chui, P. Lindenfeld, W. L. McLean, and K. Mui, "Coupling and isolation: Critical field and transition temperature of superconducting granular aluminum," *Phys. Rev. B*, vol. 24, p. 6728, 1981. (Cited on page 82.)
- [128] A. D. C. Grassie, D. B. Green, and A. Benyon, "Disordered aluminium films," *Physica*, vol. 55, p. 243, 1971. (Cited on page 82.)
- [129] B. Shinozaki, T. Kawaguti, and Y. Fujimori, "Upward Curvature of the Temperature Dependence of Upper Critical Magnetic Field Perpendicular to Superconducting Aluminum Films," *J. Phys. Soc. Japan*, vol. 52, p. 2297, 1983. (Cited on page 82.)
- [130] N. Maleeva, L. Grünhaupt, T. Klein, F. Levy-Bertrand, O. Dupre, M. Calvo, F. Valenti, P. Winkel, F. Friedrich, W. Wernsdorfer, A. V. Ustinov, H. Rotzinger, A. Monfardini, M. V. Fistul, and I. M. Pop, "Circuit quantum electrodynamics of granular aluminum resonators," *Nat. Commun.*, vol. 9, p. 3889, 2018. (Cited on page 83.)
- [131] I. Glozman, C. E. Johnson, and H. W. Jiang, "Fate of the delocalized states in a vanishing magnetic field," *Phys. Rev. Lett.*, vol. 74, p. 594, 1995. (Cited on page 96.)
- [132] M. Kayyalha, D. Xiao, R. Zhang, J. Shin, J. Jiang, F. Wang, Y. F. Zhao, R. Xiao, L. Zhang, K. M. Fijalkowski, P. Mandal, M. Winnerlein, C. Gould, Q. Li, L. W. Molenkamp, M. H. Chan, N. Samarth, and C. Z. Chang, "Absence of evidence for chiral Majorana modes in quantum anomalous Hall-superconductor devices," *Science*, vol. 367, p. 64, 2020. (Cited on page 97.)

- [133] E. N. Jin, A. Kakekhani, S. Ismail-Beigi, C. H. Ahn, and F. J. Walker, "Two-dimensional electron gas oxide remote doping of Si(001)," *Phys. Rev. Mater.*, vol. 2, p. 115001, 2018. (Cited on page 114.)
- [134] C. W. Liu, C. Chuang, Y. Yang, R. E. Elmquist, Y. J. Ho, H. Y. Lee, and C. T. Liang, "Temperature dependence of electron density and electron-electron interactions in monolayer epitaxial graphene grown on SiC," *2D Mater.*, vol. 4, no. 2, 2017. (Cited on page 114.)
- [135] A. F. Hebard and M. A. Paalanen, "Magnetic-field-tuned superconductor-insulator transition in two-dimensional films," *Phys. Rev. Lett.*, vol. 65, p. 927, 1990. (Cited on page 115.)
- [136] N. Mason and A. Kapitulnik, "Dissipation effects on the superconductor-insulator transition in 2D superconductors," *Phys. Rev. Lett.*, vol. 82, p. 5341, 1999. (Cited on page 115.)
- [137] Z. Han, A. Allain, H. Arjmandi-Tash, K. Tikhonov, M. Feigel'Man, B. Sacépé, and V. Bouchiat, "Collapse of superconductivity in a hybrid tin-graphene Josephson junction array," *Nat. Phys.*, vol. 10, p. 380, 2014. (Cited on page 115.)
- [138] Z. Tan, C. Tan, L. Ma, G. T. Liu, L. Lu, and C. L. Yang, "Shubnikov-de Haas oscillations of a single layer graphene under dc current bias," *Phys. Rev. B - Condens. Matter Mater. Phys.*, vol. 84, p. 115429, 2011. (Cited on page 121.)
- [139] A. Boisen, K. Birkelund, O. Hansen, and F. Grey, "Fabrication of submicron suspended structures by laser and atomic force microscopy lithography on aluminum combined with reactive ion etching," *J. Vac. Sci. Technol. B Microelectron. Nanom. Struct.*, vol. 16, p. 2977, 1998. (Cited on page 132.)
- [140] Z. J. Davis, G. Abadal, O. Hansen, X. Borisé, N. Barniol, F. Pérez-Murano, and A. Boisen, "AFM lithography of aluminum for fabrication of nanomechanical systems," *Ultramicroscopy*, vol. 97, p. 467, 2003. (Cited on page 132.)

-
- [141] F. H. Hedlund, M. F. Nielsen, S. H. Mikkelsen, and E. K. Kragh, "Violent explosion after inadvertent mixing of nitric acid and isopropanol - Review 15 years later finds basic accident data corrupted, no evidence of broad learning," *Saf. Sci.*, vol. 70, p. 255, 2014. (Cited on page 134.)